Computer Simulations of Laser Ablation from Simple Metals to Complex Metallic Alloys

Computersimulationen der Laserablation von einfachen Metallen hin zu Komplexen Metallischen Phasen

Von der Fakultät für Mathematik und Physik der Universität Stuttgart zur Erlangung der Würde eines Doktors der Naturwissenschaften (Dr. rer. nat.) genehmigte Abhandlung

Vorgelegt von

Steffen Sonntag

aus Öhringen

Hauptberichter:	Prof. Dr. H.-R. Trebin
Mitberichter:	Prof. Dr. C. Holm
Tag der mündlichen Prüfung:	21. Februar 2011

Institut für Theoretische und Angewandte Physik
der Universität Stuttgart

2010

Theresia und Josef

Contents

List of Symbols

$\langle\omega^2\rangle$	Averaged squared phonon frequency, page 44
α	Inverse absorption length, page 55
γ	Electron constant of specific heat, page 41
κ	Electron–phonon coupling constant, page 41
$\lambda(T)$	Electron–phonon enhancement parameter, page 44
$\mathcal{D}(E)$	Density of states, page 37
$\mathcal{T}_{\boldsymbol{R}_i}$	Translation opererator, page 28
τ_{ee}	Electron–electron scattering time, page 40
τ_{el}	Electron–lattice relaxtion time, page 41
C_{el}	Specific heat of the electrons, page 38
C_{l}	Specific heat of the lattice, page 43
d_{abl}	Ablation depth, page 77
d_{melt}	Melting depth, page 95
F_{th}	Ablation threshold, page 77
F_{melt}	Melting threshold, page 96
K_{el}	Thermal conductivity of the electrons, page 38
K_{l}	Thermal conductivity of the lattice, page 43
$S(\boldsymbol{x}, t)$	Laser power density, page 43
v_{s}	Speed of sound, page 79

$Y(N)^{-\delta}$	Yield distribution function, page 86
`IMD`	ITAP Molecular Dynamics, page 51
CMA	Complex Metallic Alloy, page 34
EAM	Embedded atom method, page 53
FD	Finete differences, page 58
MD	Molecular dynamics, page 50
QC	Quasicrystal, page 35
TTM	Two–Temperature model, page 43

List of Figures

List of Tables

Abstract

In this work, a method for computer simulations of laser ablation in metals is presented. The ambitious task to model the physical processes, that occur on different time and length scales, is overcome to some extent by the combination of two techniques: Molecular dynamics and finite differences. The former is needed to achieve atomistic resolution of the processes involved. Material failure like melting, vaporization or spallation occur on the atomic scale. Light absorption and electronic heat conduction, which plays the major role in metals, is described by a generalized heat conduction equation solved by the finite differences method. From the so–called Two–Temperature Model temperature, density and pressure evolution – both in time and space – can be derived. With this, various studies on laser heated metals were done. For reasons discussed in more detail later, aluminum was chosen as a model system for most simulations on isotropic materials. As a more complex structure, the metallic alloy $Al_{13}Co_4$ was used because of its special material properties. As an approximant to the decagonal phase of Al–Ni–Co, the alloy shows an anisotropy in its transport properties, e.g. an anisotropic heat conduction.

It will be shown, that the model is able to describe the physics in laser heated solids on time scales from 100 fs up to the ns–scale properly. Great insight was gained about the processes occuring during and shortly after the laser pulse. Many of the quantities interesting for experimentalists can be predicted by the theory. From the simulations relevant parameters like the electron–cooling time or the important ablation threshold were calculated. All values match their experimental counterpart very well.

Computersimulation der Laserablation von einfachen Metallen hin zu Komplexen Metallischen Phasen

Zusammenfassung in deutscher Sprache

Die vorliegende Arbeit beschäftigt sich mit der Laserablation in Metallen. Ziel ist es, mit Hilfe von numerischen Simulationen das Verhalten von Metallen nach der Bestrahlung mit intensiven Laserpulsen vorherzusagen. Die Arbeit ist inhaltlich in zwei Teile gegliedert. In der ersten Hälfte werden theoretische Grundlagen, eine qualitative Beschreibung der Ablation und die Implementierung des Modells gegeben. Im zweiten Teil folgen Ergebnisse sowie, falls vorhanden, Vergleiche mit Experimenten. Die Arbeit schließt mit einer Zusammenfassung und einem Ausblick.

Einleitung

Mit dem Aufkommen von ultrakurzen Piko– und vor allem Femtosekunden–Laserpulsen hat sich eine Vielzahl neuer Bearbeitungsmöglichkeiten von Materialien eröffnet. Für die Anwendung ergeben sich industrielle Verfahren wie Bohren, Erodieren, Schweißen, Strukturieren oder Markieren. Darüber hinaus ist die Laserablation ein wichtiger Bestandteil der modernen Chirurgie geworden. Gerade für Anwendungen im Mikrostrukturbereich liegt der Vorteil der Femtosekundenpulse in schärferen Lochgeometrien sowie einer, durch die kürzere Wärmeleitung bedingten, kleineren, wärmeaffektierten Zone. Das Material wird außerhalb des bearbeiteten Bereichs erheblich geschont.

Verschiedene experimentelle sowie theoretische Studien beschäftigen sich mit den Vorgängen, die während der Ablation passieren. Je nach Schwerpunkt geht es dabei um das Materialinnere, um Oberflächeneffekte oder Vorgänge in der entstehenden Gas– und Plasmawolke. Aufgrund der komplexen Natur der auf unterschiedlichen Zeit– und Längenskalen vorkommenden Prozesse ist es eine anspruchsvolle Aufgabe, theoretische sowie numerische Modelle zu finden. Die auftretenden Prozesse umfassen dabei mehr als vier Größenordnungen in ihrem zeitlichen Ablauf. Während der Laserpuls im Bereich von Femtosekunden liegt, dauert es Nanosekunden für den Austrieb von Schmelze oder das Abkühlen der Probe. Typische Elektron–Gitter Relaxationszeiten liegen mit Pikosekunden dazwischen. Es scheint unmöglich, innerhalb eines Modells alle Mechanismen zu beschreiben. Erschwerend kommt hinzu, dass es sich bei den vorkommenden Mechanismen je nach Material (etwa bei der Wechselwirkung mit Licht) um unterschiedliche Vorgänge handelt.

Werden Laserpulse bedeutend kürzer als die Elektron–Gitter Relaxationszeit, befinden sich Elektronen und Gitter in einem Metall nicht mehr im thermischen Gleichgewicht. Die beiden Systeme müssen getrennt behandelt werden. Einer der ersten theoretischen Ansätze, der dies berücksichtigte war das von Anisimov 1974 vorgestellte Zwei–Temperatur–Modell (TTM, vom Englischen *Two–Temperature Model*). Es beschreibt die zeitliche Entwicklung der Elektronen- und Gittertemperatur durch zwei gekoppelte partielle Differenzialgleichungen. Das Zwei–Temperatur–Modell hat sich über die Jahre als vielversprechender Ausgangspunkt für viele Untersuchungen und Theorien etabliert. Neben numerischen Rechnungen gibt es relativistische Korrekturen um die instantane Wärmeausbreitung, wie sie durch das Fourier Gesetz gegeben ist, zu verhindern. Es gibt Erweiterungen der verwendeten Konstanten, wie der thermischen Leitfähigkeit oder der Elektron–Phonon Wechselwirkung auf einen weiten Temperaturbereich. Das Zwei–Temperatur–Modell wurde an Molekulardynamik Simulationen oder an hydrodynamische Gleichungen gekoppelt. Bei Ultrakurzzeitphänomenen diente es als Ausgangspunkt für Elektronendynamik außerhalb des thermischen Gleichgewichts. Änderungen zur Fermi–Dirac Statistik wurden untersucht.

Um die verschiedenen Längenskalen zu überwinden, nutzt man Multi–Skalen–Simulationen. Eine laterale Erweiterung wurde durch die Kopplung von Molekulardynamik an Finite–Elemente erreicht. In Einfallsrichtung des Lasers sorgen Monte–Carlo–Methoden für die Berechnungen der Gaswolke

bis zu mehreren Mikrometern Ausdehnung.

Für Anwendungen wie der gepulsten Laserdeposition von Materie (PLD vom Englischen *pulsed laser deposition*) ist es von größter Wichtigkeit, die Zusammensetzung der Gaswolke zu kontrollieren. Zusammensetzung sowie Entstehung finden ebenfalls auf verschiedenen Zeit– und Größenskalen statt. Weiter gibt es Simulationen der Kraterbildung sowie zur Analyse des abgetragenen Materials. Cluster–, Winkel–, Ladungs– oder Geschwindigkeitsverteilung sind dabei von besonderem Interesse.

Viele der bereits durchgeführten theoretischen Überlegungen wurden an Modellsystemen wie Lennard–Jones Kristallen gemacht. Teilchenzahlen waren dabei nicht selten vergleichsweise gering. Andere Rechnungen waren auf weniger als drei Raumdimensionen oder organische Materialien beschränkt. Wo eine Vergleichsmöglichkeit zu anderen Arbeiten bezüglich der Systemgröße und der verwendeten Potenziale besteht, wurde auf eine Wärmeleitung über das Zwei–Temperatur–Modell verzichtet.

Es ist das Bestreben dieser Arbeit, Methoden vorzustellen, mit denen vollständige Studien der Laserablation in Metallen durchgeführt werden können. Zusätzlich werden notwendige Simulations– und Analysewerkzeuge vorgestellt, damit man anschließend die Ergebnisse qualitativ und quantitativ mit Experimenten vergleichen kann.

Theoretischer Hintergrund

Der Ablationsprozess kann materialunabhängig in vier Schritten zusammengefasst werden. Diese sind:

1. Absorption von Laserstrahlung durch das Medium.
2. Umwandlung von eingestrahlter Energie in thermische Schwingungen.
3. Emission von Partikeln an der Oberfläche.
4. Unter gewissen Umständen die Bildung einer Plasmawolke.

Je nach Material handelt es sich dabei um unterschiedliche Prozesse. In Metallen erfolgt die Absorption durch die freien bzw. schwach gebundenen Elektronen. Nach einer Thermalisierung findet ein Energieübertrag durch Stöße an das Atomgitter statt. Durch Stöße der Elektronen untereinander wird die Wärme zusätzlich diffusiv unter die Oberfläche transportiert.

Übersteigt die eingekoppelte Energie einen kritischen Wert, die *Ablations–* oder *Abtragsschwelle*, findet ein Abtrag von Teilchen statt.

Gitterschwingungen sowie Phasenumwandlungen von fest nach flüssig oder von flüssig nach gasförmig können bereits durch Molekulardynamikrechnungen beschrieben werden. Molekulardynamik (MD) bezeichnet Computersimulationen, bei denen Wechselwirkungen zwischen Atomen oder Molekülen berechnet und daraus Teilchentrajektorien bestimmt werden. Es wird die NEWTONsche Bewegungsgleichung für ein Vielteilchensystem numerisch integriert. Im Gegensatz zu *ab initio* Methoden, die auf quantenmechanischen Rechnungen basieren, verwendet die Molekulardynamik Kraftfelder oder semiempirische Methoden, um Simulationen mit großen Teilchenzahlen zu erreichen. Diese werden an theoretische Rechnungen sowie an experimentelle Daten, etwa die Schmelztemperatur oder die Gitterkonstante, angepasst. Das makroskopische Verhalten des Stoffes wird dadurch bestmöglich wiedergegeben. Im Vergleich zu ab initio Rechnungen (bis max. 1000 Atome) sind Teilchenzahlen im dreistelligen Millionenbereich möglich.

Die Temperatur eines Körpers lässt sich in MD Simulationen durch den Mittelwert der kinetischen Energie der Atome definieren. Größere Energien entsprechen dabei höheren Temperaturen. Durch die Änderung der Geschwindigkeitsverteilung nahe der Oberfläche kann eine Umwandlung von Laserleistung in thermische Schwingungen modelliert werden. Je nach Größe der Materialparameter kommt es im Vergleich mit dem Experiment jedoch zu Abweichungen. Die fehlende Wärmeleitung der Elektronen, die in Metallen den überwiegenden Teil ausmacht, sorgt für eine unphysikalische Lokalisierung der eingebrachten Energie, ein Problem, das bereits bei den ersten Simulationen der Laserablation in den 1990er Jahren bekannt war.

Eine wesentlich realistischere Wärmeausbreitung kann durch ein 1974 vorgestelltes Modell für laserbestrahlte Metalloberflächen erreicht werden. Das Zwei–Temperatur–Modell beschreibt die Lösung einer verallgemeinerten Wärmeleitungsgleichung für Elektronen– und Gittertemperatur durch inhomogene partielle Differenzialgleichungen. Von diesen Gleichungen wird für die Modellierung der Ablation nur der elektronische Teil verwendet. Die Gitterdynamik wird durch die Molekulardynamik übernommen und entsprechend an das Kontinuumsmodell gekoppelt. Der Austausch von Energie wird über eine Elektron–Phonon–Kopplung ermöglicht. Es entsteht eine Hybridsimulation, die Vorteile beider Methoden kombiniert. Dadurch ist es

gelungen, die Laserleistung physikalisch sinnvoll in das System zu bringen: Energie wird vom elektronischen System absorbiert und diffusiv unter die Oberfläche geleitet. Gleichzeitig wechselwirkt es mit den Atomrümpfen, die sich in Folge dessen aufheizen. Es ist somit möglich, die Prozesse bei der Laserablation in atomarer Auflösung zu erfassen.

Ergebnisse

Für die Studien an Metallen wurde reines Aluminium als Material ausgewählt, nicht zuletzt, weil für dieses Metall bereits geeignete EAM–Potenziale in der Literatur existieren. Weiter gibt es bei Aluminium im festen Zustand keine temperatur– oder druckabhängigen Phasenumwandlungen, wie es andere Metalle zeigen, die zusätzliche Modellierung erfordern würden. Da bei der Ablation alle Aggregatzustände vorkommen können, ist es sinnvoll, im Vorfeld das Phasendiagramm des Potenzials zu ermitteln. Dazu wurden verschiedene Schmelz– sowie Verdampfungssimulationen durchgeführt. Es konnte gezeigt werden, dass sich alle drei Phasen mehr als zufriedenstellend reproduzieren lassen.

Für den Fall einfachen Aufheizens wurde eine räumlich konstante Laserintensität verwendet. Im Experiment entspricht dies der Zone im Zentrum eines gaußförmigen Laserstrahls. Durch Simulationsreihen, bei denen die Laserleistung sukzessiv erhöht wurde, konnte das Schmelz– und Abtragungsverhalten bestimmt werden. Für das Modell mit elektronischer Wärmeleitung ergibt sich dabei ein Wert für die Ablationsschwelle von $F_{\mathrm{th}} = (858 \pm 170)\ \mathrm{J/m^2}$. Für die bestimmte thermische Eindringtiefe α^{-1} ergab die Simulation (27 ± 6) nm. Die experimentellen Werte liegen je nach Messung zwischen 580 und 1200 $\mathrm{J/m^2}$ für die Abtragsschwelle und bei 39 nm für die Eindringtiefe. Die aus der Simulation vorhergesagten Werte stimmen demnach sehr gut mit den Experimenten überein.

Als weitere Ablationssimulation wurde eine inhomogene Leistungsdichte, wie sie für TEM_{00}–Moden vorliegt, durchgeführt. Aufgrund der begrenzten Systemgröße von 60 Millionen Atome musste von einer Wärmeleitung der Elektronen abgesehen werden. Wegen der großen Temperaturgradienten, die an der Oberfläche entstehen, würde sich die Temperatur zu schnell verteilen, sodass erneut ein homogenes Profil vorliegen würde. Die Simulationen wurden deshalb mit dem einfacheren Modell, das lediglich die Geschwindigkeiten der Atome verändert, durchgeführt. Als Ablationsschwel-

le ergibt sich hier ein Wert von (1137 ± 166) J/m^2, was noch immer im Toleranzbereich der Experimente liegt. Anders ist es bei der thermischen Eindringtiefe. Der gefundene Werte $\alpha^{-1} = (8.6 \pm 1.7)$ nm liegt erheblich unterhalb der experimentellen Vorgaben. Dieser Wert entspricht im Fall fehlender Wärmeleitung in etwa der optischen Eindringtiefe $l_\alpha = 8$ nm.

Im Vergleich zum komplexeren Zwei–Temperatur–Modell entsteht über der Probe wegen der inhomogenen Anregung eine Gasphase, die weiter analysiert werden kann. Für die sich mit ca. 6 km/s ausbreitenden Gaswolke (experimentelle Werte schwanken zwischen 3 und 30 km/s) können Statistiken über Größen–, Winkel– und Geschwindigkeitsverteilung aufgestellt werden. Es zeigt sich, dass die Größenverteilung der entstehenden Cluster einem Potenzgesetz folgt. Der gefundene Exponent liegt mit $\delta = 5.1$ nahe an den experimentellen Werten (zwischen 7.7 und 9.3). Die experimentellen Daten sind aus Ionenbeschuss von Metalloberflächen gewonnen, sodass es sich für das Potenzgesetz um ein universales Verhalten zu handeln scheint. Auch wenn die kleinsten erreichbaren Strahldurchmesser mit $0.5 - 1$ μm eine Größenordnung über der Simulation liegen, sind die gefundenen Ergebnisse gut vergleichbar.

Da das Institut für Theoretische und Angewandte Physik als Hintergrund die Physik komplexer metallischer Legierung hat, bot es sich an, ebenfalls deren Ablationsverhalten zu studieren. Als Einstiegssystem diente ein Approximant für die dekagonale Phase von Al–Ni–Co, $Al_{13}Co_4$. Strukturell vereint diese Legierung Eigenschaften periodischer und quasiperiodischer Festkörper: Sie besteht aus quasiperiodischen Ebenen, die periodisch geschichtet sind. Die Wärmeleitfähigkeit erhält somit eine Richtungsabhängigkeit.

Wie erwartet gibt es wegen der anisotropen Wärmeleitung unterschiedliche Schmelztiefen – wenn auch nicht sehr ausgeprägt (< 5 nm). Eine erste Erklärung für diese schwache Richtungsabhängigkeit gibt die relativ hohe Elektron–Phonon–Kopplung in Aluminium–Cobalt. Diese sorgt für eine sehr kurze Elektron–Gitter Relaxationszeit, wodurch die diffusive Wärmeleitung der Elektronen verkürzt wird.

Zusammenfassung

In der vorliegenden Arbeit wird ein Modell vorgestellt, mit dessen Hilfe die Laserablation in Metallen quantitativ und qualitativ beschrieben wer-

den kann. Im verwendeten Zwei–Temperatur–Modell wird die vom Laser an das Material abgegebene Leistung von den freien Elektronen absorbiert und anschließend diffusiv unter die Oberfläche transportiert. Gleichzeitig findet ein Energieaustausch mit dem Atomgitter statt. Alle vorhergesagten Parameter, wie beispielsweise die Elektron–Gitter Relaxationszeit oder die Ablationsschwelle, liegen innerhalb der experimentell bestimmten Werte oder sind vergleichbar. Eine tabellarische Zusammenfassung aller Parameter sowie deren experimenteller Gegenstücke findet sich auf Seite 102.

Zusammenfassend konnte gezeigt werden, dass mit Hilfe von atomistischen Computersimulationen vielversprechende Aus– und Vorhersagen über das Verhalten von laserbestrahlten Metallen getroffen werden können.

Chapter 1

Introduction

Over the years material processing with intensive laser radiation has found numerous applications such as micro–machining [110, 94], nano–technology, e.g. the creation of nano diamond clusters [4] and carbon nanotubes [105] or thin–film deposition [27]. Aside from industrial applications, laser ablation is used in the medical world for the removal of biological tissue [134]. It seems that for each process and material a best suitable laser source can be found. While there are applications for nanosecond (ns) pulses [14], various studies show the advantages of femtosecond (fs) pulses over the ns–regime for microstructuring. Most important are the sharper hole geometries [26] and the smaller damage due to the limited heat transfer perpendicular to the incoming laser pulse, resulting in a reduced thermally effected area around the laser spot [127].

Different studies, experimental and also theoretical ones, deal with the processes occurring in the bulk material or the surface during or after the laser pulse. Due to the complex character of the processes involved at different time and length scales, theoretical and computational investigations are a challenging task. It seems impossible to describe all processes that occur within a single model. In addition, the mechanisms, e.g. for photon absorption, are different for different classes of materials [23].

An important quantity one has to look at is the electron–lattice relaxation time. When pulses became shorter than this time, the electrons and the lattice are out of thermal equilibrium and have to be described separately. One of the first theoretical models for laser heated solids was given 1974 by Anisimov [7]. Over the years his introduced Two–Temperature Model (TTM) has become the starting point for many investigations. It is also the basis of the simulations presented in this work. The TTM describes the lattice and the electron temperature evolution via two coupled inhomogeneous partial differential equations. Besides numerical solutions of the basic equations, various extensions exist. There are suggestions for rela-

tivistic corrections, like the one given by Hüttner [58] or a generalization of the used parameters, e.g. the heat conductivity or the electron–phonon coupling constant to higher temperatures [28]. The TTM was coupled to molecular dynamics [114, 61] or to hydrodynamic calculations [29]. It was also used to describe ultrashort phenomena in non–equilibrium electron dynamics as done by Rethfeld [108]. Multi–scale models exist, where additionally to the TTM finite element methods were used to achieve lateral dimensions up to 600 nm [60]. On top, Monte Carlo simulations were done to describe the evolving gas plume and to increase the size of the simulations to the μm–scale [142].

For applications like pulsed laser deposition (PLD) or matrix–assisted laser deposition/ionization (MALDI) of biomolecules [55], the ability to predict and control the cluster composition of the plume is critical. Experimental studies for cluster formation exist over different time regimes from many picoseconds down to less than 100 fs [22, 81, 74]. Also numerical investigations of plume evolution were carried out by different methods, such as molecular dynamics [1] or Monte Carlo simulations [46], and were compared to experiments. There are simulations for crater formation or the composition of the ablated material, i.e. cluster size, velocity and angular distributions [10, 143].

However, many of the the existing simulations were either done on model systems with Lennard–Jones potentials or have comparatively small sample sizes [126, 1]. Others were restricted to less than three dimensions or non–metallic systems [16, 141]. Where comparable conditions (regarding sample size or used potentials) exist, a different approach for the heat conduction was used instead of the TTM [6, 138]. It is the goal of this work to present a method, containing simulation and analysis tools, for a comprehensive study on heated metals by ultrashort laser pulses. A complete study on aluminum will be shown and all relevant parameters will be extracted from the simulation and compared to experiments.

The thesis is organized as follows. In the first part an introduction to the theoretical background is given. The ablation process is described qualitatively and a model for ultra–short laser pulses in metals is presented. Then, the implementation scheme of the basic equations is proposed. In the last part, results from the simulations of various scenarios are discussed. Among them are simulations of homogenous laser fluences in aluminum, melting and ablation experiments and studies of the evolving gas plume. A short look is taken on a system with anisotropic material properties:

$Al_{13}Co_4$. The thesis is summarized in the last chapter.

Parts of this work have already been published. A *List of Publications* is given on page 125.

Chapter 2

Theoretical Background

In the following chapter basic theories from solid state physics are presented. This includes an introduction to crystal lattices, solid state HAMILTONians, heat conduction in metals, quasicrystals and complex metallic alloys. A key understanding of the processes involved in laser ablation is necessary to invent a practical — but not too complex — model of the ablation mechanisms. After a qualitative discussion of the ablation process, the well established Two–Temperature Model (TTM) is presented. The TTM describes the temperature evolution in laser heated solids with two coupled partial differential equations. In the last part an improvement of this model is proposed. The extended Two-Temperature Model (eTTM) can be used within ultra–short phenomena, when the finite propagation of heat plays a role.

2.1 Metal Physics

Classically there are three states of matter: The solid, the liquid and the gaseous phase. The gas phase can be characterized such, that all particles capture the whole available volume. In contrast are the solids, with a fixed volume and a fixed shape. Liquids are in between, the volume is fixed, but the shape is enforced by a surrounding container. Solids can be classified in amorphous ones like glasses or ceramics in whose only a short range order exist, and crystalline ones like metals. Additionally to this short range order, the crystalline phases possess a long range order, accomplished by the repetition of an identical unit cell in all space directions. Given the fact that most simulations in this work were done on perfect metals, like aluminum or copper, the focus will be on the description of perfect crystal structures.

Crystal Lattices

One may argue that perfect structures and also infinite crystals cannot be found in nature. But for real crystals, having atom numbers in the order of 10^{23}, this approximation of an infinite solid is sufficient. Though the restriction to perfect periodic structures lacks the regard of effects like impurities or disorder. Impurities can be considered as a perturbation of an ordered system, while disorder is needed to study other phenomena like glassy behavior. Nevertheless, these effects are neglected, as they play a minor role in the physics of laser ablation.

For a perfect crystal, a BRAVAIS lattice has to be defined. This lattice specifies the underlying structures, to which the basis is affixed. A basis can be a single atom, atomic–groups, ions or molecules. A d–dimensional BRAVAIS lattice consists of all vectors

$$\boldsymbol{R}_i = \sum_{j=1}^{d} n_{i_j} \boldsymbol{a}_j \tag{2.1}$$

with integer-numbers n_{i_j}. The $\boldsymbol{a}_i$ with $i = 1, \ldots, d$ are the basis vectors of the lattice. The simplest lattice is the *primitive lattice*, where the same atom is put on each lattice point $\boldsymbol{R}_i$ of the BRAVAIS lattice. The primitive lattice is invariant under translation by any vector $\boldsymbol{R}_i$, because it results in the same infinite lattice. The translation $\mathcal{T}_{\boldsymbol{R}_i}$ is defined through an operator, which acts on an arbitrary function $f(\boldsymbol{r})$, e.g. the density or the electronic wave function, by replacing $\boldsymbol{r} \to \boldsymbol{r} + \boldsymbol{R}_i$:

$$\mathcal{T}_{\boldsymbol{R}_i} \quad : \quad f(\boldsymbol{r}) \to f(\boldsymbol{r} + \boldsymbol{R}_i). \tag{2.2}$$

For most problems such a simple crystal lattice is not sufficient. For the description of complex crystal structures, a lattice with basis has to be introduced. The j different nuclei are grouped around the basis vectors $\boldsymbol{r}_j$ relative to the BRAVAIS lattice points, i.e. at $\boldsymbol{R}_i + \boldsymbol{r}_j$. To fill the whole space without a gap or overlap, the concept of an *elementary cell* is used. This unit cell does not have to share the symmetry of the lattice.

There are several ways to construct an elementary cell. One choice is the parallelepiped spanned by the basis vectors of the BRAVAIS lattice, see Fig. 2.1(a). Another example for a primitive cell is the the WIGNER–SEITZ cell of a lattice. It is defined as the set of points in space, that are closer to the given lattice point than to any other lattice point. Geometrically,

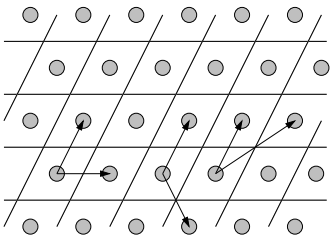

(a) One possible elementary cell as well as different basis vectors.

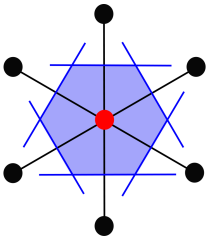

(b) The Wigner–Seitz cell of a two–dimensional lattice with sixfold symmetry.

Figure 2.1: Examples of different elementary cells for the primitive lattice and the construction of the Wigner–Seitz cell.

the cell is constructed by drawing the perpendicular bisector planes of the translation vectors from one lattice point to its nearest neighbors (see Fig. 2.1(b)). This volume shares the symmetry of the underlying lattice. While in direct space this concept is not of highest interest, it is extremely important in reciprocal space. There, the cell is called the first Brillouin zone and contains all information about a material whether it will be a conductor, semiconductor or an insulator.

The Reciprocal Space

For the sake of simplicity, all formulas will be limited to three dimensions from now on. The volume of the elementary cell, spanned by its basis vectors, is

$$\Omega = \boldsymbol{a}_1 \cdot (\boldsymbol{a}_2 \times \boldsymbol{a}_3). \tag{2.3}$$

The following three vectors are now defined as the basis vectors of the reciprocal lattice:

$$\left.\begin{aligned} \boldsymbol{b}_1 &= (2\pi/\Omega)\boldsymbol{a}_2 \times \boldsymbol{a}_3 \\ \boldsymbol{b}_2 &= (2\pi/\Omega)\boldsymbol{a}_3 \times \boldsymbol{a}_1 \\ \boldsymbol{b}_3 &= (2\pi/\Omega)\boldsymbol{a}_1 \times \boldsymbol{a}_2 \end{aligned}\right\} = b_i^{\alpha} = \frac{2\pi}{\Omega}\varepsilon_{ijk}\varepsilon^{\alpha\beta\gamma}a_j^{\beta}a_k^{\gamma} \tag{2.4}$$

ε_{ijk} and $\varepsilon^{\alpha\beta\gamma}$ are the totally antisymmetric LEVI–CIVITA tensors and the indices are $i, j, k = 1, 2, 3$ and $\alpha, \beta, \gamma = x, y, z$. From the definition of the vectors $\boldsymbol{b}_i$ it can be shown that the inner product is

$$\boldsymbol{a}_i \cdot \boldsymbol{b}_j = 2\pi\delta_{ij} \quad \text{with} \quad \delta_{ij} = \begin{cases} 1 \text{ if } i = j \\ 0 \text{ if } i \neq j \end{cases} . \tag{2.5}$$

This new basis defines the *reciprocal lattice*, which has the same dimension as the direct lattice. The reciprocal lattice vectors are given by

$$\boldsymbol{G} = \sum_{j=1}^{3} k_j \boldsymbol{b}_j, \tag{2.6}$$

where the k_j are again integer numbers. Together with Eq. (2.1) the important property of the reciprocal lattice can be found:

$$\begin{aligned} \boldsymbol{G} \cdot \boldsymbol{R} &= \sum_{i,j} n_i k_j \boldsymbol{a}_i \cdot \boldsymbol{b}_j \\ &= 2\pi \sum_{i} n_i k_i = 2\pi M, \quad M \in \mathbb{N}. \end{aligned} \tag{2.7}$$

It follows from Eq. (2.7), that:

$$\exp(i\boldsymbol{G} \cdot \boldsymbol{R}) = 1. \tag{2.8}$$

In reciprocal space the constructed WIGNER–SEITZ cell is called the *first* BRILLOUIN *zone*. Its volume can be obtained from the triple product of the three basis vectors:

$$\Omega_{\mathrm{B}} = \boldsymbol{b}_1 \cdot (\boldsymbol{b}_2 \times \boldsymbol{b}_3) \overset{(2.4)}{=} \frac{(2\pi)^3}{\Omega}. \tag{2.9}$$

Higher order zones, e.g. second or third BRILLOUIN zone, can be constructed by connecting the translation vector to the second–, third–nearest, etc. neighbors.

Solid State Hamiltonian

For a theory of solid state physics all forces but the COULOMB interactions are neglected. While it seems to be wrong to not consider the gravitational

force for large systems, the sample sizes of interest are still small and in the order of 10^{23} atoms. Only COULOMB interactions between the electrons (el) and nuclei (nuc) and a coupling between the two species (el–nuc) are assumed. In doing so, the following HAMILTONian can be derived:

$$\mathcal{H} = \mathcal{H}_{\text{nuc}} + \mathcal{H}_{\text{el}} + \mathcal{H}_{\text{el–nuc}}. \tag{2.10}$$

Neglecting relativistic effects like LAMB–shift, the three parts of the HAMILTONian can be written explicitly as:

$$\mathcal{H}_{\text{nuc}} = \sum_{i}^{N} \frac{\boldsymbol{P}_i^2}{2M_i} + \frac{1}{2}\sum_{i\neq j} \frac{e^2 Z_i Z_j}{|\boldsymbol{R}_i - \boldsymbol{R}_j|}, \tag{2.11}$$

$$\mathcal{H}_{\text{el}} = \sum_{i}^{ZN} \frac{\boldsymbol{p}_i^2}{2m_{\text{e}}} + \frac{1}{2}\sum_{i\neq j} \frac{e^2}{|\boldsymbol{x}_i - \boldsymbol{x}_j|}, \tag{2.12}$$

$$\mathcal{H}_{\text{el–nuc}} = -\sum_{i,j} \frac{e^2 Z_j}{|\boldsymbol{x}_i - \boldsymbol{R}_j|}. \tag{2.13}$$

In these equations $\boldsymbol{R}_i$ denotes the position operator of the N nuclei and $\boldsymbol{P}_i = -i\hbar\nabla_{\boldsymbol{R}_i}$ the momentum operators. The subscript $\boldsymbol{R}_i$ implies that the nabla operator only acts on the coordinates $\boldsymbol{R}_i$. $\boldsymbol{x}_i$ and $\boldsymbol{p}_i = -i\hbar\nabla_{\boldsymbol{x}_i}$ are the operators of the electrons respectively.

An exact HAMILTONian, like the one given above, is all that is needed to solve a quantum mechanical problem, i.e. determining its wave functions and corresponding eigenvalues. In reality things are somewhat different. Analytic solutions only exist in the case of one and two particles. Even numerical methods like the `VASP` code [71, 72, 69, 70] can only handle systems of a few hundreds of atoms. This is because the COULOMB interaction of the particles correlates the movement of all electrons and nuclei, so that a quantum mechanical many–body problem has to be solved. The calculation time for such problems scales exponentially with the number of particles, so that it cannot be solved for a significant number of atoms. A piece of metal, e.g. 1 cm^3, has already $\mathcal{O}(10^{23})$ atoms – an impossible task. Approximations to solve the above problem have to be made.

The Adiabatic Approximation

The *adiabatic approximation* is also known as BORN–OPPENHEIMER *approximation*. In fact, the nuclei mass is about 1,800 times larger than the

electrons mass. This implies that the average kinetic energy of the nuclei is much smaller than that of the electrons. Physically it means, that the electrons are able to instantaneously accommodate to the position of the nuclei. With this condition the adiabatic theorem can be used [112].

For the solid state HAMILTONian (2.10), the coordinates of the nuclei are functions of time $\boldsymbol{R}_i = \boldsymbol{R}_i(t)$ which change slowly (adiabatically) in comparison to the fast moving electrons. In the BORN–OPPENHEIMER approximation the HAMILTONian for the electrons is considered with fixed nuclei positions at every time t. For fixed t the SCHRÖDINGER equation

$$(\mathcal{H}_{\text{el}} + \mathcal{H}_{\text{el-nuc}})\psi_j(\boldsymbol{x}, \boldsymbol{R}) = E_j^{\text{el}}(\boldsymbol{R})\psi_j(\boldsymbol{x}, \boldsymbol{R}) \tag{2.14}$$

with $\boldsymbol{x} = (\boldsymbol{x}_1, \ldots, \boldsymbol{x}_{ZN})$, $\boldsymbol{R} = (\boldsymbol{R}_1, \ldots, \boldsymbol{R}_N)$ and $\boldsymbol{R}$ giving the instantaneous positions of the nuclei, has to be solved. It is assumed, that the electrons stay in the same eigenstate, e.g. the ground state ψ_0. The eigenfunctions for the complete HAMILTONian (2.10) can then be obtained through the product ansatz

$$\Psi(\boldsymbol{x}, \boldsymbol{R}) = \psi_0(\boldsymbol{x}, \boldsymbol{R})\Phi(\boldsymbol{R}). \tag{2.15}$$

After neglecting the non–adiabatic terms, the action of the HAMILTONian (2.10) to this ansatz leads to so–called *lattice dynamics* (phonons). The system is described by the following SCHRÖDINGER equation:

$$\left[\sum_{i=1}^{N} \frac{\boldsymbol{P}_i^2}{2M_i} + E_0^{\text{el}}(\boldsymbol{R}) + U_0(R)\right] \Phi(\boldsymbol{R}) = E\Phi(\boldsymbol{R}). \tag{2.16}$$

Nevertheless, the determination of the potential $U(\boldsymbol{R}) = E_0^{\text{el}} + U_0(\boldsymbol{R})$ still is an ambitious task.

The most important correction for the BORN–OPPENHEIMER approximation are not the non–adiabatic terms but comes from the incompleteness of the product ansatz, Eq. (2.15). A full ansatz takes all eigenstates j of the system into account:

$$\Psi(\boldsymbol{x}, \boldsymbol{R}) = \sum_j \psi_j(\boldsymbol{x}, \boldsymbol{R})\Phi(\boldsymbol{R}). \tag{2.17}$$

For non–infinitely slow moving nuclei, transitions between the electron eigenstates, given by terms of the form

$$\int \mathrm{d}^3x \psi_j^* \frac{\partial}{\partial \boldsymbol{R}_j} \psi_{j'} \tag{2.18}$$

occur. This is known as the electron–phonon coupling, describing how the movement of the nuclei leads to transitions between the electronic states j and j'. The electron–phonon coupling is needed later for the transfer of deposited heat by the laser from the electrons to the lattice in the Two–Temperature Model.

The above concepts are very general and are valid for gases, liquids or solids. However, as the main interest of this work lies in metals, properties of metals and alloys will be discussed in the next section.

2.1.1 Metals and Alloys

A very general definition of a metal is the following: It is a chemical element, that is a good conductor for electricity and heat. The *metallic bond* arises from the delocalized electrons surrounding the positive charged ions. Thus, the solid is held together by COULOMB interactions between its constituents. A look into the periodic table shows, that metals occupy the majority of it. A line drawn from boron (B) to polonium (Po) separates the metals (elements to the lower left) from the non–metals (elements to the upper right). For elements directly on the line, semiconductors are found. These elements share properties common from both conductors and insulators. Alternatively, metals can be defined via their band structure: If the energy bands of the material are filled with all available electrons and the top band is partly occupied, this material is a metal. The definition is somewhat more general and opens up the category for metallic polymers and other organic metals, which have been made by researchers and employed in high–tech devices.

Besides the high electrical and thermal conductivity, physical properties of metals are luster, a high density and the ability to deform under stress without cleaving. Most of the metals are extremely reactive, thus rarely found in their elemental metallic state. Due to the large number of free electrons, a metal is opaque, shiny and lustrous. Its microstructure makes it opaque for light waves in the optical range. Compared to non–metals, metals have on average higher densities. The tightly packed crystal lattice of the metallic structure is the reason for the high densities of most metals. Nonetheless, there is a wide variance of the densities throughout the periodic system.

The high electrical and thermal conductivity originates in the metallic bond: The valence electrons of the atoms form a gas of nearly free electrons,

moving as an electron cloud in the background of the ion cores. It will be shown later, that the mathematical calculations for a *free electron gas* lead to accurate predictions for the electron contribution to the heat capacity and conductivity.

Mechanical properties include a high ductility, originating from the metals capacity for plastic deformation. For elastic deformation HOOKE's law can be used for restoring forces. The stress–strain relation is a linear function. When the elastic limit is exceeded, the metal deforms permanently, known as plasticity. This irreversible change in atomic arrangement occurs as a result of the action of an applied force (tensile, compressive, shear bend or torsion forces) or by a change in temperature. The applied heat effects the mobility of structural defects like grain boundaries, point vacancies, line and screw dislocations or stacking faults. For an alloy two or more elements are combined[1]. Usually the major component in this solid solution is metal. A combination is especially interesting when it comes to practical use of the metal. The pure metal can either be too soft, brittle or chemical reactive. When different ratios of metals are combined, the desired properties of the resulting alloy can be *designed*. Generally, the aims are higher resistance to corrosion, different color, higher hardness or less brittleness.

During the last years *Complex Metallic Alloys* (CMAs) have become increasingly interesting for metal–based industries. They rely on materials based on elementary metals and binary metallic alloys. To tailor the properties for practical purposes, other elements are added. An example is the much smaller surface energy of highly complex intermetallics compared to the metallic constituents [113]. The reduced friction and wetting against polar liquids was taken as the best example of applications of CMAs. Three key features, which influence the properties of CMAs, can be found:

1. A large unit cell (up to hundreds or thousands of atoms).
2. The unit cell has a cluster substructure.
3. There is inherent disorder in various ways.

CMAs are formed with crystal structures based on giant unit cells. As a result, these materials can offer unique combinations of properties, which

[1] Alloys designed for very special demands like the application in jet engines may contain more than ten elements.

are excluded to conventional materials. CMAs are mentioned here because they show an affinity to quasicrystals (QCs). In Sec. 4.5 ablation is studied on an alloy, $Al_{13}Co_4$, which is an approximant to the decagonal phase of Al–Ni–Co.

Quasicrystals

Quasicrystals were discovered in 1984 by SHECHTMAN *et al.*, who observed a perfect fivefold X–ray diffraction pattern of an Al–Mn alloy [116]. This indicated a long–range order. The point group symmetry was that of the icosahedral group – a symmetry group that is not compatible with periodic order. Quasicrystals are structures that are both ordered and non–periodic. They form patterns that fill all the space but lack translational symmetry. In the classical theory of crystals only two–, three–, four– and sixfold rotational symmetries are allowed [67]. In the early 1960s aperiodic tilings, like the two–dimensional PENROSE tiling [101], were discovered by mathematicians. Twenty years later the relationship between the materials and the quasiperiodic tilings was recognized. Aside from the icosahedral quasicrystals also octagonal, dodecagonal or decagonal quasicrystals exist. The latter one is of special interest. Decagonal quasicrystals (d-QCs) are ordered periodically in one direction and quasi–periodically with eight–, ten– or twelvefold symmetry in the plane normal to it. Due to this structure, they combine properties from both, the periodic and the quasiperiodic world. It is shown later, that this stacking of quasiperiodic planes leads to an inherent anisotropy in most physical quantities.

2.1.2 Electrons in Metals

A lot of physical quantities could be understood by the model of the free electron gas. According to this theory, the weakly bound electrons can move freely through the crystal lattice. The valence electrons become conduction–band electrons. Many attributes of the metal – and also other materials – could be explained with the free electron gas years before the discovery of quantum mechanics. The classical theory was very helpful in deducting OHMs law and also the connection between the electrical and the thermal conductivity, known as WIEDEMANN–FRANZ law. However, other properties, like the magnetic susceptibility of the conducting electrons or the heat capacity cannot be explained by the classical theory.

Energy Levels of the Free Electron Gas

For a three–dimensional free electron the SCHRÖDINGER equation

$$-\frac{\hbar^2}{2m}\left(\frac{\partial^2}{\partial x^2}+\frac{\partial^2}{\partial y^2}+\frac{\partial^2}{\partial z^2}\right)\psi_{\boldsymbol{k}}(\boldsymbol{r})=E_{\boldsymbol{k}}\psi_{\boldsymbol{k}}(\boldsymbol{r}). \tag{2.19}$$

has to be solved. When confined in a rectangular box of length L and origin in one corner, the solution of Eq. (2.19) are standing waves:

$$\psi_{\boldsymbol{n}}(x,y,z)=A\sin\left(\frac{\pi n_x}{L}x\right)\sin\left(\frac{\pi n_y}{L}y\right)\sin\left(\frac{\pi n_z}{L}z\right), \tag{2.20}$$

with n_x, n_y and n_z being positive integers. It is convenient to claim a certain periodicity, i.e.

$$\psi(x+L,y,z)=\psi(x,y,z) \tag{2.21}$$

and also with respect to y and z. Wave functions conform with the above condition and also solving the SCHRÖDINGER equation are called plane waves:

$$\psi_{\boldsymbol{k}}(\boldsymbol{r})=\exp(i\boldsymbol{k}\cdot\boldsymbol{r}). \tag{2.22}$$

The components of the *wave vector* $\boldsymbol{k}$ satisfy the condition:

$$k_x=0,\pm\frac{2\pi}{L},\pm\frac{4\pi}{L},\ldots \tag{2.23}$$

Analogously for k_y and k_z, i.e. each component of $\boldsymbol{k}$ has the form $2n\pi/L$, where n is a positive or negative integer. These components of $\boldsymbol{k}$ together with the spin orientation m_s are the quantum numbers of the problem. It follows from Eq. (2.22) and (2.19) that the energy corresponding to the wave vector $\boldsymbol{k}$ is

$$E_{\boldsymbol{k}}=\frac{\hbar^2}{2m}\boldsymbol{k}^2=\frac{\hbar^2}{2m}(k_x^2+k_y^2+k_z^2). \tag{2.24}$$

Wave number $k=|\boldsymbol{k}|$ and wavelength λ are related over $k=2\pi/\lambda$. Looking at the ground state of N free electrons, the orbitals can be interpreted as points inside a sphere in $\boldsymbol{k}$–space. The energy on the surface of this sphere is called the FERMI–energy. With a radius of k_F the energy on the FERMI–surface is:

$$E_\mathrm{F}=\frac{\hbar^2}{2m}k_\mathrm{F}^2. \tag{2.25}$$

Inside the above defined FERMI–sphere the number of energy levels is equal to

$$2 \cdot \frac{4\pi k_\mathrm{F}^3/3}{(2\pi/L)^3} = \frac{V}{2\pi^2} k_\mathrm{F}^3 = N. \tag{2.26}$$

The factor 2 arises from the two possible values of the spin quantum number m_s for each value of $\boldsymbol{k}$. The FERMI radius is then a function of only the electron density:

$$k_\mathrm{F} = \left(\frac{3\pi^2 N}{V} \right)^{1/3}. \tag{2.27}$$

Together with Eq. (2.25) the FERMI energy can be related to the electron density N/V and its mass m:

$$E_\mathrm{F} = \frac{\hbar^2}{2m} \left(\frac{3\pi^2 N}{V} \right)^{2/3}. \tag{2.28}$$

From Eq. (2.28) the *density of states* is derived for the electrons by taking the derivative of N with respect to the energy E:

$$\mathcal{D}(E) = \frac{\mathrm{d}N}{\mathrm{d}E} = \frac{V}{2\pi^2} \left(\frac{2m}{\hbar^2} \right)^{3/2} E^{1/2}. \tag{2.29}$$

Heat Capacity of the Free Electron Gas

In the classical theory the electrons add $\frac{3}{2} N k_\mathrm{B}$ to the heat capacity of the electron gas – just as in a monoatomic ideal gas. Measurements show, that at room temperature the actual contribution of the electrons is less than 1% of the expected value. The correct equation was found by E. FERMI. Making the right conclusions, he said *"One recognizes that the specific heat vanishes at absolute zero and that at low temperatures it is proportional to the absolute temperature."* [67].

When heating up a sample from zero temperature, not all electrons gain the same amount of energy, which would be in the order of $k_\mathrm{B}T$. Instead, only the electrons in a small region $k_\mathrm{B}T$ around the FERMI energy get thermally activated. This is the solution to the above problem: In a system with N electrons, a small portion in the order of T/T_F are activated thermally. Only the electrons which lie inside a small range around the FERMI energy gain thermal energy in magnitude of $k_\mathrm{B}T$. Each of these NT/T_F

electrons has a thermal energy of $k_B T$. The total inner energy of the free electron gas is given by

$$U \approx \frac{NT}{T_F} k_B T. \tag{2.30}$$

The electrons add just a small portion to the specific heat that is proportional to T

$$C_{el} = \frac{dU}{dT} \approx \frac{N k_B T}{T_F}, \tag{2.31}$$

which is in good agreement with experiments. An exact equation for the specific heat, which is a function of the density of states at the FERMI energy E_F, can be derived [67]:

$$C_{el} = \frac{1}{3}\pi^2 \mathcal{D}(E_F) k_B^2 T = \frac{1}{2}\pi^2 N k_B T / T_F. \tag{2.32}$$

This dependency of C_{el} on the temperature is later used to simplify the equations of the Two–Temperature Model.

Thermal Conductivity of Metals

The thermal conductivity K for particles moving with velocity v is given by

$$K = \frac{1}{3} C v l, \tag{2.33}$$

where C is the specific heat per volume and l the mean free path length. Together with Eq. (2.32) the thermal conductivity for the FERMI gas is:

$$K_{el} = \frac{\pi^2}{3} \cdot \frac{n k_B^2 T}{m v_F^2} \cdot v_F \cdot l = \frac{\pi^2 n k_B^2 T \tau}{3m}. \tag{2.34}$$

With $l = v_F \tau$, n the electron density and τ their collision time. For pure metals the major part of the heat flux comes from the electrons and not from the phonons. Nevertheless, in contaminated metals or alloys the contribution from the phonons may become comparable to the electrons.

2.2 The Ablation Process

Theoretical and computational investigations of the laser ablation phenomenon are challenging tasks. The complex nature of the involved processes at different time and length scales makes it difficult to find an overall

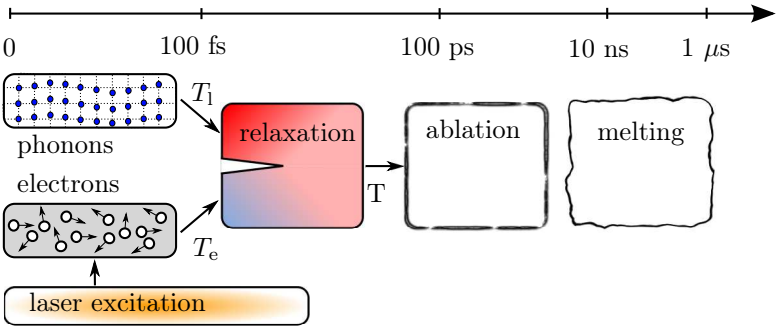

Figure 2.2: Time scales and processes of ablation in metals. After the pulse energy is absorbed, the electrons thermalize quickly (< 500 fs). Typical electron–lattice relaxation times are 5 ps. At this time the system can be described with a unified temperature. The ablation process and melt overflow take more than ten times as long.

model. A qualitative description of the ablation process includes primary elementary excitations of optically active states in a solid, thermalization of the deposited laser energy, formation of high–temperature and high–pressure regions, explosive disintegration and ejection of material, intensive processes in the ejected plume, propagation of a pressure wave into the bulk away from the surface, etc. It is impossible to address all the processes that occur within a single model. However, the macroscopic observations are always the same:

1. Laser energy is absorbed by the medium.
2. The energy is transformed into thermal vibrations.
3. In case the atoms have gained enough energy, emission of particles (electrons, ions, neutral atoms or molecules) can take place at the surface.
4. Under certain circumstances a plasma cloud is formed in front of the target.

What happens – and on which time scales – depends entirely on the material and the laser parameters like wave length or pulse duration. For metals

the time scales and processes are shown in Fig. 2.2. For a complete model four orders of magnitude in time have to be taken into account.

All events were caused by the incident laser light on the targets surface. The propagation of electromagnetic waves is governed by the MAXWELL equations [62]. For zero charge and current densities the wave equation can be derived from the inhomogeneous MAXWELL equations:

$$\frac{1}{c^2}\frac{\partial^2 \boldsymbol{E}}{\partial t^2} - \Delta \boldsymbol{E} = 0, \tag{2.35}$$

$$\frac{1}{c^2}\frac{\partial^2 \boldsymbol{B}}{\partial t^2} - \Delta \boldsymbol{B} = 0. \tag{2.36}$$

$\boldsymbol{E}$ and $\boldsymbol{B}$ are the electric and magnetic field vectors, c is the vacuum speed of light. The solutions to these equations are waves that propagate with the speed of light. The signal speed in a media is different and is determined by the permeability ϵ and permittivity μ of the material. The ratio of the vacuum speed of light to the one in a media is called *index of refraction*:

$$n' = n + ik = \sqrt{\frac{\epsilon\mu}{\epsilon_0\mu_0}}. \tag{2.37}$$

Generally n and k are frequency dependent quantities, ϵ and μ are functions of $\boldsymbol{E}$ and $\boldsymbol{B}$. In media with absorption the imaginary part of Eq. (2.37) leads to a damping of the wave according to LAMBERT–BEERs law:

$$E_x = E_0 e^{-\alpha x} = E_0 e^{-x/l_\alpha}. \tag{2.38}$$

l_α is the characteristic absorption length along the direction of propagation of the wave.

Initially, the laser energy is absorbed by the metal from the free or weakly bound electrons. After some femtoseconds the electron gas is thermalized via electron–electron collisions. In the frame of the FERMI liquid theory the electron–electron scattering time for an electron with energy E is defined by

$$\tau_{\mathrm{ee}} = \frac{1}{a(E - E_{\mathrm{F}})^2 + b(k_{\mathrm{B}}T_{\mathrm{e}})^2} \tag{2.39}$$

where a and b are independent of E and T_{e} [11]. In the case of laser excitations, the electrons' energy is approximately the FERMI energy. In addition, the temperature can rise above 15,000 K. In consequence τ_{ee} becomes

small. The physical reason for this short time can be given in k–space: The phase–space for scattering is huge and is not restricted to PAULIs principle since there are many empty places for scattering events. After thermalizing, a temperature T_e can be assigned to the electrons according to the FERMI–DIRAC distribution. Only the reduction of the quantum mechanical many–body system to a single thermodynamic quantity allows a macroscopic description.

Due to their inertia, the ions cannot follow the fast oscillating electromagnetic field of the laser. Still, the ions gain kinetic energy from collisions with the hot electrons. The mass difference between the electrons and ions is huge, therefore, only a small portion of the energy is transferred per collision. The electron–lattice relaxation time can be calculated by

$$\tau_{el} = \frac{\gamma T_e}{\kappa} \tag{2.40}$$

with γ the electron constant of specific heat, T_e the electron temperature and κ the electron–phonon coupling constant [3]. The equation can be used to estimate the time scales of electron–lattice thermalization and is usually one order of magnitude larger than τ_{ee}. For metals with strong electron–phonon coupling like iron τ_{el} is around 0.5 ps, while for aluminum τ_{el} is approximately 5 ps [58].

In general the laser affected zone is small compared to the whole sample, thus only a local equilibrium exists. The energy transfer to regions deeper inside the system again takes place by collisions between the electrons.

Depending on the time scales of interest, the electron–electron collisions self have to be considered [107]. For the systems and pulses under study in this work, all times were considerably longer than τ_{ee}, therefore, a classical description of heat conduction can be applied.

2.2.1 Heat Conduction

For a stationary solid the energy balance can be expressed as

$$c(T)\rho\frac{\partial T}{\partial t} + \nabla \cdot \boldsymbol{q} = Q(\boldsymbol{x}, t), \tag{2.41}$$

where ρ is the mass density, $c(T)$ is the specific heat at a given temperature T, $\boldsymbol{q}$ is the thermal heat flux vector and $Q(\boldsymbol{x}, t)$ is the heat source. It is

assumed that the light energy is absorbed within the medium and is totally transformed into heat. The source term can then be written as

$$Q(\boldsymbol{x},t) = -\nabla\langle \boldsymbol{S}(\boldsymbol{x},t)\rangle + U(\boldsymbol{x},t). \tag{2.42}$$

$U(\boldsymbol{x},t)$ describes the additional energy that is required or provided in phase changes or if chemical reactions take place. It will be neglected for all further calculations. $\langle \boldsymbol{S}\rangle = c\langle \boldsymbol{E}\times\boldsymbol{H}\rangle/4\pi$ is the time average of the POYNTING vector. For monochromatic light absorbed in an isotropic medium, $-\nabla\langle \boldsymbol{S}\rangle$ equals the well–known LAMBERT–BEER law [14]. In case of an isotropic and homogenous material, FOURIERs linear approximation $\boldsymbol{q} = -K\nabla T$ of the heat flux can be inserted in Eq. (2.41). The combination leads to the FOURIER equation of heat conduction:

$$\frac{\partial T}{\partial t} = \beta\nabla^2 T + Q(\boldsymbol{x},t), \tag{2.43}$$

where K is the thermal conductivity and $\beta = K/c\rho$ the thermal diffusivity. The heat conduction of the electrons is around 100 times larger than from the ions [21]. Thus K can be written as the heat conductivity of the electrons K_e only.

For the problem given in Eq. (2.43), analytic solutions exist for very special boundary conditions and heat sources $Q(\boldsymbol{x},t)$ only. A solution for a point source $Q(\boldsymbol{x},t) = Q_0\delta(\boldsymbol{x},t)/\beta$ in infinite space can be derived from the linear heat equation. For three dimensions the GREENs function is of the form [24]:

$$T(\boldsymbol{x},t) = \frac{Q_0}{8(\pi\beta t)^{3/2}} \exp\left\{-\frac{|\boldsymbol{x}|^2}{4\beta t}\right\}. \tag{2.44}$$

For a more general heat source $S(\boldsymbol{x}',t')$ and an infinite sample it follows from superposition that

$$T(\boldsymbol{x},t) = \int_{t'=0}^{t} \iiint \frac{S(\boldsymbol{x}',t')}{8(\pi\beta)(t-t')^{3/2}} \exp\left\{-\frac{|\boldsymbol{x}-\boldsymbol{x}'|^2}{4\beta(t-t')}\right\} \mathrm{d}^3\boldsymbol{x}'\,\mathrm{d}t'. \tag{2.45}$$

For specific, e.g. finite, geometries or more complex heat sources the solutions rapidly get complicated, so that numerical methods are applied for most practically relevant problems [45].

2.3 The Two-Temperature Model (TTM)

As already mentioned, the diffuse heat conduction into bulk material is governed mainly by the electrons. Together with the heat conduction equation (see Sec. 2.2.1) a solution for the temperature evolution of the electrons in a laser heated metal can be derived. However, this is only half of the truth. The melting, pressure waves and most ablation phenomena are happening because the crystal lattice breaks down. Thus, a description for the temperature of the phonons is needed.

For the calculations of the electron and phonon temperatures after ultrashort laser irradiation the Two–Temperature Model (TTM) has been established [7]. The continuous model describes the time evolution of the temperatures of the sub–systems by inhomogenous coupled partial differential equations

$$C_\mathrm{e}(T_\mathrm{e})\frac{\partial T_\mathrm{e}}{\partial t} = \nabla\left[K_\mathrm{e}(T_\mathrm{e})\nabla T_\mathrm{e}\right] - \kappa(T_\mathrm{e}-T_\mathrm{l}) + S(\mathbf{x},t), \tag{2.46}$$

$$C_\mathrm{l}(T_\mathrm{l})\frac{\partial T_\mathrm{l}}{\partial t} = \nabla\left[K_\mathrm{l}(T_\mathrm{l})\nabla T_\mathrm{l}\right] + \kappa(T_\mathrm{e}-T_\mathrm{l}) \tag{2.47}$$

where C and K are the heat capacity and thermal conductivity of the electrons (C_e,K_e) and the lattice (C_l,K_l). κ is the electron–phonon coupling constant and $S(\boldsymbol{x},t)$ is the laser source term, which for historical reasons will be written as $S(\boldsymbol{x},t)$ instead of $Q(\boldsymbol{x},t)$. It can be seen, that for constant K_e, Eq. (2.46) is the heat conduction equation (2.43) with the additional term $\kappa(T_\mathrm{e}-T_\mathrm{l})$. The lattice temperature T_l is described with the same differential equation. In most cases the phonon diffusion $\nabla[K_\mathrm{l}(T_\mathrm{l})\nabla T_\mathrm{l}]$ can be neglected due to the small phonon temperature gradient.

The essential new quantity is the electron–phonon coupling constant κ. κ can be measured and calculated in different ways [20]. This will be important in Sec. 4.5, were κ is needed for $Al_{13}Co_4$ for which κ has not been measured yet. It is therefore very useful to compare methods to estimate κ. The electron–phonon coupling also is an important quantity in the theory of superconductivity. It can be shown that its value is related to the transition temperature of superconductors [84].

Following the work of Wang *et al.*, a relation for κ is given by [133]:

$$\kappa = \frac{\pi^4(k_B v_\mathrm{s} n_\mathrm{e})^2}{18 L \sigma_\mathrm{e}(T_\mathrm{e}) T_\mathrm{e}}, \tag{2.48}$$

where v_s is the speed of sound, n_e the electron–density, σ_e the electrical conductivity and L the LORENZ number known from the WIEDEMANN–FRANZ law. A second equation was derived by ALLEN, comparing the relaxation rate of the electron temperature T_e to the electron–phonon enhancement parameter $\lambda(T)$ and the averaged square of the phonon frequency $\langle\omega^2\rangle$ using standard scattering formulas [3]:

$$\kappa = \frac{3\hbar\gamma\lambda\langle\omega^2\rangle}{\pi k_B}. \tag{2.49}$$

The electron–phonon enhancement of the diffusion thermopower can be written as [65]:

$$\frac{S}{T} = \frac{S_0}{T}\left[1 + \lambda(T)\right], \tag{2.50}$$

where S_0 is the thermopower in the absence of electron–phonon interactions. The electron–phonon mass enhancement parameter $\lambda(T)$ is given by

$$\lambda(T) = \int_0^\infty \frac{\alpha^2(\omega)F(\omega)}{\omega} G\left(\frac{\hbar\omega}{k_B T}\right) \mathrm{d}\omega. \tag{2.51}$$

$G(\hbar\omega/k_B T)$ is a universal function, introduced by KAISER and $\alpha^2 F(\omega)$ is the ELIASHBERG function [65]. $F(\omega)$ is the phonon density of states and α^2 an average of the electron–phonon interaction. It can be seen from Eq. (2.51) that a lot of theoretical and experimental knowledge is needed to calculate exact values for the electron–phonon coupling κ. Taking all functional dependencies into account is beyond the scope of this work. However, with formula (2.50), the electron–phonon coupling can be related to the SEEBECK–coefficient S of thermoelectric power. It can be measured by standard temperature–gradient techniques, which later on will be very useful for the treatment of $Al_{13}Co_4$ in Sec. 4.5.

The Simplified Two–Temperature Model (sTTM)

In general, all parameters in the TTM equations (2.46) and (2.47) are temperature dependent. An analytic solution cannot be given.

When thin metal films of 100 nm thickness and below are heated by laser radiation, the temperature gradients between the surface and the back side can be neglected [61]. With the approximation of constant specific heat

and an instantaneous heating of the electrons, analytic expressions for $T_\mathrm{e}(t)$ and $T_\mathrm{l}(t)$ can be derived. In this case the TTM equations simplify to

$$-C_\mathrm{e}\frac{\partial T_\mathrm{e}}{\partial t} = C_\mathrm{l}\frac{\partial T_\mathrm{l}}{\partial t} = \kappa(T_\mathrm{e} - T_\mathrm{l}). \tag{2.52}$$

The ansatz

$$\begin{aligned} T_\mathrm{e}(t) &= Ae^{-t/\tau} + T_\infty, \\ T_\mathrm{l}(t) &= Be^{-t/\tau} + T_\infty \end{aligned} \tag{2.53}$$

with a relaxation constant τ and the equilibrium temperature T_∞ is chosen. It follows from Eq. (2.52) that

$$\tau = \frac{C_\mathrm{e}C_\mathrm{l}}{\kappa C_\mathrm{e} + C_\mathrm{l}} = \frac{C_\mathrm{r}}{\kappa} \tag{2.54}$$

with the reduced heat capacity C_r. Usually C_e is much smaller than C_l, thus τ can be written as $\tau = C_\mathrm{e}/\kappa$. This is the already known relaxation time, given in Eq. (2.40). Together with initial conditions

$$T_\mathrm{e}(0) = T_\mathrm{e}^0, \tag{2.55}$$

$$T_\mathrm{l}(0) = T_\mathrm{l}^0 \tag{2.56}$$

the solutions for the sTTM are

$$T_\mathrm{e}(t) = \left(\frac{T_\mathrm{e}^0 - T_\mathrm{l}^0}{\frac{C_\mathrm{e}}{C_i} + 1}\right) e^{-t/\tau} + T_\infty, \tag{2.57}$$

$$T_\mathrm{l}(t) = \left(\frac{T_i^0 - T_\mathrm{e}^0}{\frac{C_i}{C_\mathrm{e}} + 1}\right) e^{-t/\tau} + T_\infty. \tag{2.58}$$

The solutions can be seen for a given set of parameters in Fig. 2.3. The equilibrium temperature T_∞ turns out to be a weighted average of the two initial temperatures:

$$T_\infty = T_\mathrm{e}^0\frac{C_\mathrm{e}}{C_\mathrm{e} + C_\mathrm{l}} + T_\mathrm{l}^0\frac{C_\mathrm{l}}{C_\mathrm{e} + C_\mathrm{l}}. \tag{2.59}$$

For larger samples the diffusive part in Eq. (2.46) cannot be neglected anymore. Additionally, for real systems all parameters have a temperature

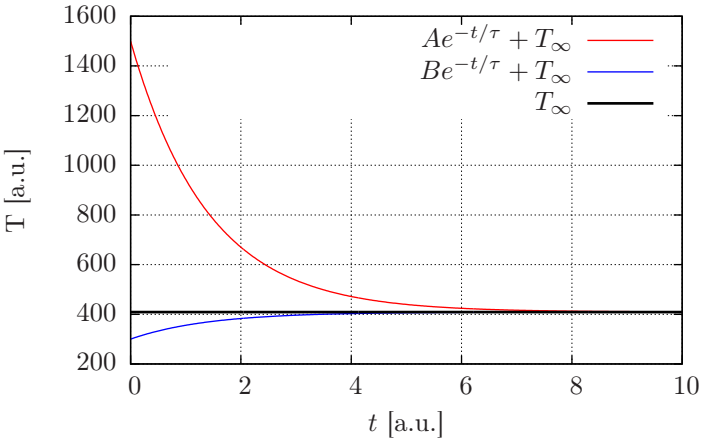

Figure 2.3: Solutions for the simplified TTM. The parameters are $C_\mathrm{e} = 1$, $C_\mathrm{l} = 10$, $T_\mathrm{e}(0) = 1500$, $T_\mathrm{l}(0) = 300$ and $\kappa = 0.65$. The equilibrium temperature $T_\infty = 409$ is reached after approximately four relaxation times $\tau = 1.4$.

dependence. Although analytic models exist, it is difficult to find equations for the parameters valid over a large temperature range [9, 132]. Tabulated functions, gathered from experiments or from complex simulations have to be used [78, 79]. However, there are more pitfalls within the Two–Temperature Model.

2.3.1 The Extended Two–Temperature Model (eTTM)

The Two–Temperature Model as it was introduced by Anisimov [7] and discussed in the last section has an intrinsic shortcoming. As it is based on the classical Fourier law of heat conduction, it assumes an infinite speed of propagation for the heat. One of the implications of the theory of relativity is the principle of *no action at a distance*. A finite speed of propagation for any given signal is needed [109]. The basic idea can be traced back to Maxwell [83]. He derived Fouriers law with an additional term

$$\tau_\mathrm{th} \frac{\partial \boldsymbol{q}}{\partial t} + \boldsymbol{q} = -K \nabla T. \tag{2.60}$$

τ_{th} is a relaxation time of the heat conducting medium. MAXWELL concluded that *"The first term may be neglected, as the rate of conduction will rapidly establish itself."*. 150 years ago this might have been true, but does not hold for todays femtosecond time scales. It is not clear what this characteristic time τ_{th} is. ZHANG *et al.* argue, that τ_{th} is the relaxation time needed for the target temperature to reach a new equilibrium after the surface experiences a very high temperature gradient [139]. Other interpretations are that of a mean free time in the energy carriers' collision process [131]. For metals the free electron relaxation time can be used as a typical relaxation time. Eq. (2.60) was rediscovered in 1958 by CATTANEO and VERNOTTE. A modern derivation can also be given in the framework of extended thermodynamics [64].

It is argued in the literature, that the TTM fails to make correct predictions on the sub–picosecond time scale [49, 115]. In contrast, other authors conclude that the TTM also is valid to describe the physics for ultra short pulses [135, 56]. However, an extended version of the Two–Temperature Model (eTTM) is given on the basis of Eq. (2.60) by HÜTTNER [57]. Together with the energy conservation law

$$\nabla \cdot \boldsymbol{q} = -C_e \frac{\partial T_{\mathrm{e}}}{\partial t} + S(\boldsymbol{x}, t) - \kappa(T_{\mathrm{e}} - T_{\mathrm{l}}) \tag{2.61}$$

the eTTM equations can be derived. The general FOURIER equation (2.60) is re–written to

$$\left(1 + \tau_{\mathrm{th}} \frac{\partial}{\partial t}\right) \nabla \cdot \boldsymbol{q} = -\nabla K_{\mathrm{e}} \nabla T_{\mathrm{e}}. \tag{2.62}$$

The combination with Eq. (2.61) leads to a hyperbolic partial differential equation for the electron temperature:

$$\begin{aligned} C_{\mathrm{e}} \tau_{\mathrm{th}} \frac{\partial^2 T_{\mathrm{e}}}{\partial t^2} + C_{\mathrm{e}} \frac{\partial T_{\mathrm{e}}}{\partial t} &= \nabla \left[K_{\mathrm{e}} \nabla T_{\mathrm{e}}\right] + \left(1 + \tau_{\mathrm{th}} \frac{\partial}{\partial t}\right) S(\boldsymbol{x}, t) \\ &\quad - \left(1 + \tau_{\mathrm{th}} \frac{\partial}{\partial t}\right) \kappa (T_{\mathrm{e}} - T_i). \end{aligned} \tag{2.63}$$

The above equation is similar to the telegrapher's equation, which also has a second derivative in time. It is a more general form of the wave equation and was initially used to describe the signal propagation in undersea cables.

For the phonon part, the equation stays unchanged as proposed in the TTM, Eq. (2.47). Physically the heat flow occurs within a characteristic

time τ_{th}, because it cannot be established within arbitrary short times. In the limit of $\tau_{\mathrm{th}} \to 0$, the old TTM equations are obtained.

It was shown by METZLER *et al.*, that the eTTM possesses a principal solution with a ballistic behavior at very short times [86]. A diffusive model like the TTM predicts a linear time dependence for the mean square of the thermal displacement. For ballistic motion a time dependence proportional to t^2 is observed.

At least for aluminum the standard Two–Temperature Model can be used because τ_{th} is small. HÜTTNER gives a value for the electron relaxation time with 67 fs, which is comparatively small [58]. However, one has to keep in mind, that for larger τ_{th}, e.g. for copper, which has as temperature relaxation time of 467 fs, the TTM may not be the appropriate model anymore.

Chapter 3

Numerical Methods and Implementation

The methods necessary for a laser ablation simulation are discussed in this chapter. In the beginning a short introduction to *ab initio* calculations is given. These complicated quantum mechanical methods are used to create interaction potentials for computer simulations. A description of molecular dynamics follows, then a model for the energy deposition of the laser is given. The simple model is improved in the last section, where the Two–Temperature Model (TTM) is combined with molecular dynamics to a hybrid simulation scheme.

3.1 Atomistic Computer Simulations

Ab Initio Calculations and Force Matching

The phrase *ab initio* has its origin in the Latin language, meaning *from the beginning*. Thus, depending on the branch of science, it has different senses: In chemistry an *ab initio synthesis* is based on fundamental chemicals only. In aerospace an *ab initio education* is from the very beginning, i.e. from a pedestrian to an aviator. In physics, usually the SCHRÖDINGER equation

$$\hat{H}|\psi\rangle = i\hbar\frac{\partial}{\partial t}|\psi\rangle \tag{3.1}$$

has to be solved for a many–body system to arrive at an *ab initio calculation*. The solutions for the eigenvalue problem (3.1) are the energies and corresponding wave functions of the system. The SCHRÖDINGER equation has no further parameters beyond natural constants and the types and positions of the atoms, giving the methods the prefix *ab initio* or *first–principle* calculations. Many quantum mechanical problems, especially for

solid state physics, fit the conditions described in sec. 2.1, so that the equations can be further simplified. Nevertheless, as simple as equation (3.1) may look, it cannot be solved for significantly more than 100 or 1000 atoms. More precisely, a reasonable sized laser ablation simulation based on pure ab initio methods can not be carried out in an acceptable time. *Effective potentials* for bigger simulations have to be used – ab initio data and the *force matching method* will be applied for their generation [38].

The method can be described in a few sentences, yet its application is a very demanding task. α indicates an entire set of L parameters $\alpha_1, \ldots, \alpha_L$, which are used to characterize the effective potentials, e.g. parameters for a LENNARD–JONES potential or a set of points to describe a function. A force database is built by using ab initio pseudo potential calculations, done with an ab initio code like `VASP` [71, 72, 69, 70]. Ideally different structures and conditions, like stressed or molten samples, free surfaces, vacancies etc. are included in the database. The *optimal* set of parameters $\langle\alpha\rangle$ is then found by trying to match the ab initio forces to the effective potentials. Simultaneously the data is fitted to experimental values as cohesive energies, vacancy formation energy or elastic constants. Mathematically, this reduces to a non–linear minimization problem in a L–dimensional space with an objective function given by

$$Z(\langle\alpha\rangle) = Z_{\text{forces}}(\langle\alpha\rangle) + Z_{\text{exp. data}}(\langle\alpha\rangle), \tag{3.2}$$

where Z is the mean square error in the fitting. There is a very powerful tool, called `potfit`, already available which does exactly the above process [19]. `potfit` is able to fit data for all sorts of potentials, which can then be used in large–scale molecular dynamics simulations.

Molecular Dynamics Simulations

Although it is possible to predict material properties from ab initio simulations to high accuracy, the method has an immense drawback. The large computational times required for these calculations make them unpractical for typical simulations, e.g. material failure. The system sizes which can be simulated on modern computers still are in the order of a few hundreds of atoms – which is way too small. In the case of molecular dynamics (MD) simulations the system is simplified by not treating the ions and electrons separately. The modeled atoms do not have inner degrees of freedom anymore, they interact as classical particles with each other. For the solution

of the many–body problem, the classical HAMILTONian equations of motion are integrated. In general, for a $N-$particle system, this leads to $6N$ first order differential equations. Let

$$\mathcal{H}(\boldsymbol{p}_1, \ldots, \boldsymbol{p}_N, \boldsymbol{r}_1, \ldots, \boldsymbol{r}_N) = \sum_{i=1}^{N} \frac{\boldsymbol{p}_i^2}{2m_i} + U(\boldsymbol{r}_1, \ldots, \boldsymbol{r}_N) \tag{3.3}$$

be the HAMILTONian of a configuration of N classical particles, $U(\{\boldsymbol{r}_i\})$ being the potential. The equations of motion then become:

$$\dot{\boldsymbol{r}}_j = \frac{\boldsymbol{p}_j}{m_j}, \quad \dot{\boldsymbol{p}}_j = \boldsymbol{F}_j = -\nabla_{\boldsymbol{r}_j} U(\{\boldsymbol{r}_i\}). \tag{3.4}$$

The force $\boldsymbol{F}_j = \dot{\boldsymbol{p}}_j$, acting on atom j, is calculated by taking the gradient of the potential U with respect to the coordinate $\boldsymbol{r}_j$. These equations cannot be solved analytically for large N. Instead, the equations are discretized in time: For a given configuration (coordinates and momenta) at time t, the forces on all the atoms are calculated. After this, their positions and momenta are adjusted accordingly for $t + \delta t$ (see Fig. 3.1). The time step δt is not arbitrary, in contrast, it has to be suitable for the underlying problem. While for a simulation of the universe a time step of years might be adequate [120], femtoseconds or even less are necessary for atomistic simulations. The time step has to be smaller than the time scales of characteristic motions to be resolved in the system. This dictates an upper bound for δt. For atomistic simulations of solids a time step between 0.1 and 2 fs has been established. There are well–known algorithms like GAUSS, RUNGE–KUTTA or VERLET in the literature which are used to solve ordinary first order differential equations. The latter one is applied in the code `IMD` [121] which was used throughout this work. Details on the implementation can be seen for example in *Numerical Recipes* [103].

Solving the standard HAMILTON equations characterizes a system which does not exchange particles (N), volume (V) or energy (E) with its environment. In statistical mechanics, a system like this is called *microcanonical ensemble*. However, there are situations (e.g. the phase diagram calculations in Sec. 4.1) when energy or pressure control is required. Usually this is achieved by introducing a coupling constant to an external heat bath. This reservoir allows the control of temperature during the simulation (NVT), which is equivalent to the *canonical ensemble* in thermodynamics [95, 96].

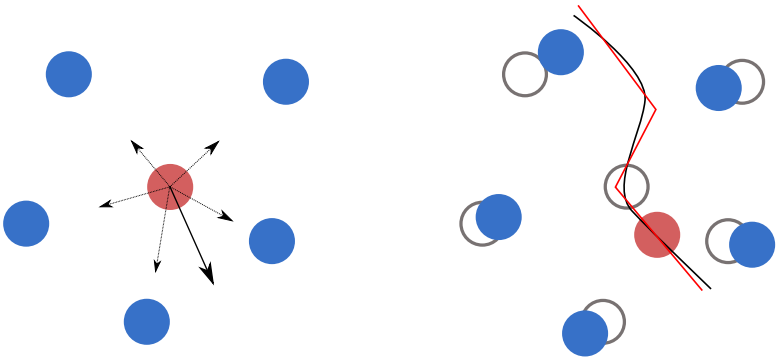

Figure 3.1: Scheme of a molecular dynamics (MD) simulation. First the net–force on a single participant for a given configuration is calculated (left side). This is done for all particles before their positions are adjusted accordingly (right side). By repeating this scheme, a trajectory is generated.

By the coupling of an additional volume reservoir, the pressure can be controlled during the simulation (NPT).

For the solution of Eq. (3.4) a potential has to be specified. A general potential is given by taking multi–body contributions into account. The potential energy can be expanded in a part from an external potential, a pair term, a three body term and so on. This leads to:

$$U(\{\boldsymbol{r}_j\}) = \sum_i \phi_1(\boldsymbol{r}_i) + \frac{1}{2}\sum_{\substack{i,j \\ i\neq j}} \phi_2(\boldsymbol{r}_i, \boldsymbol{r}_j) + \frac{1}{6}\sum_{\substack{i,j,k \\ i\neq j\neq k \\ i\neq k}} \phi_3(\boldsymbol{r}_i, \boldsymbol{r}_j, \boldsymbol{r}_k) + \dots \quad (3.5)$$

In this work only EAM potentials were used. The potentials are assumed to be isotropic and homogeneous, i.e. their dependence on the atomic coordinates is restricted to the euclidian distance $r_{ij} = |\boldsymbol{r}_i - \boldsymbol{r}_j|$. The potential energy of the system is thus

$$U(\{\boldsymbol{r}\}) = \frac{1}{2}\sum_{\substack{i,j \\ i\neq j}} \phi_{s_i s_j}(r_{ij}), \qquad i,j = 1,\dots N \quad (3.6)$$

where the pair potential ϕ_{ij} only depends on the species $s_{i,j}$ of atoms i and j. Although pair potentials are probably the simplest ones, still

many systems like noble gas solids, metals or liquids can be described very well. More information about pair potentials and molecular dynamics applications in general can be found in textbooks like the one of Allen and Tildesley [2].

Embedded Atom Method (EAM) Potentials

The embedded atom method (EAM) potential, which was originally modeled by Daw and Baskes [32], will now be introduced. The EAM approach is related to the second moment approximation to the tight binding theory, also known as the Finnis–Sinclair model and is particularly appropriate to describe metals and metallic alloys. The total energy of the system can be written as:

$$U = \sum_i U_i \tag{3.7}$$

with

$$U_i = \frac{1}{2} \sum_{i \neq j} \phi(r_{ij}) + F(n_i). \tag{3.8}$$

$\phi(r)$ is the pair potential, $F(n)$ is the embedding energy function and n_i is the total *atomic density* at the atom i from the surrounding atoms. It is assumed that

$$n_i = \sum_{i \neq j} \rho(r_{ij}). \tag{3.9}$$

While the original authors identify the n_i with the local electronic density and the repulsive pair term with the screened Coulomb interactions from the nuclei, alternative views exists. Potentials that can be written as in Eq. (3.8) show certain invariance properties. In monatomic system the potential is invariant under the transformation

$$\begin{aligned} \phi(r) &\rightarrow \phi(r) + 2\lambda\rho(r) \\ F(n_i) &\rightarrow F(n_i) - \lambda n_i, \quad \text{with} \quad n_i = \sum_{i \neq j} \rho(r_{ij}), \end{aligned} \tag{3.10}$$

where λ is an arbitrary real number [37]. A linear embedding function F can be entirely replaced by pair potentials. An energy contribution linear in n can always be shifted from one function to another. Thus, assigning any physical meaning (like the electronic density suggested initially) to

each of these functions seems false. From that conclusion it can be seen that only quantities that are invariant under the above transformation are physically relevant.

The gauge invariance can be generalized to a system with m different species, in which $m+1$ gauge degrees of freedom exist. When comparing different potentials, these invariances have to be fixed. Force calculations for EAM potentials take more computing time than standard pair potentials. Nevertheless, a lot of metallic systems cannot be sufficiently described by pair potentials only. The Embedded Atom Method was successfully applied to many systems, see e.g. DAW, FOILES and BASKES [33] for an overview.

More empirical interatomic potentials exist in the literature. Two that are also included in the IMD code are the STILLINGER–WEBER [122] and the TERSOFF potential [123]. The former was originally used to describe interactions in solid and liquid forms of silicon. The potential energy function comprises both two– and three–atom contributions. The other one was designed for multi–component systems, interpolating between potentials for the different elements to treat heteronuclear bonds. It was successfully applied to C–Si and Si–Ge systems. These potentials can also be used in ablation simulations, at least with the method described in the next section.

3.2 The Direct Approach: Rescaling the Kinetic Energy

Phenomenologically all laser heated materials behave the same: They heat up in the laser affected zone. Nevertheless, depending on the material, different coupling mechanisms are involved. For metals the laser field excites electrons into the conduction band [14], which then transfer energy to the lattice via electron phonon–coupling. For organic materials the mechanisms are different. The photons excite vibrational states and induce photochemical fragmentation [143]. If the physical mechanisms involved are not known — or too complicated for a computer simulation — a modeling of the macroscopic behavior can be a workaround.

For this approach, the temperature near the surface has to be increased during the simulation. The temperature of a system is related to the aver-

age kinetic energy of its atoms via

$$\langle E_{\text{kin}} \rangle = \frac{f}{2} k_{\text{B}} T, \tag{3.11}$$

where f is the number of degrees of freedom, $f = 3$ in the existing case. The basic idea of the *direct approach* is a rescaling of the kinetic energy of the atoms. After each time step δt the momentum vector $\boldsymbol{p}_i$ of the i–th atom is rescaled accordingly, leading to an immediate rise in temperature. The amount of energy that is absorbed by the lattice atoms can be determined by taking the equations of the Two–Temperature Model into account. The power density $S(\boldsymbol{x}, t)$, which serves as a source term in the heat–conduction equation of the electrons, stays the same for the rescale model. A general form for the power density contains an amplitude factor S_0, an absorption law $d(x)$, an intensity distribution on the surface $I(y, z)$, consideration of the reflectivity $(1 - R)$ and the temporal beam shape $f(t)$:

$$S(\boldsymbol{x}, t) = (1 - R) S_0 d(x) I(y, z) f(t). \tag{3.12}$$

For the absorption $d(x)$ the Lambert–Beer law is used, where α is the inverse absorption length. The intensity $I(y, z)$ can be adjusted according to the problem, while the temporal distribution $f(t)$ is assumed with a Gaussian shape:

$$S(\boldsymbol{x}, t) = (1 - R) S_0 \alpha e^{-\alpha x} I(y, z) e^{-\frac{(t - t_0)^2}{2\sigma_t^2}}. \tag{3.13}$$

The power density $S(\mathbf{x}, t)$ is multiplied by the time step δt and is divided by the average atomic density ρ_n to achieve a small energy difference. After each time step δt that amount of energy is added to the kinetic energy of the i-th particle:

$$E_{\text{kin}}^i(t + \delta t) = E_{\text{kin}}^i(t) + \frac{\delta t}{\rho_n} S(\mathbf{x}_i, t). \tag{3.14}$$

The atomic number density ρ_n can be calculated on–the–fly by averaging the atomic masses over the irradiated volume. This density is assumed as constant for pulses less than 1000 fs. For significantly longer pulses the material may change its phase, which results in a time dependent density $\rho_n(t)$.

The huge advantage of this model clearly lies in its simplicity: No knowledge of material properties like electron–phonon coupling or processes during ablation are needed. Heat transfer, melting or vaporization are all governed by the potentials used for the molecular dynamics. It will be shown later, that especially for inhomogeneous intensities this model is an ideal starting point (see Sec. 4.4). However, the lack of electronic heat conduction — the dominant part in metals — makes it somewhat limited for applications in metals and more complex systems. First and foremost anisotropic systems, both structural and thermo–conductive, cannot be treated without a proper model of the electrons.

3.3 A Hybrid Approach with the Two–Temperature Model

The great advantage of a pure molecular dynamics simulation is that only details of the interatomic potentials are needed. No assumptions have to be made about the processes under investigation. However, it is not directly applicable for simulations of laser interactions with metals. In metals the electronic contribution to the thermal heat conduction is dominant, thus the classical MD method, where only heat conduction via the lattice is present, underestimates the total thermal conductivity. The result is an unphysical confinement of the deposited laser energy near the sample's surface. The problem of over–heating has been recognized by Ohmura *et al.* in first simulations of laser ablation [97]. Later a modified method, in which the simulation box was divided into small blocks in which Fouriers law was applied to account for the heat conduction between adjacent cells, was suggested [98]. The following model aims to overcome these problems by combining the advantages of MD and TTM for a more realistic description of the physics involved.

The Two–Temperature Model describes the temperature evolution of the lattice and the electrons with two coupled partial differential equations (see Sec. 2.3) [7]. The two equations are

$$C_\mathrm{e}(T_\mathrm{e})\frac{\partial T_\mathrm{e}}{\partial t} = \nabla\left[K_\mathrm{e}(T_\mathrm{e})\nabla T_\mathrm{e}\right] - \kappa(T_\mathrm{e} - T_\mathrm{l}) + S(\boldsymbol{x}, t), \tag{3.15}$$

$$C_\mathrm{l}(T_\mathrm{l})\frac{\partial T_\mathrm{l}}{\partial t} = \nabla\left[K_\mathrm{l}(T_\mathrm{l})\nabla T_\mathrm{l}\right] + \kappa(T_\mathrm{e} - T_\mathrm{l}) \tag{3.16}$$

where C and K are the heat capacities and thermal conductivities of the electrons (C_e,K_e) and the lattice (C_l,K_l). κ is the electron–phonon coupling constant and $S(\mathbf{x}, t)$ is the laser source term, already given in Eq. (3.12). The advantages of two methods — MD and TTM — are combined by substituting Eq. (3.16) from the TTM completely by molecular dynamics [114, 42, 53, 125]. The heat diffusion equation for the electrons, Eq. (3.15), is solved by a finite difference (FD) method.

The heat equation is a partial differential equation. For its solution a *forward in time central in space* (FTCS) method is used [103]. This first–order method is explicit in time. For equations of the form

$$\frac{\partial u(x,t)}{\partial t} = \beta \frac{\partial^2 u(x,t)}{\partial x^2} \tag{3.17}$$

the FCTS scheme is conditionally stable if the following VON NEUMANN condition is satisfied:

$$\frac{2\beta \Delta t}{(\Delta x)^2} \leq 1. \tag{3.18}$$

Δt and Δx are the time step and the size of the finite differences, respectively. For the problem given in Eq. (3.15) the upper bound for the time step is $\Delta t \approx 10^{-18}$ s when estimating it for typical metals. Due to the explicit[1] nature of the FCTS scheme, the solution is computationally inexpensive. This is important, because of the small time step Δt, the heat conduction equation has to be solved many times for one time step δt in the molecular dynamics (typically 10^{-15} s).

The used hybrid scheme works in three–dimensions, but to show its function a two–dimensional version is shown in Fig. 3.2. For the molecular dynamics part a geometric algorithm based on the linked–cell method is used [2]. A cubical simulation box is subdivided into MD cells. The atoms are assigned to the cells according to their position in the sample. The size of one MD cell is chosen such, that only particles in adjacent cells can interact with each other. Usually this is in the order of the used potentials range, the cutoff radius R_{cut}. At this point the simulation contains $m_1 \times m_2 \times m_3$ MD cells. For reasons discussed later, aluminum was used as a model system throughout this work. The cutoff radius of the used potentials is $R_{\text{cut}} \approx 5.6$ Å and its inverse density is 16.6 Å^3/atom. From

[1] For the computation of the discretized $u(x,t)$–field, no system of algebraic equations has to be solved.

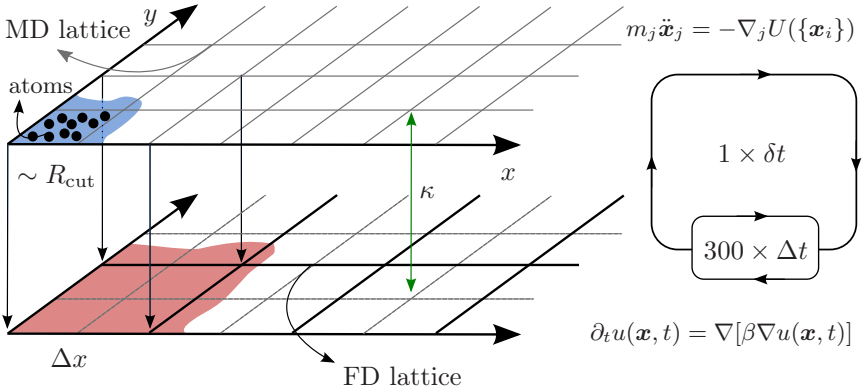

Figure 3.2: Schematic representation of the hybrid simulation. The electron temperature is described by Eq. (3.15), which is solved on the coarse lattice. For the motion of the atoms the MD method is used. The lattices are coupled via an electron–phonon coupling term κ. Time step δt used for MD has to be a multiple of the FD time step Δt.

these values, roughly 11 atoms per MD cell can be found. This number is too small to calculate a reasonable lattice temperature per cell. Therefore several MD cells are grouped commensurably into larger finite difference (FD) cells. The MD lattice is coarse grained into $f_1 \times f_2 \times f_3$ FD cells, so that at least 500 atoms are inside each of them. The lattice temperature T_{l}^i of the i–th cell can be calculated by averaging the kinetic energy of the atoms inside:

$$\langle E_{\mathrm{kin}} \rangle^i = \frac{3}{2} k_{\mathrm{B}} T_{\mathrm{l}}^i. \tag{3.19}$$

To each of the $f_1 \times f_2 \times f_3$ FD cells an electronic (T_{e}^i) and a lattice (T_{l}^i) temperature is associated. The lattice temperature is used in the heat conduction equation, Eq. (3.15), and also in the coupling term ξ^i in the MD equations[2]. For the MD part, which completely substitutes Eq. (3.16), the `IMD` code with an altered equation of motion is used [121]. Both temperatures enter the coupling term, which is responsible for energy exchange

[2]The coupling term ξ^i is not global, in contrast it has to be defined for each of the $f_1 \times f_2 \times f_3$ FD cells during the simulation.

between the electrons and the lattice. The index i corresponds to the FD cell to which the j–th atom belongs:

$$m_j \ddot{\boldsymbol{x}}_j = -\nabla_{\boldsymbol{x}_j} U(\boldsymbol{x}_1, \boldsymbol{x}_2, \ldots, \boldsymbol{x}_N) + \xi^i m_j \boldsymbol{v}_j^{\mathrm{t}}, \tag{3.20}$$

$$\text{with} \quad \xi^i = \frac{\sum_{\alpha=1}^{n} \kappa V_{\mathrm{cell}} (T_{\mathrm{e}}^{\alpha,i} - T_{\mathrm{l}}^i)}{n \sum_k m_k (\boldsymbol{v}_k^{\mathrm{t}})^2}. \tag{3.21}$$

In Eq. (3.21) m_k and $\boldsymbol{v}_k^{\mathrm{t}}$ are the mass and the velocity of the k–th atom. The forces are given in the common form by the negative gradient of the potential. For the particle velocities thermal values are used, i.e. $\boldsymbol{v}_k^{\mathrm{t}} = \boldsymbol{v}_k - \boldsymbol{v}^{\mathrm{c}}$, where $\boldsymbol{v}^{\mathrm{c}}$ is the center of mass velocity of the FD cell to which the k–th atom belongs. The temperature $T_{\mathrm{e,l}}^i$ and the coupling term ξ^i are defined for each FD cell with volume V_{cell}. Thus, $T_{\mathrm{e,l}}^i$ are functions of $\boldsymbol{x}$ and t. The summation over k in Eq. (3.21) is performed over all atoms in a given cell. While for each MD time step δt the diffusion equation has to be solved numerous times ($n = \delta t / \Delta t$), an average value of ξ^i after n iterations is passed to the MD equations, explaining the summation over α in Eq. (3.21). For a better readability, the cell index i, and the space and time coordinates $(\boldsymbol{x}, t)$ for the temperature fields $T_{\mathrm{e,l}}^i$ are omitted from now on: $T_{\mathrm{e,l}}^i(t) = T_{\mathrm{e,l}}(\boldsymbol{x}, t) = T_{\mathrm{e,l}}$.

In general, the FD lattice is three–dimensional, resulting in a three–dimensional heat conduction. In short laser irradiation the laser spot size is typically much larger than the depth affected by laser heating (order of nm's compared to μm's). In this special case a one–dimensional diffusion equation for the electrons can be used [15]. Eq. (3.15) becomes

$$C_{\mathrm{e}}(T_{\mathrm{e}}) \frac{\partial T_{\mathrm{e}}}{\partial t} = \frac{\partial}{\partial x} \left[K_{\mathrm{e}}(T_{\mathrm{e}}) \frac{\partial}{\partial x} T_{\mathrm{e}} \right] - \kappa (T_{\mathrm{e}} - T_{\mathrm{l}}) + S(x, t). \tag{3.22}$$

This will be used later on for the application of the hybrid model to homogenous laser pulses in metals, see Sec. 4.2.

Assumptions for the temperature behavior of C_{e} and K_{e} have to be made as further simplifications. The electrons heat capacity can be calculated by taking the derivative of the total electron energy density with respect

to the electron temperature [11]:

$$C_{\mathrm{e}}(T_{\mathrm{e}}) = \int_0^\infty \epsilon \frac{\partial f(\epsilon, \mu, T_{\mathrm{e}})}{\partial T_{\mathrm{e}}} g(\epsilon) \mathrm{d}\epsilon, \tag{3.23}$$

where $g(\epsilon)$ is the electron density of state at the energy level ϵ, μ is the chemical potential at T_{e} and $f(\epsilon, \mu, T_{\mathrm{e}})$ is the FERMI distribution function. For low temperatures the SOMMERFELD expansion of the electronic free energy is used. The result was already derived in Sec. 2.1.2, where the heat capacity for the free electron gas was given with $C_{\mathrm{e}} = \gamma T_{\mathrm{e}}$, γ being the electron heat capacity constant. Especially for aluminum this approximation is valid even for temperatures above 20,000 K [79]. The coefficient of the electron heat conductivity K_{e} is more difficult to model, since it depends on the local electronic and atomic temperature. Low temperature approximations for K_{e} exist, but in laser ablation the temperatures can rise as high as the FERMI temperature of the metal [132, 9]. However, using a formula valid for low temperatures at higher values, or assuming K_{e} as constant will both result in an error. Throughout this work a constant value for K_{e} was favored. In addition, a fixed value for K_{e} simplifies the diffusion equation such that the FTCS scheme solves

$$\gamma T_{\mathrm{e}} \frac{\partial T_{\mathrm{e}}}{\partial t} = K_{\mathrm{e}} \frac{\partial^2}{\partial x^2} T_{\mathrm{e}} - \kappa (T_{\mathrm{e}} - T_{\mathrm{l}}) + S(x, t). \tag{3.24}$$

When further on referred to the Two–Temperature Model (TTM) or the hybrid model, the solution of the two equations (3.24), or its three–dimensional counterpart Eq. (3.15) and Eq. (3.20) is meant.

Chapter 4

Calculations and Results

The theoretical background was given in chapter 2. Then, in chapter 3, the computational model and the implementation was discussed in detail. Now, for a laser ablation simulation a system has to be chosen. Due to the nature of the Two–Temperature Model (TTM), this choice is restricted to metals or metallic alloys.

For the simulations of a material with isotropic heat conduction aluminum was chosen, while for an anisotropic material $Al_{13}Co_4$ was used. The choice of aluminum was not at all arbitrary, it has some advantages in the computational description compared to other metals. The applied effective potentials do not have to describe phase transitions in the solid state like the bcc–fcc transition in iron. Additionally, the small electron temperature relaxation time of 67 fs makes it an ideal candidate for the TTM. The more complex eTTM, that was introduced in Sec. 2.3.1, is not required. As a third argument, potentials already exist in the literature. Especially the last argument is of great importance, because for ablation simulations the results are only as good as the potentials used.

For metals, EAM potentials have been established. During ablation, free surfaces, clusters, vacancies or stacking faults occur, which have already successfully been modeled by EAM potentials [33]. From the various EAM potentials that exist in the literature, the focus will be limited to two of them: The potential from Ercolessi and Adams [38] and the one developed by Mishin and Farkas [90]. As a test for their capability, the $P - \rho$ phase diagram was calculated via molecular dynamics simulations. A correct description of the three phases is the minimal pre–condition for a potential. The transitions solid–liquid and liquid–gas do not have to match experimental data in detail, but the change of phase should be distinct. This is important for the analysis of the gas phase in Sec. 4.4 and to make rough predictions about the compositions of the ablated material.

After the validation of the potentials, ablation experiments for aluminum

follow. The simple case of homogenously heated aluminum with electronic heat conduction is considered. In the next section, the simulations are expanded to more general laser intensities. Simulations with inhomogeneous beam profiles are of special interest because todays techniques allow foci smaller than the wavelength [111]. It is possible to achieve these length scales with todays' MD simulations. From the data, the ablation threshold, velocity, angular or cluster size distributions can be determined and compared to experiments. In the end a more complex system, the metallic alloy $Al_{13}Co_4$, which is related to the decagonal phase of Al–Ni–Co (a system with anisotropic heat conduction) is studied.

4.1 Pre–Survey: The Phase Diagram of Aluminum

Although the potentials were fitted to properties like the surface energy or the melting point, their application is limited to moderate temperatures and bulk samples in most cases.

The processes during laser ablation were described quantitatively in Sec. 2.2. It was shown, that for a thorough description at least the solid, liquid and the gas phase are necessary. Even more: Under specific circumstances plasma can arise above the surface [54]. However, plasma cannot be treated within the used models and was therefore neglected for all simulations. A two–fold justification can be given. First, the laser pulses are in the order of 500 fs and shorter. At these short times, an eventually expanding plasma has dimensions of nm's only [54]. Second, only single laser pulse excitations were investigated. An existing plasma would interact with the radiation followed from a second pulse.

The Solid-Liquid Transition

For the $P - \rho$ phase diagram, the solid–liquid and the liquid–gas coexistence line have to be determined by MD simulations. For all simulations, the same sample containing 32,000 atoms was used. The aluminum block, with an edge length of 8.1 nm, was initially equilibrated to 301 K. With a lattice constant of $a_0 = 0.4032$ nm the pressure on the sample is approximately 0 GPa. During the heating simulation of the solid the density was monitored. At the actual solid–liquid phase transition a jump can be

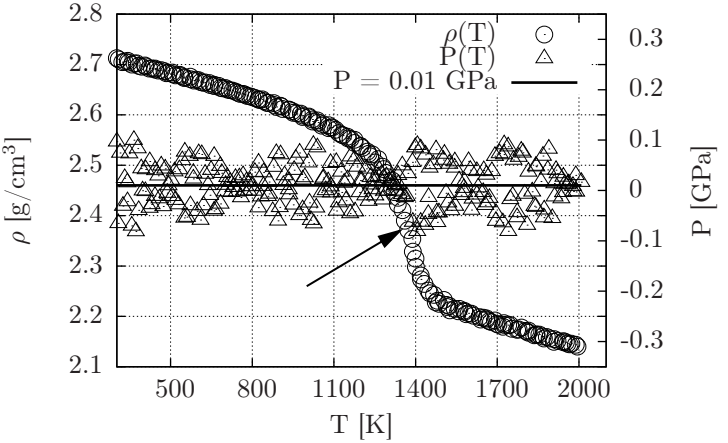

Figure 4.1: The solid–liquid transition as a result of the MD simulations. The circles and triangles correspond to the values of ρ and P during the heating simulation. The arrow marks the actual melting temperature.

observed (see Fig. 4.1). From the same figure, the values for $(\rho_{\mathrm{melt}}, P_{\mathrm{melt}})$ can be obtained and collected in the $P - \rho$ diagram. For each point of the solid–liquid phase transition line a two–step MD simulation was carried out.

1. The pressure was increased at constant temperature to the desired value P. During the run isotropic[1] volume scaling was allowed.

2. T was increased via a Nosé–Hoover thermostat at constant pressure over the melting point.

The rate of heating was constant for 50,000 steps with 1.018 fs each from 301 K to 1,500 K. The simulations correspond to path No. 2 in Fig. 4.2.

The melting temperature with $T_{\mathrm{melt}}^{\mathrm{sim}} = (1280 \pm 50)$ K for the Ercolessi potential turns out to be too high compared to the literature value of $T_{\mathrm{melt}}^{\mathrm{lit}} = 934$ K. One reason for the overheating is the non–physical heating

[1] The simulation box is scaled isotropic in all three directions while for an axial scaling – also possible with `IMD` – two directions are fixed.

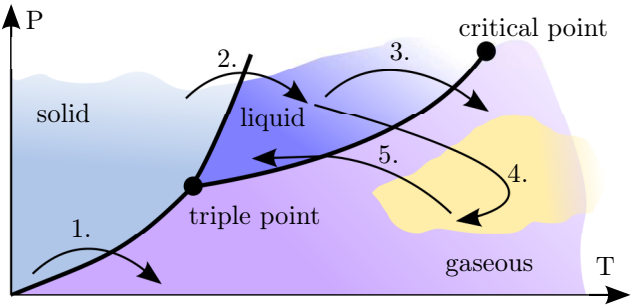

Figure 4.2: Sketch of the T–P phase diagram for a material without anomaly. The arrows and numbers indicate the paths that were simulated to determine the coexistence lines.

rate of 10^{12} K/s. Besides that, the perfect crystal without seeds for melting and the periodic boundary conditions lead to a delayed melting. Without free surfaces, nucleation is hindered for the melting process [44, 63]. With a more realistic sample, including vacancies and a free surface, the melting temperature can be reduced by several K's, however the effect is small. A better way to determine the melting temperature is done by a two–phase simulation. Here, a liquid and a solid phase are brought into contact. The simulation is carried out at different temperatures and the boundary between solid and liquid is tracked. At temperatures below T_{melt} the liquid part solidifies, while for higher temperatures the solid part melts. However, this procedure is too complex for a whole phase diagram where between 100 and 200 individual simulations are needed.

The Liquid-Gas Transition

The points in the liquid–vapor coexistence region were more difficult to obtain, because the transition cannot be seen by a further increase of temperature, which would correspond to path No. 3 in Fig. 4.2. As a remedy, the fact was used that the gaseous phase has the same symmetry as the liquid state. The coordinates of a liquid sample were scaled by a factor of 1.5, leading to a gaseous state (step No. 4 in Fig. 4.2). T and P are not known for this artificially created gas state, thus the sample had to be equilibrated again to determine its temperature and pressure. For each

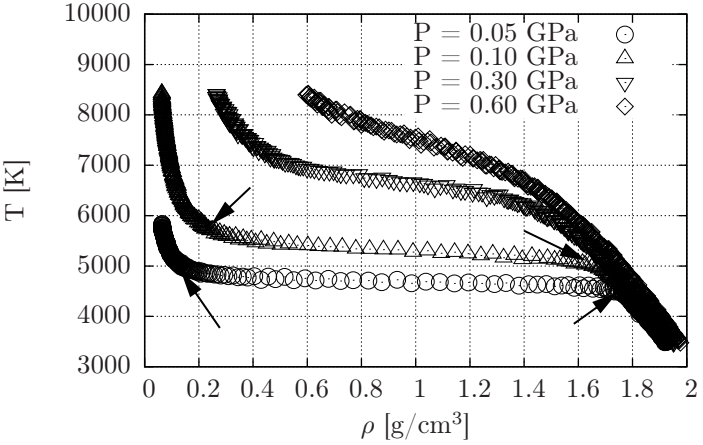

Figure 4.3: Four different isobaric curves for the condensation. The arrows mark the estimated values for the liquid vapor coexistence line in the P–ρ diagram.

point $(P_{\text{vap}}, T_{\text{vap}})$ of the gas–liquid coexistence line a two–step simulation was done.

1. The pressure was adjusted to the desired value P.

2. A cooling simulation at constant pressure follows, step No. 5 in Fig. 4.2.

In Fig. 4.3 different isobaric simulations are shown. According to the arrows, the points in the $P - \rho$ diagram (see Fig. 4.4) were estimated.

Comparison to Experiments

Although the above method seems to be rather simple, the phase diagram shows all the relevant features. Three phases can be clearly seen in the $P - \rho$ phase diagram, Fig. 4.4. The potential given by Mishin *et al.* leads roughly to the same behavior for melting, but fails to produce vaporization in the coexistence region when the pressure approaches the critical point. These regions are of interest especially for dynamics in the evolving plume.

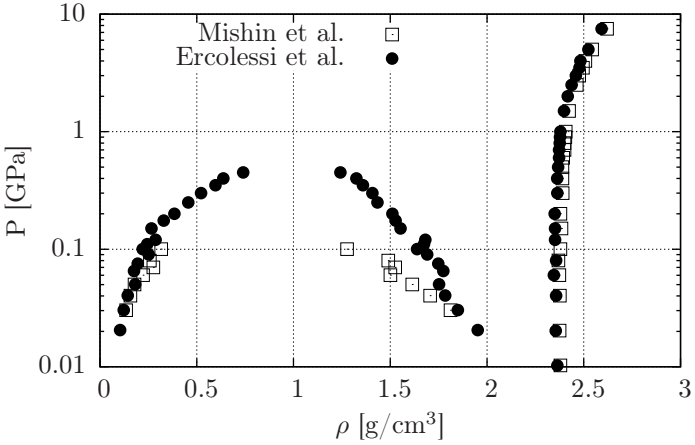

Figure 4.4: The calculated phase diagram for aluminum. The potentials developed by Ercolessi *et al.* better describe the system in the the coexistence regime.

Therefore all further simulations were done with the potentials developed by Ercolessi and Adams.

Literature values for the critical density are $\rho_c = 0.28 - 0.79$ g/cm^3 and $P_c = 0.19 - 0.55$ GPa for the critical pressure (see [41] for an overview). The above calculations lead to values of $\rho_c \approx 0.7 - 0.9$ g/cm^3 and $P_c \approx 0.45$ GPa which is quite comparable. In the small pressure region the results are in good agreement with experimental values, e.g. at $P = 0.1$ GPa the density is $\rho = 2.35$ g/cm^3 ($\rho_{\text{exp}} \approx 2.4$ g/cm^3). For higher pressures, the calculated values deviate more. The highest experimental accessible data for melting is at $P_{\text{exp}} \approx 1.2$ GPa, while in the simulation melting at pressures higher than $P = 5$ GPa is observed. Most ablation simulations are in extreme non–equilibrium, legitimating this crude way of calculating the phase diagram. The heating of the lattice occurs typically in times less than 10 ps, so it is already an important result that the potentials used can reproduce the phase transitions more than qualitatively.

Other Materials

By following the above recipe, phase diagrams for all kinds of materials can be at least estimated. The $P - \rho$ diagrams for iron, copper and Ni_3Al are shown in Fig. 4.5. Calculating the phase diagrams for these systems turned out to be more difficult than it was for aluminum. First, melting temperatures for the pure metals are — again — higher than the literature values: More than 800 K for iron and 400 K for copper. Second, the vapor–liquid coexistence lines near the critical point could not be calculated.

EAM potentials were used for copper [93]. These potentials were fitted to a database containing both ab initio and experimental data like phonon frequencies $\nu_{\mathrm{L}}(X)$ and $\nu_{\mathrm{T}}(X)$, elastic constants c_{ij} or thermal expansion factors for fcc copper at several temperatures.

In the case of iron a more complex potential type, including angular–dependent interactions was used. To distinguish them from MEAM [12] or EDM [100] potentials, they are denoted the *Angular-Dependent Potentials* (ADP) [92, 91]. The fitting database included experimental values of the lattice constant, three elastic constants c_{ij}, vacancy formation $E_{\mathrm{v}}^{\mathrm{f}}$ and migration $E_{\mathrm{v}}^{\mathrm{m}}$ energies and the surface energy γ_{s}. Interpreting these data, the potential was trained mainly for simulations of bulk properties instead of high temperature applications. This can be seen in the bad shape of the coexistence region, Fig. 4.5. Additionally it is difficult to model the hcp–fcc transition and the magnetic properties of iron. In other words, these potentials were not suitable for laser ablation simulations.

EAM potentials were used again for Ni_3Al [89]. In Fig. 4.5 the results are shown. More points towards the critical point can be resolved. Therefore, these potentials are suitable for further ablation simulations. Mishin *et al.* designed the potentials to describe lattice properties of Ni_3Al, point defects, planar faults as well as the γ and γ' field of the Ni–Al phase diagram. The fitting database contained experimental values of the lattice parameters, cohesive energies, elastic constants c_{ij}, vacation formation and migration energy. Thermal expansion factors at several temperatures were also included with a small weight. Additional ab initio data was added in the form of energy–volume relations for several structures like fcc, hcp, bcc, simple cubic (sc) and diamond.

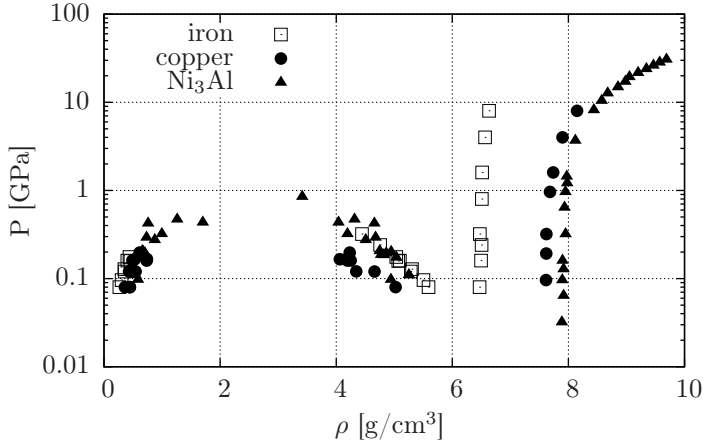

Figure 4.5: The phase diagrams for iron, copper and Ni_3Al.

4.2 Laser Ablation in Isotropic Materials: Metals

The phase diagram and simulation tools described in chapter 3 are all that is needed for an ablation simulation. It can be seen that the laser source term $S(\boldsymbol{x}, t)$ in the TTM equations from section 3.3, becomes one–dimensional in space for a spatially homogenous power density. Assuming that the x–axis is the laser incident direction, the power source density is given by

$$S(x,t) = (1-R)S_0\alpha e^{-\alpha x} e^{-\frac{(t-t_0)^2}{2\sigma_t^2}}, \tag{4.1}$$

The density relates to the innermost area of a GAUSSian laser beam. For these kind of beams, the radial temperature gradient can be neglected compared to the one in normal direction [15]. In this case, the heat conduction can be treated as one–dimensional. The equation in the Two–Temperature Model simplifies to

$$C_\mathrm{e}(T_\mathrm{e})\frac{\partial T_\mathrm{e}}{\partial t} = K_\mathrm{e}\frac{\partial^2 T_\mathrm{e}}{\partial x^2} - \kappa(T_\mathrm{e} - T_\mathrm{l}) + S(x,t). \tag{4.2}$$

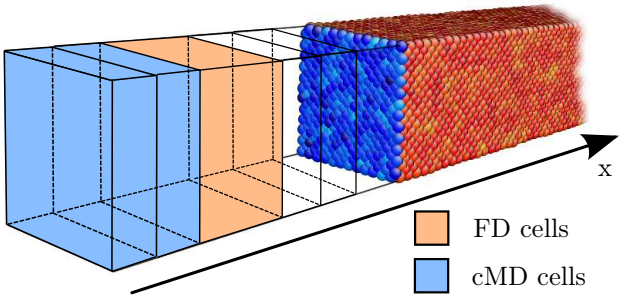

Figure 4.6: Scheme for the partitioning of the simulated volume into cells. There are two different kinds of cells: One for the FD lattice on which the electron temperature $T_e(x,t)$ is calculated, and a second mesh on which the average quantities for MD are calculated. The two meshes do not need to have the same size (figure was created using `AtomEye` [76]).

The method to solve this partial differential equation was explained in Sec. 3.3. There, the concept of molecular dynamics (MD) and finite difference (FD) cells was introduced. The latter ones are used to allocate an electronic temperature to a certain volume in space, the orange cells in Fig. 4.6. The decomposition of the volume in MD cells is a computational trick to speed up the algorithm. Now a third kind of cell is introduced, the coarse molecular dynamics (cMD) cell.

The calculations for the lattice dynamics stay — independent of the underlying electronic system — three–dimensional. All observables, except the temperature of the electrons, are based on the atomic data gathered from MD simulations by ensemble averages. The time evolution of an arbitrary observable would be a four–dimensional function, $f = f(\boldsymbol{r}, t)$. To avoid this, the volume is divided into slices along the x–axis, the direction of incident light. The physical quantities are calculated inside these coarse MD cells, the blue cells in Fig. 4.6. The two meshes are coupled to each other by the electron–phonon coupling κ in the TTM equations but do not have to match in size. In general, the FD cells are chosen such that they contain 500 or more atoms. This ensures reasonable statistics for the averages. By the reduction to a two–dimensional function, contour plots for time evolutions can be generated.

Three different laser intensity regions can be defined:

1. Small fluence: When the laser fluence is small compared to the ablation threshold F_{th}, the atoms near the surface are heated up slightly, no melting occurs.

2. Medium fluence: The applied laser intensity is comparable to the threshold value of ablation. Melting near the surface can be observed [129]. The phenomenon is called *laser induced surface melting*.

3. High fluence: When the fluence is at the ablation value or higher, material floats from the surface into the ambient gas.

The first case is trivial and will not be discussed. The second scenario is investigated in this section, where melting depths for various pulses and energies are given. In Sec. 4.4 pulses with higher energy are considered, there the important parameter of the ablation threshold F_{th} is determined.

4.2.1 Parameters for Aluminum

For the solutions of the TTM equations a small number of parameters have to be specified. For the electron–phonon coupling constant κ a value of $5.69{\cdot}10^{17}$ J/Km^{3}s was chosen [58]. The electronic heat conductivity was treated as a constant $K_{\mathrm{e}} = 235$ J/mKs, while the specific heat is temperature dependent: $C_{\mathrm{e}} = \gamma T_{\mathrm{e}}$. The coefficient γ was used with 134.5 J/m^{3}K^2 throughout this work [67]. For the optical penetration depth two different values were used for the different models. $\alpha^{-1} = 6.5$ nm for the TTM and 8 nm for the rescale model respectively. Fisher *et al.* give $R \approx 0.85$ as reflectivity for a beam with 800 nm wavelength [43], while a more recent work reports a value of $R \approx 0.8$ [66]. The average of these two experiments $R = 0.825$ was taken.

4.2.2 Laser Induced Surface Melting

For the simulations a box of size $172.1 \times 4.86 \times 4.86$ nm^3 with 230,400 aluminum atoms was used. This box was divided into 400 FD cells along the x–axis. On average 600 atoms are inside each of these cells. A Gaussian shaped pulse in time with durations σ_t between 100 and 1000 fs was applied. The fluences were varied between 571 and 1029 J/m^2. For the absorption

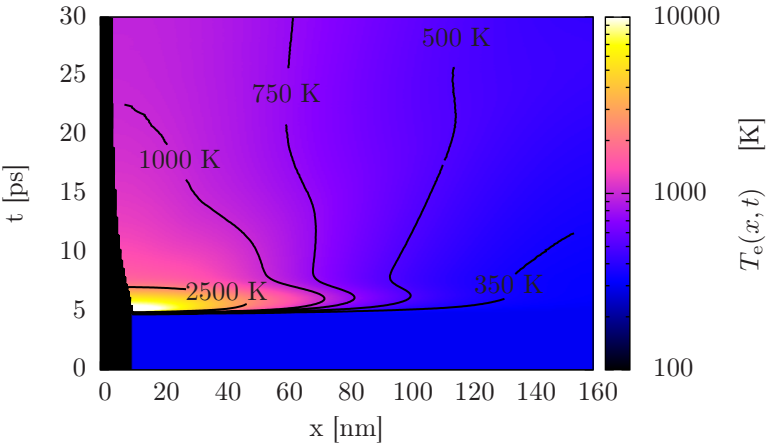

Figure 4.7: Time evolution of the electronic temperature $T_e(x,t)$ as it is calculated via the FD scheme. The laser hits the surface at $t = 5$ ps and lasts only 100 fs (less than one pixel in the graph). Iso–temperature lines are shown for 350 K, 500 K, 750 K, 1,000 K and 2,500 K. A very small volume is heated up to more than 10,000 K

length a value of $\alpha^{-1} = 6.5$ nm, which corresponds to a laser wavelength of $\lambda = 250$ nm was chosen [14]. The pulses had their intensity maximum 5 ps after the simulation started. Combined, 54 separate simulations were done, each of them representing one point in Fig. 4.12 on page 76. The figures on the next pages show typical contour plots for all relevant observables for a 100 fs laser pulse with fluence $F = 1029$ J/m^2.

The electrons, which interact first with the laser, immediately heat up to over 10,000 K — even for moderate intensities. A sharp rise in temperature can be seen in Fig. 4.7, where the time evolution of the electronic temperature is plotted. A cut along the x–axis shows, that 0.10 ps after the intensity maximum of the laser, the electron temperature mainly follows the pulse shape, Fig. 4.8. The exponential decay has its origin in the absorption behavior of the metal, the Lambert–Beer law that is proportional to $\exp(-\alpha x)$. At this time, the lattice temperature has risen only slightly above room temperature. With advancing time, a convergence of

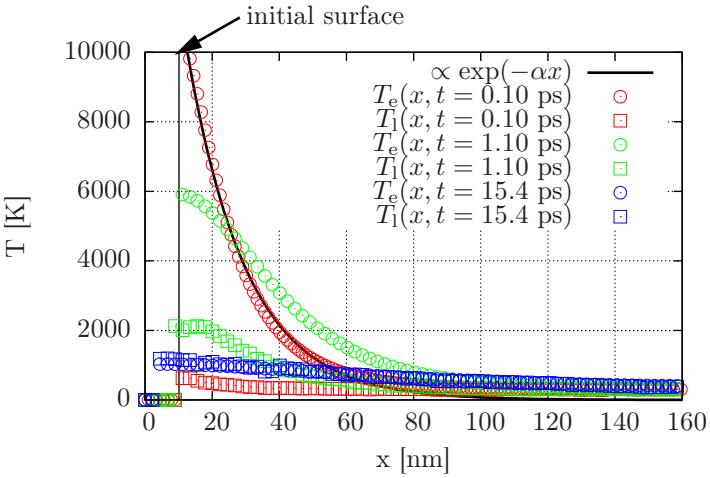

Figure 4.8: Electron and lattice temperatures are shown for three different times 0.10 ps, 1.10 ps and 15.4 ps after the intensity maximum hits the surface. $T_e(x, t)$ mainly follows the external laser field, which is an exponential in this case. Bit by bit the two temperatures converge to their equilibrium value, which is almost reached at 15.4 ps.

the lattice and electron temperature can be seen. Indicated by an arrow is the initial surface coordinate at $x = 10.1$ nm. Towards the end of the simulation ($t \gtrsim 15$ ps) temperatures are measured for $x < 10.1$ nm. This is a clear indication of the thermal expansion and melting of the aluminum block. Due to the electron–phonon coupling the temperatures of the lattice and the electrons converge. An estimation of the electron–cooling time τ_{el} can be made by comparing the heat capacity of the electrons C_e to the value of the coupling constant κ [3]:

$$\tau_{\text{el}} = \frac{C_e}{\kappa}. \tag{4.3}$$

In general C_e is a non–analytic function of temperature T_e, making it difficult to give accurate values for τ_{el}. While tabulated functions for C_e exist [78, 79], the TTM model uses a linear scaling with temperature for C_e. An

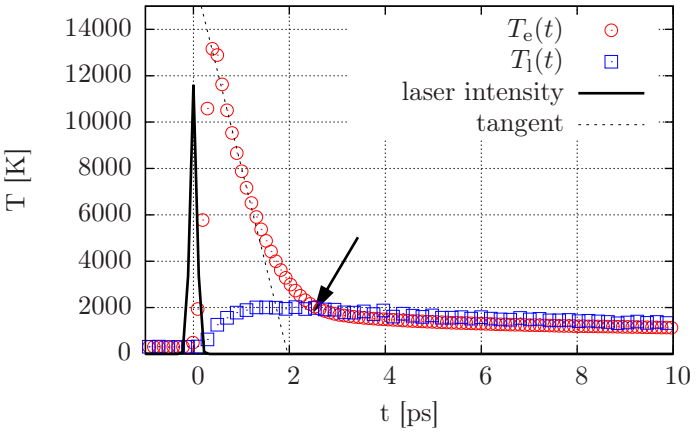

Figure 4.9: Electron lattice relaxation. The arrow indicates τ_{el}. A second method given by RETHFELD determines τ_{el} by the intersection of the tangent of T_e with the t–axis [106]. (The laser intensity is shown to clarify the different timescales.)

approximation for τ_{el} can be given via

$$\tau_{el} = \frac{C_e(T_{max}) + C_e(T_{min})}{2\kappa}. \tag{4.4}$$

For aluminum this results in $\tau_{el} \approx 1.58$ ps. Due to the temperature dependence of C_e, τ_{el} also depends on the temperature. However, two estimations from the simulations of an 100 fs pulse are given within Fig. 4.9, which shows a cut along the t–axis of the contour plot. The time where $T_e = T_l$ is indicated by the arrow. This is at $t = \tau_{el} = 2.53$ ps after the pulse. RETHFELD approximates the relaxation time by the intersection of the tangent of $T_e(t)$ with the t–axis [106]. This method leads to $\tau_{el} = 2$ ps. HÜTTNER reports a relaxation time for aluminum with $\tau_{el}^{exp} = 4.27$ ps [58], a value which is quite comparable with the predictions derived from the TTM.

The contour plot for the lattice temperature is shown in Fig. 4.10. The heating process is much slower compared to the electrons, also the temperatures are considerably lower. The highest value is achieved near the surface and is 1,700 K.

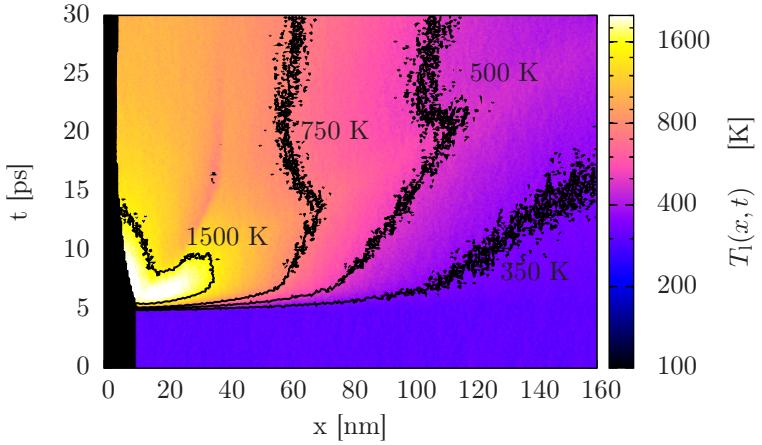

Figure 4.10: Time evolution of the lattice temperature $T_l(x,t)$ as it is calculated during the MD simulations. Iso–temperature lines for 350 K, 500 K, 750 K and 1,500 K are shown. The hottest area where the melting occurs is near the surface with $\approx$ 1,700 K.

The next quantity discussed is the mass density ρ shown in Fig. 4.11. In the plot, density oscillations can be noticed even at times where no laser field is present ($t < 5$ ps). The appearance of the oscillations can be explained by the overlapping of two grids, the so–called Moiré–pattern. These interference patterns are created when two grids were overlaid at an angle, or when — as in this case — the grids have slightly different mesh sizes. One grid is the intrinsic lattice constant of the fcc crystal ($d_1 = a_0/2 = 2.016$ Å), the other is from the above described cell–based method for the ensemble averages. The length of one MD cell is $d_2 = 1.81$ Å. For the Moiré–patterns the spacing can be calculated by

$$d_3 = \frac{d_1 \cdot d_2}{|d_1 - d_2|} = 17.9 \text{ Å}. \tag{4.5}$$

This value matches the distance of the lines in Fig. 4.11. The oscillations have no physical meaning, they are rather an effect of the numerical methods applied. Near the surface, where the crystal is already molten, no perfect lattice exists. In conclusion, the patterns vanish.

For the melting depth the distance from the actual surface coordinate to the point where the Moiré–pattern starts can be used. A sharp solid–liquid interface can be seen, making the determination of the melting front straightforward. Alternatively, a sudden drop in density from $\rho_{\text{solid}} = 2.7$ g/cm^3 to $\rho_{\text{liquid}} = 2.0$ g/cm^3 where the melting front proceeds can be seen. Results for different pulse lengths and energies are shown in Fig. 4.12. The melting depth scales linearly with $\log(F)$. On the other hand, the melting depth remains stationary when the pulse length σ_t is varied. This is because the normalization of S_0 in Eq. (4.1) is chosen such, that $\int S \mathrm{d}V = E_{\text{pulse}}$, with E_{pulse} the total pulse energy. Thus, a longer pulse leads to a smaller power density $S(\boldsymbol{x}, t)$. In conclusion, the melting depth is a function of absolute absorbed energy only. In experiments the melting behavior is of minor interest, making it difficult to compare the calculated results. Williamson *et al.* report 20 ps as sufficient melting time for 25 nm thick aluminum films [136]. The time depends on the actual laser conditions, but it can be seen in Fig. 4.11 that after 19 ps the melting depth in the simulation is around 27 nm, which compares well with the experiment.

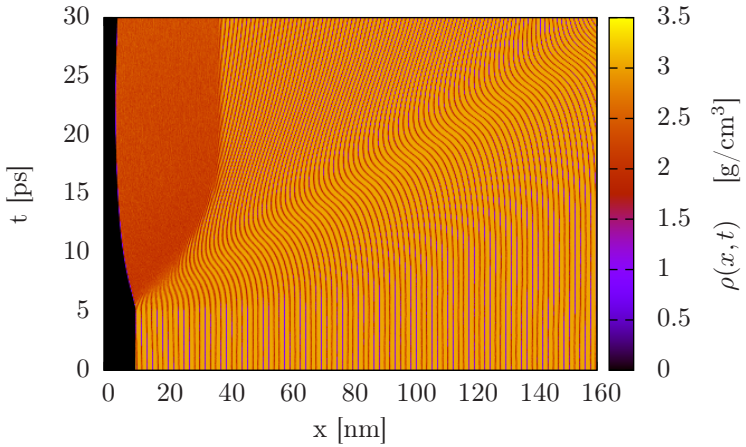

Figure 4.11: Time evolution of the density. The solid–liquid interface can be clearly seen. The fluence is too small for ablation, after 20 ps the melting front stays stationary. See Fig. 4.13 in contrast for a fluence above the ablation threshold F_{th}. An explanation for the stripe pattern is given in the text.

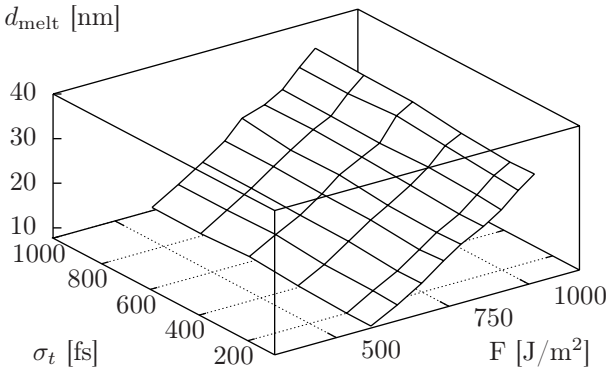

Figure 4.12: Melting depth for aluminum for different laser pulses.

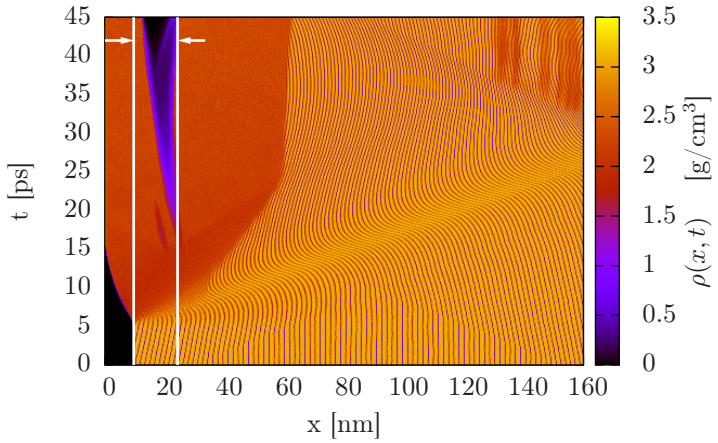

Figure 4.13: Contour plot of the mass density. The fluence applied to the target is above the threshold value F_{th}. The arrows indicate the ablation depth d_{abl}.

4.2.3 The Ablation Threshold

In the last section moderate fluences were discussed. The laser was strong enough to melt the surface, but was too weak to remove material. When the fluence is further increased, the ablation threshold F_{th} is reached and material starts to *ablate* from the target. From now on, only pulse durations with $\sigma_t = 100$ fs are used. In Fig. 4.13 a density contour plot is shown for a fluence $F = 1487\ \mathrm{J/m^2}$. It can be seen, that this value is above the threshold for ablation. From around 15 ps on, a layer of liquid aluminum starts to detach from the surface. This ablated layer forms a moving shell with constant velocity [59]. The layer and the bulk material build a pair of optically flat, sharp interfaces. Interference happens due to the sudden drop of optical density over a distance in the order of the wavelength. Pump and probe experiments with a 120 fs pulse at 620 nm wavelength were done showing these patterns, called NEWTONian rings [119]. Although the pulse duration is comparable ($\sigma_t = 100$ fs), the wavelength is smaller with $\lambda = 250$ nm. However, the same phenomena can be reproduced by the simulation.

The ablation threshold can be calculated following a method from experimental ablation studies. Preuss *et al.* derived a formula for the ablation depth, bringing the applied fluence F and the inverse thermal penetration depth α in relation to the ablation depth d_{abl} [104]:

$$d_{\mathrm{abl}} = \frac{1}{\alpha} \ln\left(\frac{F}{F_{\mathrm{th}}}\right). \tag{4.6}$$

The equation is valid only if the following assumptions are made:

1. Absorption can be described by the Lambert–Beer law and the reflectivity is constant during the pulse.
2. Ablation takes place after the pulse is over and no redeposition occurs.
3. The heat conduction is negligible.

While for ns–pulses not all of the above statements can be satisfied, they can for sub–picosecond pulses. Although heat conduction occurs, the thermal diffusion length $l_{\mathrm{th}} \propto \sqrt{K_{\mathrm{e}} t}$ is much smaller than for ns–pulses, where l_{th} is two orders of magnitude larger than the optical penetration depth. d_{abl} is shown in Fig. 4.14. From a linear fit the values obtained are $F_{\mathrm{th}} = (858 \pm 170)$ J/m^2 and $\alpha^{-1} = (27 \pm 6)$ nm. As done in experiments, both constants, α^{-1} and F_{th}, serve as fitting parameters [73, 104]. It should be noted that the points can not be fitted very well with the above equation, therefore the errors are quite large.

Vorobyev *et al.* determine 580 J/m^2 as ablation threshold in vacuum [130], while in [52] a fluence of 340 J/m^2 as *damage threshold* for aluminum is reported. In contrast Le Harzic *et al.* gave $F_{\mathrm{th}} = 1200$ J/m^2 [73] as ablation threshold. In the same work α^{-1} is found to be 39 nm for aluminum. However, different fluence regimes were studied in the experiments using 120 fs pulses, and only a few points for the low fluence regime ($F < 2000$ J/m^2) were taken into account for the fitting procedure. An error range was not given, so the values gained from simulations and experiments might still overlap. In other numerical studies, an ablation threshold of 700 J/m^2 is found [6], but (i) a slightly different model (no TTM) and (ii) different potentials were used, which makes a direct comparison difficult.

The last observable gained from the simulations is the pressure inside the bulk material. A contour plot is shown in Fig. 4.15. During the laser pulse the metal is heated iso–choric. This change of state leads to an

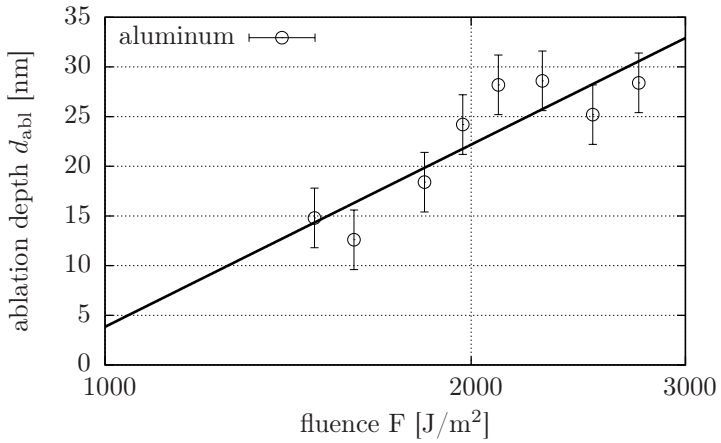

Figure 4.14: Ablation depth for the homogeneous 100 fs pulse in aluminum.

immediate increase of pressure, generating a pressure wave. Its speed can be estimated directly from the slope of the pressure maximum in the $x-t$–diagram. For the given parameters the speed is $v_{\mathrm{s}} \approx 6522$ m/s . Compared to the longitudinal speed of sound in aluminum ($v_{\mathrm{s}} = 6420$ m/s [77]), this wave is an ordinary sound wave and not a *shock wave*. The fluence values to induce shock waves have to be considerably higher than the intensities applied here [40]. Interesting for laser induced waves is an effect called *back–spallation* [30]. Back–spallation occurs when the pressure wave is reflected at the back of a thin film, thus reversing it to a tensile wave. The tensile pressure then exceeds the critical value of the bulk modulus. What follows is material failure, similar to laser ablation.

Being able to reproduce a number of physically relevance with the simulations is already a great result, but one problem arises when longer simulation times are of interest. The samples finite size effects the physics in the surface region. The pressure wave is reflected at the back side of the sample, thus traveling back to the surface.

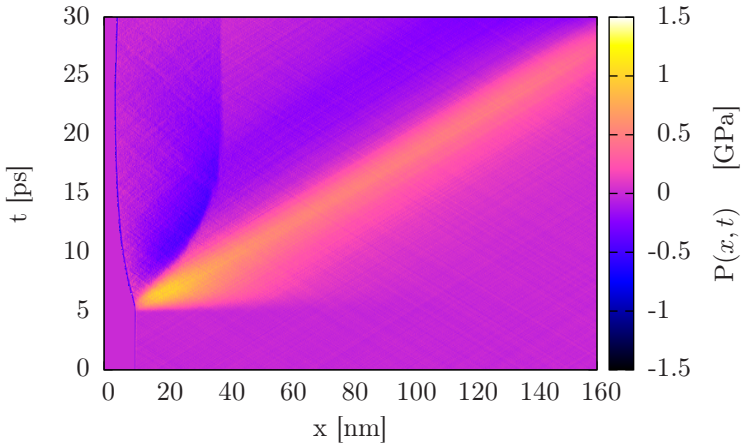

Figure 4.15: Time evolution of the pressure inside the sample. A pressure wave forming near the laser affected zone that travels into the bulk is observed.

4.3 Non–reflecting Boundary Conditions

Laser heated solids were studied in detail in the last section. It was shown, that due to the iso–choric heating, large stresses arise in the laser affected zone. The stress reloads itself into the bulk material, generating a pressure wave. In *infinite* samples, or for systems in a laboratory with dimensions of mm or cm, these stresses have long enough time to vanish in the bulk. For finite samples the time a wave needs to reach the end of the box is very short. In the existing case this leads to a reflection of the wave at the back side. The generated tensile pressure can fall below the YOUNGs modulus, rupture of the material is the result. Back–spallation is also observed in experiments or simulations [30, 140]. It totally depends on the processes of interest, if this wave is an artefact of the simulation or a physical effect. For studies on the ablation rate or the ablation threshold F_{th} the wave is an unwanted side effect.

A method to damp the emitted waves can be adopted from fracture simulations [51]. In simulations of fracture, pressure waves are emitted by the tip of the crack. There, a *stadium damping* is used to damp the waves.

For ablation, a slightly different method is applied. An additional damping force is added to the equations of motion in a certain sub–volume $\mathcal{V}$ of the simulation box:

$$m_j \ddot{\boldsymbol{x}}_j = \boldsymbol{F}_j - \zeta_0 f(\boldsymbol{x}_j) \cdot \boldsymbol{v}_j m_j. \tag{4.7}$$

$\boldsymbol{F}_j$ is the net force on the j–th particle due to the interactions with the other atoms and the energy transfer from or to the FD lattice. A linear increasing friction force is applied to the particles inside $\mathcal{V}$. This is done by the function $f(\boldsymbol{x}_j)$ in Eq. (4.7). The rate of damping depends on the particles x–coordinate. While particles in the very beginning of the zone only notice a small friction, particles towards the end were affected by a force up to $\zeta_0 \boldsymbol{v}_j m_j$. The special boundary conditions act like a damping ramp at the end of the simulation box. On the left side of Fig. 4.16 the laser induced pressure wave is shown. The arrow marks the spot where the wave is reflected, thus changing its sign. In case where the damping ramp is active, the reflected wave is much smaller. Compared to thermal fluctuations the reflected energy can be neglected.

Summary

For a basic understanding of laser heated solids, an isotropic medium irradiated with homogenous intensities, was studied. The metal chosen was aluminum which has a simple phase diagram and isotropic material properties. With realistic interatomic potentials and considerably large simulations, results can be directly compared to experiments. The laser intensity was distributed homogeneously on the surface, which resulted in a one–dimensional treatment for the electrons. However, the model is already useful to gain insight into the physics of laser heated solids. Basic phenomena that are observed in experiments like surface melting, ablation, interference patterns and pressure waves can be reproduced. In the next section a step towards more complex simulations, by using an inhomogeneous intensity profile, is taken.

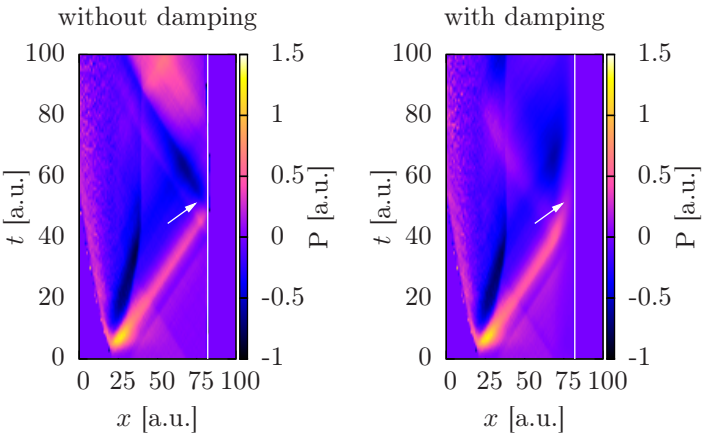

Figure 4.16: Non–reflecting boundary conditions. On the left side the original simulation is shown. The pressure wave is reflected at the back side (the white line) of the sample, indicated by the arrow. On the right hand side this reflection is prevented by an additional friction term in the equations of motion.

4.4 Inhomogeneous Ablation Experiments on Metals

Up to now, the applied laser fluence was distributed homogeneously on the target surface. The experimental setup corresponding to these simulations is that of matter heated in the center of a GAUSSian laser beam. In this section, the effects of femtosecond laser pulses with inhomogeneous profiles on aluminum will be investigated. As a consequence, a plume is evolving into the vacuum, where all kinds of distributions can be evaluated. Besides the ablated particles, a crater is formed in the bulk material.

For practical and computational reasons the system size was limited to $6 \cdot 10^7$ atoms. The practical aspect is the manageable size of a complete snapshot, which contains the masses, velocities, the potential energy, the electron density and the coordinates of all atoms. A single snapshot already

uses six GB of disc space[2]. The tools used for data manipulation like `MegaMol` [50] were at the limit of handling samples that large. The second argument is the computational time that is needed for a single simulation. On the High Performance Computing Center Stuttgart (HLRS) with 512 CPUs in parallel, a series of five different pulses consumes over 500,000 hours of CPU time.

With 60,000,000 atoms and a rectangular shaped surface of $A = 101 \times 101$ nm^2, the sample thickness is 108 nm. This geometry is too small for a three–dimensional diffusion equation, as it was introduced in Sec. 2.3. Large temperature gradients on the surface lead to very short diffusion times. As result, a quick thermalization on the target's surface to a homogenous temperature profile occurs. Instead, the method described in Sec. 3.2, where the kinetic energy of the atoms is scaled accordingly, will be used. The general power density $S(\boldsymbol{x}, t)$ was given with

$$S(\boldsymbol{x}, t) = (1 - R) S_0 \alpha e^{-\alpha x} I(y, z) e^{-\frac{(t-t_0)^2}{2\sigma_t^2}}. \tag{4.8}$$

For the pulses applied, the spatial intensity $I(y, z)$ on the target surface is chosen to be Gaussian:

$$I(y, z) = e^{-\frac{(y^2+z^2)}{\omega^2}}. \tag{4.9}$$

The system is again aluminum, using the same potentials as in Sec. 4.2 for the homogenous fluences. Because the gas phase was of interest, simulation times of 255 ps real time were necessary. At this time, the plume has already expanded up to 1.5 μm above the surface. For reliable statistics, five different initial conditions (velocity distributions corresponding to 300 K) were used. The main reason is, that only 3–10% of the bulk volume evaporate into the gas phase per single pulse, making conclusions about clusters based on a single simulation difficult.

The pulse duration was set to $\sigma_t = 100$ fs, α^{-1} in Eq. (4.8) was chosen to be 8.0 nm [14]. A series of varying laser fluences between 1373 J/m^2 and 3204 J/m^2 was performed. The values seem to be rather high, but it has to be noted, that the fluences correspond to the peak intensity, which is only achieved in the very center of the profile. For all simulations the half beam width was set to $\omega = 15$ nm.

[2] In 2010 the average disc space of a computer is around 500 GB, so less than 100 snapshots could be stored. Typical memory is between four and eight GB, so only one snapshot at a time could be visualized.

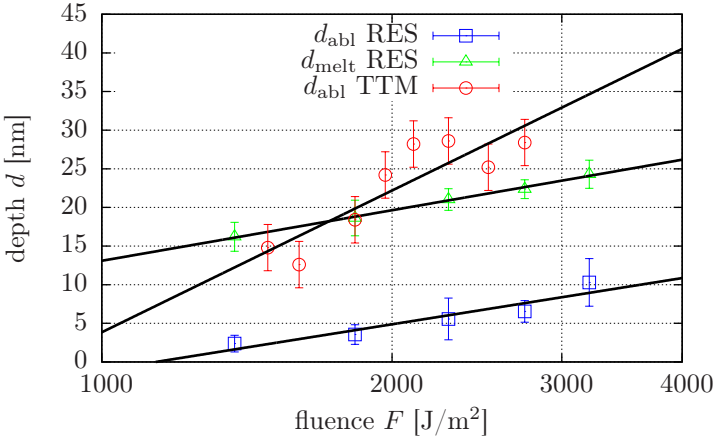

Figure 4.17: Melting and ablation depth for inhomogeneous pulses in the rescale model (RES). The penetration depth α^{-1} can be determined from the slope, while the axis intersection gives the ablation threshold F_{th}. For comparison the ablation depths from the TTM are shown.

4.4.1 The Ablation Threshold

The ablation threshold F_{th} can be determined following the same method as for the TTM simulations, Eq. (4.6). In a half–logarithmic plot, the ablation depth scales linear with applied fluence, see Fig. 4.17. In the same figure TTM results are shown for comparison. The threshold value gained from fitting is $F_{\mathrm{th}} = (1137 \pm 166)$ J/m^2 for the rescale model (RES), the penetration depth is $\alpha^{-1} = (8.6 \pm 1.7)$ nm. While F_{th}(RES) is comparable to the TTM model, α^{-1} is considerably smaller. The origin lies in the missing heat conduction of the electrons. For RES, no heat conduction is considered. The heat affected zone is smaller and in the order of the optical penetration depth α^{-1}, which is 8 nm for aluminum. However, the linear scaling is well pronounced and observed in experiments [73]. In experiments the slope of the ablation depth (*ablation rate*) strongly depends on the ambient gas, while the actual ablation threshold is not affected by the environment [104]. All simulations were done in vacuum, thus the environment for all simulations was exactly the same. In the

System	Quantity	Theory (this work)	Experiments
Al	F_{th} (TTM)	(858 ± 170) J/m^2	$580 \ldots 1200$ J/m^2
	F_{th} (RES)	(1137 ± 166) J/m^2	
	α^{-1} (TTM)	(27 ± 6) nm	39 nm
	α^{-1} (RES)	(8.6 ± 1.7) nm	
	t_{melt} (TTM)	19 ps for 27 nm	20 ps for 25 nm
	F_{melt} (TTM)	(469 ± 6) J/m^2	340 J/m^2

Table 4.1: Comparison of the ablation thresholds F_{th}, the penetration lengths α^{-1} and the melting time t_{melt} determined by the different models.

present case, different ablation rates reflect different models, one with and the other without fast heat conduction. See Tab. 4.1 for a comparison of the calculated parameters with experimental data.

4.4.2 Cluster Detection in the Plume

In the expanding gas plume, different sized clusters can develop. For the analysis of the cluster size distribution the `DBSCAN` (*Density Based Spatial Clustering of Applications with Noise*) algorithm was used [39]. Many advantages over other algorithms have set the choice to especially this one: (i) `DBSCAN` does not require the prior knowledge of the number of clusters in the volume, (ii) the shape of the clusters does not matter and (iii) it has a notion of noise. Noise in the case of atomic data corresponds to clusters with exactly one atom. All clusters with $N_{\mathrm{atoms}} = 1$ can be regarded as the gas phase of the ablated material. Two atoms are considered as a cluster, when their euclidian distance is below a certain value, $\epsilon = 0.35$ nm.

An average particle–cloud contains approximately 250,000 atoms for the lowest and 850,000 atoms for the highest fluence respectively. The algorithm was applied to the coordinates above the samples surface, i.e. the bulk material was removed. After the analysis, each atom is assigned with a new attribute C_N called `clusterID`. The assignment to a cluster is simple: If two atoms have the same C_N, they belong to the same cluster. Looking at the snapshot in Fig. 4.22, it can be seen that most of the clusters have spherical shape. This allows the determination of an average radius $R_N = \sqrt[3]{N_{\mathrm{atoms}}}$ for each cluster in units of the atomic radius. The largest

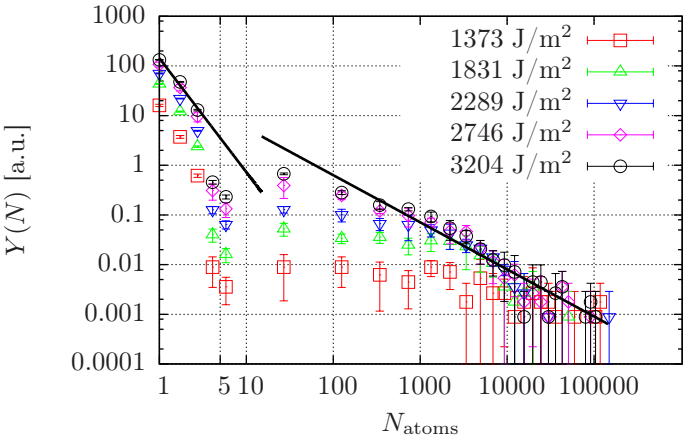

Figure 4.18: Cluster distribution for five different fluences between 1373 J/m^2 and 3204 J/m^2. For the ablation yield $Y(N)$ a power law $Y(N) \propto N^{-\delta}$ can be found with different δ values in the low–mass and the high–mass (N>10) ranges.

clusters in the plume contain approximately 100,000 atoms, corresponding to a radius of $R = 17.5$ nm. For the results shown in the Fig. 4.18 the number of atoms per cluster is shown instead of their radii. For a better overview, not all cluster sizes were shown. The x–axis was divided into suitable intervals. Also, the intensity was normalized to $1/\omega^2$.

In sputtering experiments, where a high energetic particle is shot onto the target, a bimodal power–law for the size distribution $Y(N)$ is found [31, 137]. The ablation process is somewhat different, as the energy is deposited only by radiation. The complex character of the processes involved makes it difficult to establish a direct link between the existing theoretical models and the simulations done in this work. However, a power–law $Y(N) \propto N^{-\delta}$ for the yield distribution seems to be a fairly general phenomenon, as it is also observed in other ablation studies [75, 141]. There is no clear cut between the two ranges, thus the data was fitted for $N \lesssim 6$ and above. The observed range for the exponent is $\delta = 3.9$ to 5.1 and from 0.3 to 0.9 for the high–mass region. As it can be seen in Fig. 4.18, the values for δ are very sensitive to the used fitting interval, the exponents are therefore

only rough estimates. In experiments, the exponents are found not to be constant also. WUCHNER *et al.* gave $\delta = 7.7$ while in [31] a value of $\delta = 9.3$ is reported – both for the low–mass region $N \leq 10$. The experiments were ion sputtering on aluminum, so no fluence dependence could be reported, but the values from the simulations, e.g. $\delta = 5.1$, are quite comparable to the experiments. For the high–mass exponent a value between 1.21 and 1.31 was found in other simulations done by ZHIGILEI [141]. It also has to be taken into account, that the used potentials were not fitted to such applications, thus an intrinsic error by the used potential might occur.

4.4.3 Velocity and Angular Distribution

From the MD data the velocity and angular distribution functions of the plume can be calculated. The temperature of the plume is estimated by averaging the kinetic energy. Due to the directional expansion, the individual center of mass velocity of clusters with $N_{\text{atoms}} > 1$ has to be subtracted from its members. Fig. 4.19 shows the velocity distributions for five different laser pulses. It can be seen that the gas phase seems to have roughly the same temperature for all pulses. A fit to a MAXWELL–BOLTZMANN distribution shows, that all temperatures lie within an error of 200 K. For comparison a distribution for $T = 3107$ K is shown. The asymptotic standard error for the fitting procedure is less than 2 %. A slight deviation, especially in the region with small and large velocities to the ideal distribution can be seen. Usually a modified distribution function is used to describe the ablated particles [17]. The difference to the above method is, that an *off–set* or *steam velocity* is subtracted just in the direction of plume propagation instead of the center of mass velocity. The fastest particles found in the plume move with over 6 km/s. Velocities even higher (between 3 and 30 km/s) are reported in experiments, done with femtosecond pulses [99].

From the same data set angular distribution functions can be calculated. Several approaches for determining analytic expressions for them exist. KONOMI *et al.* compare two different functions to their experiments [68]. These were done by analyzing an aluminum foil, which was positioned above the experimental setup. The ablation was carried out in vacuum (4×10^{-4} Pa) with a GAUSSian–like intensity. Hence, the experiments should be comparable to the ideal GAUSSian intensity profile used here. Unfortunately aluminum was not among the studied metals. In addition

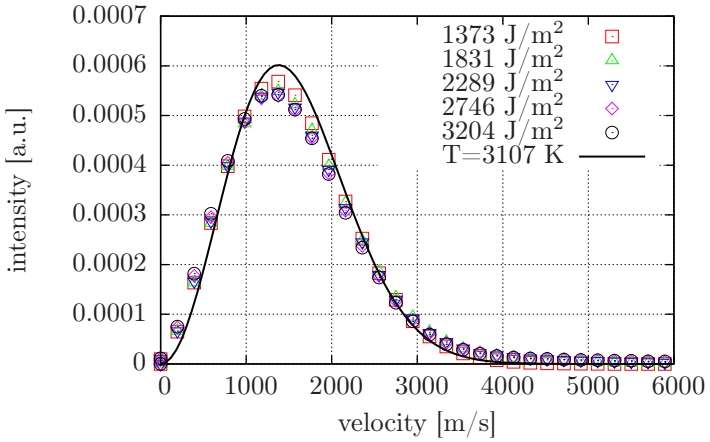

Figure 4.19: Velocity distribution calculated from MD simulations for the different fluences. For comparison a 3107 K Maxwell–Boltzmann velocity distribution is shown.

no fluence dependence of the plume, i.e. the distribution functions, was discussed. A more recent work by Donelly *et al.* compares different fluences – again not for aluminum but for nickel [36].

Other than for the velocity distribution, which was calculated over all the atoms inside the plume, the angular functions are calculated only for the clusters. This should better match the experimental conditions: Most of the material deposited — and countable — on the foil comes from larger chunks of matter, rather than from single atoms. Therefore, the calculated center of mass velocities were assigned to the according clusters. From the clustered data the distribution functions were calculated with respect to the center of mass velocity vectors.

All data points in Fig. 4.21 can be very well fitted to functions also used by Konomi *et al.* to interpret their experiments. The first function used contains the sum of two distributions, a broader (first term) and a narrower (second term) part:

$$f_1(\vartheta) = r[a\cos^m(\vartheta) + (1-a)\cos^n(\vartheta)],\ (m < n), \tag{4.10}$$

where r is the value at $\vartheta = 0$, a describes the ratio of the $\cos^m(\vartheta)$ compo-

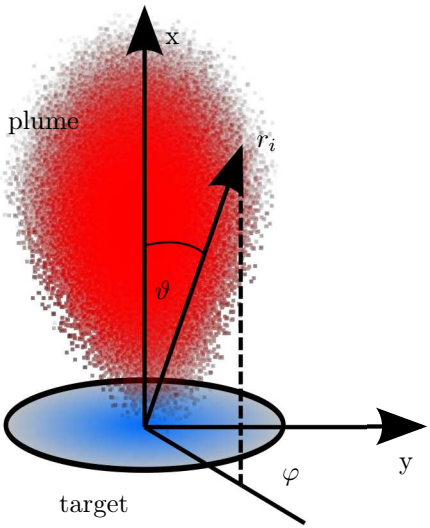

Figure 4.20: Angles ϑ and φ used for the angular–distribution functions.

nent to the whole distribution and ϑ is the angle with respect to the laser incident, see Fig. 4.20. In general, the curve describes the simulated data very well over the whole range. It can be seen (Tab. 4.2), that the ratio a of the broader distribution scales down roughly linear with increasing energy. This indicates a more directed ablation process with increasing fluence. Konomi reports values between $m = 1.0$ (Cu) up to $m = 4.0$ (Zr) and from $n = 3.0$ (In) to $n = 24$ (Ta) [68]. Tab. 4.2 summarizes the values from the simulations. For m, they lie in reasonable agreement with the experiments, while the n values came out slightly too small.

A second equation used to interpret experimental data can be derived

F [J/m^2]	r	a	m	n	k
1373	3.36	0.37	0.65	7.84	1.67
1831	7.29	0.33	2.35	20.9	2.47
2289	11.46	0.32	4.39	35.43	2.88
2746	16.49	0.27	6.10	48.45	3.06
3204	19.45	0.24	6.9	53.8	3.26

Table 4.2: Fit parameters for the angular distribution functions $f_1(\vartheta)$ and $f_2(\vartheta)$.

from a model based on gas dynamics by Anisimov [5, 8, 124]:

$$f_2(\vartheta) = r\frac{(1+\tan^2(\vartheta))^{3/2}}{(1+k^2\tan^2(\vartheta))^{3/2}}. \tag{4.11}$$

The fitting parameter k denotes the ratio of the cloud front along the surface normal direction and the front in direction of the surface, $k = X_{\text{inf}}/Y_{\text{inf}}$, respectively. While for small angles both functions fit the data set reasonable, for angles larger than 1 rad Eq. (4.11) leads to a smaller error in general, see Fig. 4.21. For different metals values for k between 1.1 (Cu) and 3.2 (Ta) are reported [68]. As mentioned above, all experiments were done with constant fluence, so it is impossible to compare the energy dependence of k. But from the simulations the dependence on the applied fluence can be very well fitted to $k(F) = \chi\sqrt{F - F_0} + k_0$ with $\chi = (38 \pm 2) \cdot 10^{-3}$ m$/\sqrt{\text{J}}$, $k_0 = 1.68 \pm 0.05$ and $F_0 = (1373 \pm 96)$ J/m^2. A larger value of k corresponds to a more forwarded ablation plume, which has been reported at least for the ions in [36]. For the un–charged particles, the exact opposite is reported: The angular distribution gets broader with higher fluences. One distribution of the azimuthal angle $\hat{f}(\varphi)$ is shown in Fig. 4.21. Since the problem has axial symmetry with respect to the laser incident — as expected — a constant particle flux to all directions is observed.

Summary

Simulations of inhomogeneous laser pulses were done and evaluated. It was shown that all accessible quantities compare well to experiments. The ablation threshold agrees with measurements, even if it is different from the

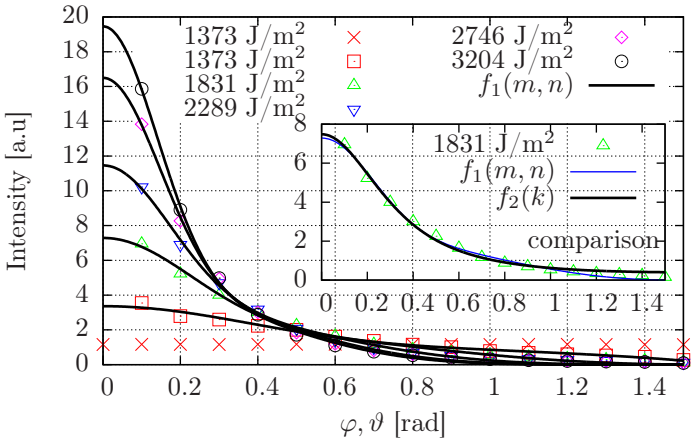

Figure 4.21: Angular distributions for different fluences between 1373 J/m^2 and 3204 J/m^2. The line shows the fit to Eq. (4.10). The inlay shows a direct comparison of the two analytic functions f_1 and f_2. In general Eq. (4.11) describes the data better than Eq. (4.10). The red crosses exemplarily show one azimuthal distribution $\hat{f}(\varphi)$ for the lowest fluence.

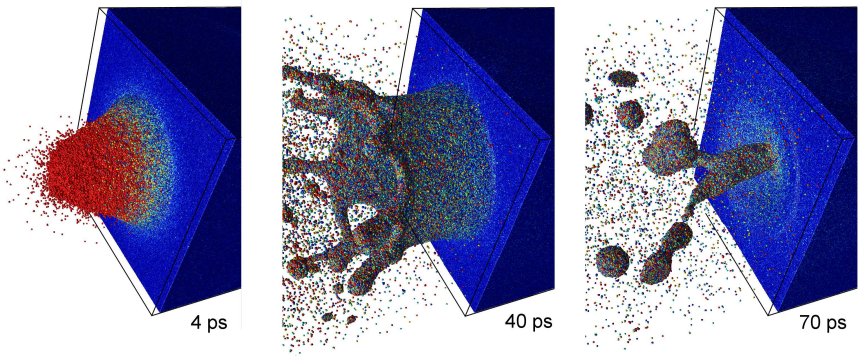

Figure 4.22: Snapshots of a 60 million atoms simulation 4, 40 and 70 ps after a 100 fs laser pulse hits the surface. The colors map the kinetic energy of the atoms. For visualization `MegaMol` [50] was used.

threshold value obtained by the Two–Temperature Model. Cluster statistics and velocity distributions were calculated from the MD data. Where available, experiments were compared to the simulations. Although the ablation simulation is one order of magnitude smaller in lateral direction than the smallest experiments, the detected angular distributions fit very well to the experiments. This indicates a scaling invariance concerning the evolving plume. Still, it is debatable if this simple model is good enough to describe the complex processes happening in the expanding plume. In comparison to experiments, it seems that a closer look at the ions has to be taken into account, even though they only make up 10–20% of the whole plume [36]. Additionally, recent experiments indicate, that the beam intensity profile $I(y, z)$ indeed has an impact on the particle size distribution [85].

4.5 Laser Ablation in Anisotropic Materials: A Case Study

Quasicrystals (QC) form a subgroup of complex metallic alloys (CMAs), which are locally similar due to their cluster sub–structure. Most of the known quasicrystals are found in Al–rich binary or ternary alloys like Al–Ni–Co, Al–Cu–Co or Al–Pd–Mn. Basically there are two sorts of stable quasicrystals interesting for laser ablation: Icosahedral and decagonal ones. This chapter will focus on an approximant to the decagonal phase of Al–Ni–Co.

Decagonal quasicrystals (d–QC) can be understood as periodic stacking of quasiperiodic two–dimensional planes, combining properties of periodic and quasiperiodic crystals. Due to the inherent structural anisotropy, d–QCs show a large anisotropy in their thermal transport properties [35, 118], and similarly in other parameters like the electrical resistivity [82], thermoelectric power [117], Hall coefficient [34] or optical conductivity [13]. For the simulations of a material with anisotropic properties the aluminum–cobalt alloy $Al_{13}Co_4$ was chosen. The alloy shows large affinity to decagonal quasicrystals, as a consequence, slight anisotropic melting behavior is observed.

4.5.1 Parameters for $Al_{13}Co_4$

The introduced hybrid simulation scheme in Sec. 3.3 describes the heat diffusion in isotropic materials. In $Al_{13}Co_4$ this isotropy is missing. Related to the three principal crystal directions a, b, and c, the thermal conductivity has different values. In the heat conduction equation (2.46) different — but constant — values for K_e have to be used for each direction. The equation is re–written into a more general form:

$$C_e(T_e)\frac{\partial T_e}{\partial t} = \left(K_e^a \frac{\partial^2}{\partial x^2} + K_e^b \frac{\partial^2}{\partial y^2} + K_e^c \frac{\partial^2}{\partial z^2} \right) T_e - \kappa(T_e - T_l) + S(x,t). \tag{4.12}$$

The interactions for the MD part are described by potentials of the EAM type, developed by Brommer *et al.* [18]. These potentials were fitted to ab initio data and were initially designed for high temperature diffusion studies. They can reproduce the melting point but are also able to stabilize surfaces at temperatures around 300 K for the three crystal directions. This is important because for ablation simulations periodic boundary conditions can only be used in two directions.

The orthorhombic $Al_{13}Co_4$ can be found in the Al–rich part of the Al–Co phase diagram [47]. The alloy belongs to the $Al_{13}TM_4$ group of decagonal approximants like $Al_{13}Fe_4$. According to the model of Grin *et al.* the lattice parameters are $a = 8.158$ Å, $b = 12.342$ Å and $c = 14.452$ Å with 102 atoms in the unit cell (space group $Pmn2_1$ and Pearson symbol $oP102$) [48]. Fig. 4.23 shows several unit cells, combined to one of the stacked layers.

There are no high temperature measurements for K_e, hence K_e is treated as constant[3]. All values are based on work done by Dolinšek *et al.* [35]. The values are

$$K_e = \{K_e^a, K_e^b, K_e^c\} = \{10.2, 4.4, 4.1\} \quad \frac{\mathrm{J}}{\mathrm{mKs}}, \tag{4.13}$$

with respect to the a–, b– and c–direction. For the specific heat of the electrons, a linear temperature behavior $C_e = \gamma T_e$ is used. Because no measurements existed, γ was used from the similar $Al_{13}Fe_4$ alloy, where data is available, $\gamma = 170$ J/m^{3}K^2 [102]. α^{-1} was chosen to be 8 nm.

[3] For real QCs it is even more difficult to determine the relevant constants like heat conductivity or electron–phonon coupling.

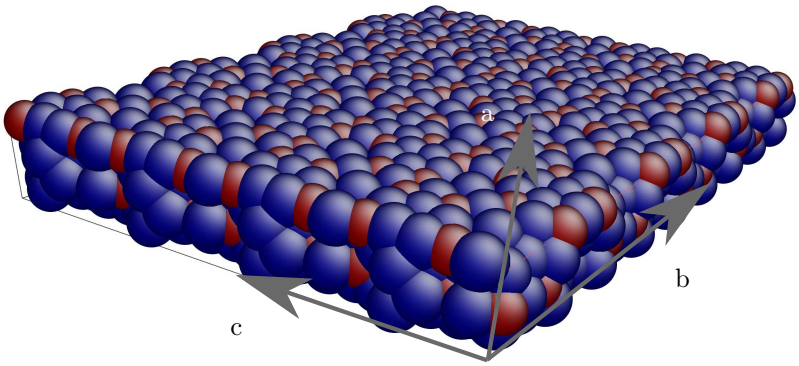

Figure 4.23: Several unit cells of the $Al_{13}Co_4$ alloy. The lattice parameters are $a = 8.158$ Å, $b = 12.342$ Å and $c = 14.452$ Å with 102 atoms in the unit cell. Blue are the aluminum atoms, in red cobalt is shown.

Different methods for the calculation of the electron–phonon coupling κ were given in Sec. 2.3. Following the equation of Wang *et al.* [133], κ is:

$$\kappa = \frac{\pi^4 (k_B v_s n_e)^2}{18 L \sigma_e(T_e) T_e} = 1.21 \cdot 10^{18} \frac{\mathrm{W}}{\mathrm{m^3 K}}. \tag{4.14}$$

The speed of sound v_s is independent of the crystal direction in d-QCs [25], n_e can be estimated from measurements of the Hall–coefficient [35]

$$R_H = -\frac{1}{n_e e}. \tag{4.15}$$

The Wiedemann–Franz law $K_e(T_e) = L\sigma_e(T_e)T_e$ is valid for quasicrystals over a wide temperature range, thus $K_e(T_e)$ and κ can be related [128, 35]. To avoid an anisotropy in κ, K_e and also n_e were averaged for the different crystal directions. The second equation derived by Allen [3] gives

$$\kappa = \frac{3\hbar\gamma\lambda\langle\omega^2\rangle}{\pi k_B} = 1.26 \cdot 10^{18} \frac{\mathrm{W}}{\mathrm{m^3 K}}. \tag{4.16}$$

For $\langle\omega^2\rangle$ the value 1050 meV^2 is taken [88], a value higher than for most pure metals. It can be explained by the strong Al–transition metal interactions

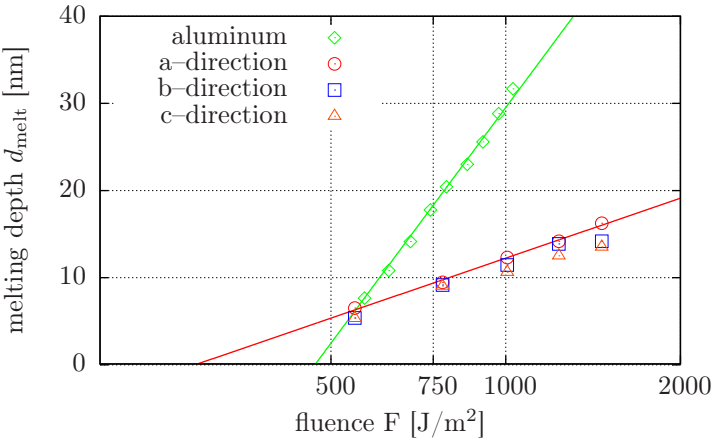

Figure 4.24: Melting depth for different laser fluences ($\sigma_t = 100$ fs). For comparison the values gained for pure aluminum by the TTM (see Sec. 4.2) are shown. Only a small effect of anisotropy can be seen.

dominating the dynamics of the system. λ is related to the SEEBECK coefficient of thermal power, Eq. (2.50), and was measured by DOLINŠEK *et al.* for $Al_{13}Co_4$ [35]. The values from Eq. (4.14) and (4.16) are quite similar, giving confidence to use the mean value, $\bar{\kappa} = 1.24 \cdot 10^{18} \frac{\mathrm{W}}{\mathrm{m^3 K}}$, for future simulations.

4.5.2 Laser Induced Surface Melting

The sample volume was $79 \times 18.3 \times 21.5$ nm^3, containing 2,295,000 atoms. For each of the crystal directions, a series of varying laser fluences between 91 and 1463 J/m^2 was performed. The pulse duration was set to $\sigma_t = 100$ fs. The results of the simulations is summarized in Fig. 4.24, where the melting depth d_{melt} is shown. For better comparison, d_{melt} for aluminum is also given[4]. A difference can be seen in the slope of $d_{\mathrm{melt}}(F)$, resulting in different melting thresholds. For the same fluence, the melted

[4]The points correspond to a cut through the surface in Fig. 4.12 on page 76 along $\sigma_t = 100$ fs.

layer in the alloy is less pronounced. Due to the comparatively small heat conduction (20 times smaller than in aluminum) the heat affected zone is smaller, thus the melting depth is decreased. The onset of melting for aluminum is determined to be $F_{\mathrm{melt}} = (469 \pm 6)$ J/m^2, which is comparable to the damage threshold of 340 J/m^2 given by Guo *et al.* [52]. In $Al_{13}Co_4$ melting thresholds are found at $F^a_{\mathrm{melt}} = (291 \pm 9)$ J/m^2, $F^b_{\mathrm{melt}} = (299 \pm 9)$ J/m^2 and $F^c_{\mathrm{melt}} = (277 \pm 8)$ J/m^2 for the *a*–, *b*– and *c*–direction. Beyond that, the deepest melting is found in the *a*–direction[5]. Up to now, no experiments on this alloy — or on comparable quasicrystals — were done. This makes conclusions on the validity of the results based on the simulations difficult.

However, a closer look reveals that the effect of anisotropic melting is very small. The difference in melting between the *a*– and the *b*–,*c*–directions is less than 5 nm, whereas the heat conduction is 2.5 times larger in the periodic direction. An explanation can be given by the small electron cooling time ($\tau_{\mathrm{el}} = C_{\mathrm{e}}/\kappa$) due to the comparatively high electron–phonon coupling constant. κ is more than twice as large compared to aluminum and more than 20 times bigger than in copper. The cooling time is 1 ps. In case of short relaxation times, the heat is confined to the atomic layers near the surface, leading to a weak direction dependent melting depth. It is also debatable if this simple approach of modeling the properties of the alloy is realistic enough. Therefore, future investigations should introduce more general material properties. κ also has a direction dependence. Additionally a temperature dependence in κ and K_{e} can be used.

Summary

The results for laser induced surface melting, calculated by the hybrid simulation scheme were shown. The model is able to describe laser absorption of the electrons and an anisotropic heat transfer to the lattice. The anisotropic heat conduction occurs due to the anisotropic structure of $Al_{13}Co_4$. The simulations showed that there is an effect of anisotropy but it is rather small. This leads to the conclusion, that before more complex structures like quasicrystals are investigated, the model has to be improved. However, the used TTM equations are designed mainly for metals. It is

[5] The direction with the highest value of heat conduction and the direction perpendicular to the semi–aperiodic plane.

debatable if a complex structure like an alloy or a quasicrystal is suitable for the Two–Temperature Model.

Chapter 5

Conclusion and Outlook

In this thesis, computer simulations of laser ablation in metals were studied. By the coupling of molecular dynamics (MD) to finite differences (FD) the advantages of both methods could be combined. Together, an approach for numerical experiments on the ablation process is given. With the FD equations, the model is able to describe the absorption of the laser energy by the electrons and the fast diffusive heat transport characteristic for metals. Parallel, a coupling to the phonons heats up the lattice atoms. The power of the MD method lies in the atomic resolution of all physical processes that occur. Melting, ablation, spallation, vaporization or cluster formation can all be seen from processed MD data. The results are delicate, because the majority of them is governed by the used potentials. Thus, choosing or creating potentials is an important task.

For aluminum an appropriate EAM potential was used. The potential is able to describe the solid–liquid and the liquid–gas phase transition very well. Different laser pulses (durations and intensity profiles) and also different models were studied. Where experiments were available, all predicted parameters match their experimental counterpart, see Tab. 5.1 for an overview. The important parameter of the ablation threshold from both methods, the more sophisticated TTM and the simpler rescale model (RES), compare very well to experiments. Ablation characteristics, i.e. cluster size and angular distributions or velocity of expansion, in the plume match qualitatively to experiments.

The model was additionally applied in ablation simulations of a more complex structure, $Al_{13}Co_4$. As an approximant to the decagonal phase of Al–Ni–Co, the alloy is built of periodically stacked semi–fivefold layers. Therefore, all transport properties show an anisotropy. Although all material parameters could be derived from theory or experiments, the expected anisotropy in the ablation behavior is missing. An explanation was given by the comparatively small electron–lattice relaxation time.

However, the model has room for improvement. It was shown that aluminum is an ideal material for the Two–Temperature Model (TTM) because of its short electron–thermalization time. Additional, the simple phase diagram makes the selection of a good potential a more straightforward task. For other system, like copper or gold, whose thermalization lasts ten times longer, the extended TTM given by HÜTTNER can be used as a starting point. For the electron heat conduction and the electron–phonon coupling constants were used. In reality, these quantities depend on the local lattice and electron temperature.

Outlook

Although the applied methods are very promising, it seems that they are too simple for more complex systems like metallic alloys. Also, it has to be noticed that only single pulse laser ablation into vacuum was studied. For typical applications like drilling, tens of thousands of pulses are needed. It was shown in experiments that the ambient gas or liquid has an impact on the ablation efficiency. Modeling an atmosphere or the evolving plasma cloud lies beyond the possibilities of standard molecular dynamics. Even for a second pulse problems arise. For a non–planar surface, interference between incoming and reflecting waves occur, thus solutions for the MAXWELL equations are needed.

For technological applications covalent systems are of special interest. For simulations of laser ablation in semiconductors, a computational approach that includes a description of the relaxation of a dense gas of hot electrons and holes generated by the laser pulse into classical MD is being developed by LORAZO *et al.* [80].

The system size also is an issue. In the simulations done, the beam diameter for inhomogeneous fluences was 30 nm. With todays technologies it is already possible to achieve beam diameters of 100 nm with so–called $\lambda/4$–pulses [111]. Still, a factor of three to five means a factor between 10 and 25[1] when it comes to simulation time.

The actual laser light was only modeled via its intensity on the surface. Experiments show, that also the polarization of the light has an influence on the physics. *Ripples*, whose orientation depends on the polarization formate on the irradiated surface.

[1] This assumes that only the lateral dimension matters. In direction parallel to the laser, typical penetration depths of 5–20 nm are already covered by todays simulations.

Summarizing, it could be shown, that for suitable systems the combination of the Two–Temperature Model to molecular dynamics is a powerful tool to predict and describe what is happening in laser heated metals by ultra short pulses.

Metal	-	Quantity	Theory	Experiments	Page
aluminum	Phase Diagram	T_{melt}	(1280 ± 50) K	934 K	63
		ϱ_{c}	$0.28 - 0.79$ g/cm^3	$0.7 - 0.9$ g/cm^3	66
		P_{c}	$0.19 - 0.55$ GPa	0.45 GPa	
		v_{s}	6522 m/s	6420 m/s	79
	Melting	τ_{el}	$1.58 - 2.53$ ps	4.27 ps	73
		t_{melt}	19 ps for 27 nm	20 ps for 25 nm	75
		F_{melt}	(469 ± 6) J/m^2	340 J/m^2	96
	Ablation	F_{th} (1)	(858 ± 170) J/m^2	$580 - 1200$ J/m^2	78
		F_{th} (2)	(1137 ± 166) J/m^2		84
		α^{-1} (1)	(27 ± 6) nm	39 nm	78
		α^{-1} (2)	(8.6 ± 1.7) nm		84
	Plume	v_{plume}	≈ 6 km/s	3–30 km/s	87
		k	$1.67 - 3.26$	$1.1 - 3.2$	
		m	$0.65 - 6.9$	$1 - 4$	90
		n	$7.84 - 53.8$	$3 - 24$	
		$-\delta$	$3.9 - 5.1$	$7.7 - 9.3$	86
$Al_{13}Co_4$	Melting	τ_{el}	≈ 1 ps	n.a.	96
		F^a_{melt}	(291 ± 9) J/m^2		
		F^b_{melt}	(299 ± 9) J/m^2		
		F^c_{melt}	(277 ± 8) J/m^2		

Table 5.1: Overview of all determined parameters and comparison to experiments where available. Additional for reference, the pages where the calculations were done are given. The numbers (1) and (2) for the ablation thresholds denote the different models, (1) for the TTM and (2) for the rescale method.

Appendix A

Used Software

A.1 IMD

IMD is a software package for classical molecular dynamics simulations. It is the abbreviation for ITAP Molecular Dynamics, where it is further developed [121]. Several types of interactions are already supported, such as simple pair potentials, EAM potentials for metals, STILLINGER–WEBER or TERSOFF potentials for covalent system. At this time, methods to deal with polarizable atoms are being implemented. Different integrators for the simulation of various thermodynamic ensembles, options that allow to shear or deform the sample during the simulation and many more are available. It is designed to run on massive parallel architectures, parallelized using the *Message Passing Interface* (MPI). Thus no restriction to the number of particles is given. Truly a great advantage of IMD is its compatibility to a wide range of systems from desktop PCs over large clusters up to supercomputers. Thereby IMD has an excellent scaling behavior with the number of processors. Typical execution times are in the order of 10^{-5} s per atom and time step. For a typical laser ablation simulation with 60,000,000 atoms and 50,000 time steps this results in $15 \cdot 10^6$ s computation time on a single CPU. On 512 CPUs it only takes eight hours.

During the last years IMD was extended with several features regarding laser ablation simulations in metals. Besides a simple rescaling model, where the kinetic energy of each atom is rescaled according to the outer laser field, a more complex hybrid model was implemented. In the so–called Two–Temperature Model an additional equation is solved in parallel to the standard molecular dynamics. This equation — a generalized heat conduction equation — describes the time evolution of the electronic temperature. Fast heat conduction in metals throughout the electronic system can be simulated. Current IMD versions are not only expanded by new

Quantity	Unit	SI value
length x	Å	10^{-10} m
time t	$\text{Å}\sqrt{\text{u/eV}}$	$10.18 \cdot 10^{-15}$ s
force f	eV/Å	$1.602 \cdot 10^{-09}$ N
stress σ	eV/Å^3	$1.602 \cdot 10^{-11}$ Pa
mass m	u	$1.661 \cdot 10^{-27}$ kg
fluence F	eV/Å^2	16.02 J/m^2
temperature T	eV	11605 K
heat capacity C	$\text{eV}/(\text{Å}^3\text{K})$	$1.381 \cdot 10^7$ J/(m^{3}K)
specific heat coefficient γ	$\text{eV}/(\text{Å}^3\text{K}^2)$	1189.7 J/(m^{3}K^2)
heat conductivity K	$\sqrt{\text{eV}^3}/(\sqrt{\text{u}}\text{KÅ})$	13.561 J/(sKm)
electron–phonon coupling κ	$\sqrt{\text{eV}^3}/(\sqrt{\text{u}}\text{Å}^4\text{K})$	$1.356 \cdot 10^{21}$ J/(m^{3}Ks)

Table A.1: Table of `IMD` units.

physical methods, there are ongoing projects were the code is ported to most current architectures like the Cell processor or the Blue Gene supercomputer.

Units

Although the used units in `IMD` can be chosen by the user, certain values have been established during the years. `IMD` determines the unit length after reading a configuration file, thus the user can give his own units to the program. The time step also is given by the user via a parameter file in multiples of 10.18 fs, see Tab. A.1

A.2 Rapidminer

`Rapidminer` is a tool for *data mining*, a process which can be generally defined as the extraction of patterns from data. It is currently used in wide ranges of research such as marketing, fraud detection or scientific discoveries. The manual extraction of patterns from given data sets has been done for many years. With growing data sets — both in size and complexity — direct hands–on analysis has become more and more tedious. The computer aided processing like neuronal networks, clustering, decision

trees or genetic algorithms have come to the fore. Rapidminer combines many modern tools for data mining in one framework. It has a powerful but intuitive graphical user interface and an on–the–fly error recognition system. It can handle all kinds of input format, especially data from IMD can be used without major pre–processing. Most comprehensive solutions like data integration, transformation, data modeling, evaluation and visualization are already included. Besides all these features, Rapidminer is availably freely as an open source project[1] [87].

Usually the process of data mining can be reduced into four classes of tasks:

1. *Clustering*, where the task is the discovery of groups and structures in the data without using known structures in the data.

2. *Classification*, where a known structure is applied to new data like in neuronal nets (the net is trained on a known data set and applied to new data to predict certain attributes like stock prices).

3. *Regression*, where the attempt is to find a function which models a given data with the least error.

4. *Association rule learning*, is the search for a relationship between variables.

Data mining was used in a variety of research fields. It was used for pattern recognition in chess games and also in economics, e.g. the market basket analysis, which tells retailers which goods customers like to purchase together. Data mining also is used in science and engineering like bio–informatics, genetics or medicine. However, from all great features available, only the clustering algorithms were used.

Fig. A.1 shows a screenshot of the actual worksheet that was used for the detection of the clusters in Sec. 4.4.2. The main window can be grouped into three parts. On the left a collection of tools can be seen. On the right side, parameters for the used algorithms can be changed. In the main window, all functions (which are called operators) can be used in a drag–and–drop fashion. For the clustering of atomic data a few operators (order from left to right) are necessary.

1. The data is read with a cvs reader.

[1] http://rapid-i.com/

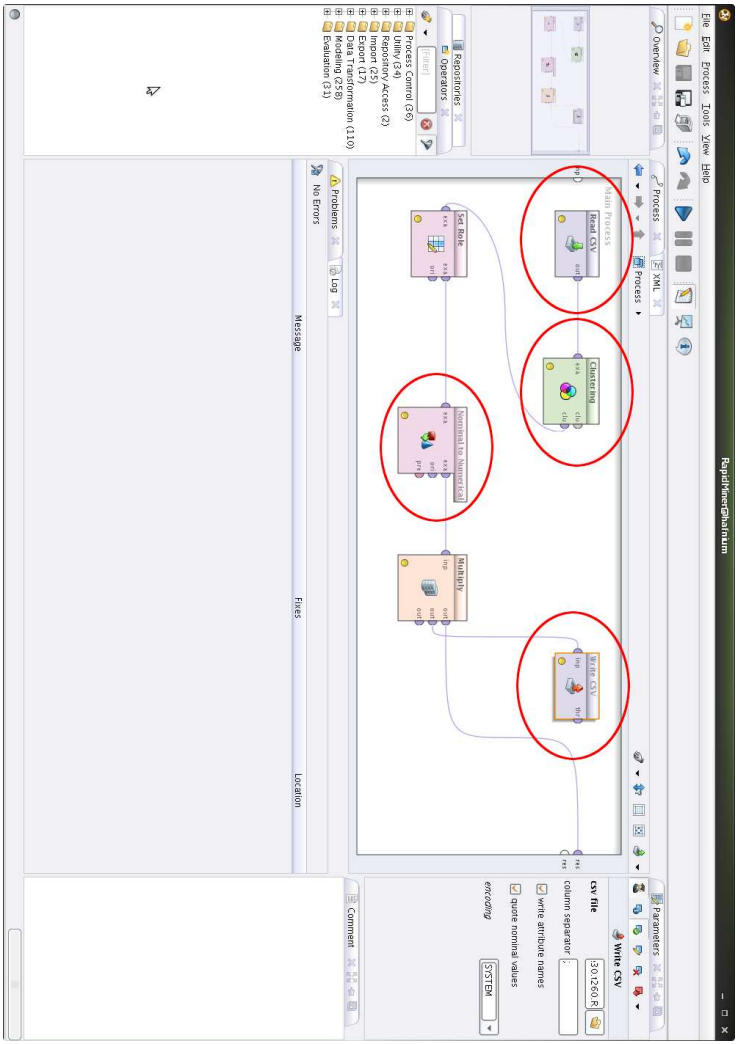

Figure A.1: Screenshot of the used tool `Rapidminer` for the cluster analysis. The circles show the four main modules used for the clustering of the atomic data.

2. The data set (in `x y z` format) is scanned for clusters using the `DBSCAN` algorithm.

3. The found attributes are converted from a string to a number. This makes post–processing with script languages like `awk` much easier.

4. The data set is written in the format `x y z id`.

`Rapidminer` lacks when it comes to efficiency. It is programmed in `Java` and runs on a single CPU only. Thus, clustering data in the order of 10^6 atoms takes up to 7 days. The same applies to its visualization capabilities. For large data sets ($> 10^5$ atoms) `Rapidminer` cannot be used in a user friendly way.

Bibliography

[1] Agranat, M., Anisimov, S., Ashitkov, S., Zhakhovskii, V., Inogamov, N., Nishihara, K., Petrov, Y., Fortov, V., and Khokhlov, V.: Dynamics of plume and crater formation after action of femtosecond laser pulse. *Applied Surface Science*, **253** (15), 6276–6282, 2007.

[2] Allen, M. and Tildesley, D.: *Computer Simulation of Liquids* (Oxford Science Publications, 1987).

[3] Allen, P. B.: Theory of thermal relaxation of electrons in metals. *Physical Review Letters*, **59** (13), 1460–1463, 1987.

[4] Amans, D., Chenus, A.-C., Ledoux, G., Dujardin, C., Reynaud, C., Sublemontier, O., Masenelli-Varlot, K., and Guillois, O.: Nanodiamond synthesis by pulsed laser ablation in liquids. *Diamond and Related Materials*, **18** (2-3), 177–180, 2009.

[5] Amoruso, S., Toftmann, B., and Schou, J.: Thermalization of a UV laser ablation plume in a background gas: From a directed to a diffusionlike flow. *Physical Review E*, **69** (5), 1–6, 2004.

[6] Anisimov, S. I., Inogamov, N. A., Petrov, Y. V., Khokhlov, V. A., Zhakhovskii, V. V., Nishihara, K., Agranat, M. B., Ashitkov, S. I., and Komarov, P. S.: Thresholds for front-side ablation and rear-side spallation of metal foil irradiated by femtosecond laser pulse. *Applied Physics A*, **92** (4), 797–801, 2008.

[7] Anisimov, S. I., Kapeliovich, B. L., and Perel'man, T. L.: Electron emission from metal surfaces exposed to ultra short laser pulses. *JETP Lett.*, **39** (2), 1974.

[8] Anisimov, S. I., Luk'yanchuk, B. S., and Luches, A.: An analytical model for three-dimensional laser plume expansion into vacuum in hydrodynamic regime. *Applied Surface Science*, **96-98**, 24–32, 1996.

[9] Anisimov, S. I. and Rethfeld, B.: On the theory of ultrashort laser pulse interaction with a metal. *Izvestia Akademii Nauk (Fiz.)*, **3093**, 192–203, 1997.

[10] Anisimov, S. I., Zhakhovskii, V. V., Inogamov, N. A., Nishihara, K., Petrov, Y. V., and Khokhlov, V. A.: Ablated matter expansion and crater formation under the action of ultrashort laser pulse. *Journal of Experimental and Theoretical Physics*, **103** (2), 183–197, 2006.

[11] Ashcroft, N. W. and Mermin, N. D.: *Solid State Physics* (Brooks/Cole, 1976).

[12] Baskes, M. I., Nelson, J. S., and Wright, A. F.: Semiempirical modified embedded-atom potentials for silicon and germanium. *Physical Review B*, **40** (9), 6085–6100, 1989.

[13] Basov, D. N., Timusk, T., Barakat, F., Greedan, J., and Grushko, B.: Anisotropic optical conductivity of decagonal quasicrystals. *Physical Review Letters*, **72** (12), 1937–1940, 1994.

[14] Bäuerle, D.: *Laser Processing and Chemistry* (Springer-Verlag Berlin Heidelberg New York, 2000).

[15] Bonn, M., Denzler, D. N., Funk, S., Wolf, M., Wellershoff, S.-S., and Hohlfeld, J.: Ultrafast electron dynamics at metal surfaces: Competition between electron-phonon coupling and hot-electron transport. *Physical Review B*, **61** (2), 1101–1105, 2000.

[16] Bouilly, D., Perez, D., and Lewis, L.: Damage in materials following ablation by ultrashort laser pulses: A molecular-dynamics study. *Physical Review B*, **76** (18), 1–9, 2007.

[17] Braun, R. and Hess, P.: Time-of-flight investigation of infrared laser-induced multilayer desorption of benzene. *The Journal of Chemical Physics*, **99** (10), 8330, 1993.

[18] Brommer, P. and Gähler, F.: Effective potentials for quasicrystals from ab-initio data. *Phil. Mag.*, **86** (6), 753–758, 2006.

[19] Brommer, P. and Gähler, F.: Potfit: effective potentials from ab initio data. *Modelling and Simulation in Materials Science and Engineering*, **15** (3), 295–304, 2007.

[20] Brorson, S. D., Kazeroonian, A., Moodera, J. S., Face, D. W., Cheng, T. K., Ippen, E. P., Dresselhaus, M. S., and Dresselhaus, G.: Femtosecond room-temperature measurement of the electron-phonon coupling constant γ in metallic superconductors. *Physical Review Letters*, **64** (18), 2172–2175, 1990.

[21] Brysk, H., Campbell, P. M., and Hammerling, P.: Thermal conduction in laser fusion. *Plasma Physics*, **17** (6), 473–484, 1975.

[22] Bulgakov, A. V., Ozerov, I., and Marine, W.: Cluster emission under femtosecond laser ablation of silicon. *Thin Solid Films*, **453-454**, 557–561, 2004.

[23] Bulgakova, N. M., Burakov, I. M., Meshcheryakov, Y. P., Stoian, R., Rosenfeld, A., and Hertel, I. V.: Theoretical Models and Qualitative Interpretations of Fs Laser Material Processing. *Journal of Laser Micro/Nanoengineering*, **2** (1), 76–86, 2007.

[24] Carslaw, H. S. and Jaeger, J. C.: *Conduction of Heat in Solids* (Oxford University Press, 1959).

[25] Chernikov, M. A.: Elastic properties of icosahedral and decagonal quasicrystals. *Physics-Uspekhi*, **48** (4), 411–417, 2005.

[26] Chichkov, B. N., Momma, C., Nolte, S., Alvensleben, F., and Tünnermann, A.: Femtosecond, picosecond and nanosecond laser ablation of solids. *Applied Physics A Materials Science & Processing*, **63** (2), 109–115, 1996.

[27] Chrisey, D. B. and Hubler, G. K.: *Pulsed Laser Deposition of Thin Films* (Wiley-Interscience, 1994).

[28] Christensen, B. H., Vestentoft, K., and Balling, P.: Short-pulse ablation rates and the two-temperature model. *Applied Surface Science*, **253** (15), 6347–6352, 2007.

[29] Colombier, J., Combis, P., Bonneau, F., Le Harzic, R., and Audouard, E.: Hydrodynamic simulations of metal ablation by femtosecond laser irradiation. *Physical Review B*, **71** (16), 1–6, 2005.

[30] Colombier, J., Combis, P., Stoian, R., and Audouard, E.: High shock release in ultrafast laser irradiated metals: Scenario for material ejection. *Physical Review B*, **75** (10), 1–11, 2007.

[31] Coon, S., Calaway, W., Pellin, M., and White, J.: New findings on the sputtering of neutral metal clusters. *Surface Science*, **298** (1), 161–172, 1993.

[32] Daw, M. S. and Baskes, M. I.: Embedded-atom method: Derivation and application to impurities, surfaces, and other defects in metals. *Physical Review B*, **29** (12), 6443–6453, 1984.

[33] Daw, M. S., Foiles, S. M., and Baskes, M. I.: The embedded-atom method: a review of theory and applications. *Materials Science Reports*, **9** (7-8), 251 – 310, 1993.

[34] Dian-Lin, Z., Li, L., Xue-Mei, W., Shu-Yuan, L., He, L., and Kuo, K.: Hall effect in a single two-dimensional quasicrystal: Al62Si3Cu20Co15. *Physical Review B*, **41** (12), 8557–8559, 1990.

[35] Dolinšek, J., Komelj, M., Jeglič, P., Vrtnik, S., Stanić, D., Popčević, P., Ivkov, J., Smontara, A., Jagličić, Z., Gille, P., and Grin, Y.: Anisotropic magnetic and transport properties of orthorhombic $Al_{13}Co_4$. *Physical Review B*, **79** (18), 184201, 2009.

[36] Donnelly, T., Lunney, J., Amoruso, S., Bruzzese, R., Wang, X., and Ni, X.: Angular distributions of plume components in ultrafast laser ablation of metal targets. *Applied Physics A*, **100**, 569–574, 2010.

[37] Ercolessi, F., Parrinello, M., and Tosatti, E.: Simulation of gold in the glue model. *Philosophical Magazine A*, **58** (1), 213–226, 1988.

[38] Ercolssi, F. and Adams, J. B.: Interatomic Potentials from First-Principles Calculations: The Force-Matching Method. *Europhysics Letters (EPL)*, **26** (8), 583–588, 1994.

[39] Ester, M., Kriegel, H.-p., Sander, J., and Xu, X.: A Density-Based Algorithm for Discovering Clusters in Large Spatial Databases with Noise. In *Proceedings of the Second International Conference on Knowledge Discovery and Data Mining (KDD-96)*, (editor U. M. F. Evangelos Simoudis, Jiawei Han), pages 226–231 (AAAI Press., 1996).

[40] Evans, R., Badger, A., Falliès, F., Mahdieh, M., Hall, T., Audebert, P., Geindre, J., Gauthier, J., Mysyrowicz, A., Grillon, G., and Antonetti, A.: Time- and Space-Resolved Optical Probing of Femtosecond-Laser-Driven Shock Waves in Aluminum. *Physical Review Letters*, **77** (16), 3359–3362, 1996.

[41] Faussurier, G., Blancard, C., and Silvestrelli, P.: Evaluation of aluminum critical point using an ab initio variational approach. *Physical Review B*, **79** (13), 1–7, 2009.

[42] Finnis, M., Agnew, P., and Foreman, A.: Thermal excitation of electrons in energetic displacement cascades. *Physical Review B*, **44** (2), 567–574, 1991.

[43] Fisher, D., Fraenkel, M., Henis, Z., Moshe, E., and Eliezer, S.: Interband and intraband (Drude) contributions to femtosecond laser absorption in aluminum. *Physical Review E*, **65** (1), 1–8, 2001.

[44] Forsblom, M. and Grimvall, G.: How superheated crystals melt. *Nature Materials*, **4** (5), 388–90, 2005.

[45] Gagliano, F. P. and Paek, U.: Thermal analysis of laser drilling processes. *IEEE Journal of Quantum Electronics*, **8** (2), 112–119, 1972.

[46] Garrelie, F., Aubreton, J., and Catherinot, A.: Monte Carlo simulation of the laser-induced plasma plume expansion under vacuum: Comparison with experiments. *Journal of Applied Physics*, **83** (10), 5075, 1998.

[47] Gille, P. and Bauer, B.: Single crystal growth of $Al_{13}Co_4$ and $Al_{13}Fe_4$ from Al-rich solutions by the czochralski method. *Cryst. Res. Technol.*, **43** (1), 1161–1167, 2008.

[48] Grin, J., Burkhardt, U., Ellner, M., and Peters, K.: Crystal structure of orthorhombic $Al_{13}Co_4$. *Journal of Alloys and Compounds*, **206** (2), 243 – 247, 1994.

[49] Groeneveld, R. H. M. and Sprik, R.: Femtosecond spectroscopy of electron–electron and electron–phonon energy relaxation in Ag and Au. *Physical Review B*, **51** (17), 11433–11445, 1995.

[50] Grottel, S., Reina, G., Dachsbacher, C., and Ertl, T.: Coherent Culling and Shading for Large Molecular Dynamics Visualization. *Computer Graphics Forum*, **29** (3), 953–962, 2010.

[51] Gumbsch, P., Zhou, S. J., and Holian, B. L.: Molecular dynamics investigation of dynamic crack stability. *Physical Review B*, **55** (6), 3445–3455, 1997.

[52] Guo, C., Rodriguez, G., Lobad, A., and Taylor, A. J.: Structural phase transition of aluminum induced by electronic excitation. *Physical Review Letters*, **84** (19), 4493–6, 2000.

[53] Häkkinen, H. and Landman, U.: Superheating, melting, and annealing of copper surfaces. *Physical Review Letters*, **71** (7), 1023–1026, 1993.

[54] Herziger, G. and Kreutz, E. W.: Fundamentals of laser microprocessing of metals. *Physica Scripta*, **T13**, 139–146, 1986.

[55] Hillenkamp, F. and Karas, M.: Matrix-assisted laser desorption/ionisation, an experience. *International Journal of Mass Spectrometry*, **200**, 71–77, 2000.

[56] Hohlfeld, J., Wellershoff, S.-S., Güdde, J., Conrad, U., Jähnke, V., and E., M.: Electron and lattice dynamics following optical excitation of metals. *Chemical Physics*, **251** (1-3), 237–258, 2000.

[57] Hüttner, B.: Femtosecond laser pulse interactions with metals. In *The Theory of Laser Materials Processing*, (editors R. Hull, R. M. Osgood, J. Parisi, H. Warlimont, and J. Dowden), volume 119 of *Springer Series in Materials Science*, pages 315–337 (Springer Netherlands, 2009). 978-1-4020-9340-1.

[58] Hüttner, B. and Gernot, R.: On the theory of ps and sub-ps laser pulse interaction with metals I. Surface temperature. *Applied Surface Science*, **103** (3), 269–274, 1996.

[59] Inogamov, N., Petrov, Y., Anisimov, S. I., Oparin, A., Shaposhnikov, N., von der Linde, D., and Meyer-ter Vehn, J.: Expansion of matter heated by an ultrashort laser pulse. *JETP Letters*, **69**, 310–316, 1999. 10.1134/1.568029.

[60] Ivanov, D. S., Rethfeld, B., O'Connor, G. M., Glynn, T. J., Volkov, A. N., and Zhigilei, L. V.: The mechanism of nanobump formation in femtosecond pulse laser nanostructuring of thin metal films. *Applied Physics A*, **92** (4), 791–796, 2008.

[61] Ivanov, D. S. and Zhigilei, L. V.: Combined atomistic-continuum modeling of short-pulse laser melting and disintegration of metal films. *Physical Review B*, **68** (6), 1–22, 2003.

[62] Jackson, J.: *Classical Electrodynamics* (New York: Wiley, 1975).

[63] Jin, Z., Gumbsch, P., Lu, K., and Ma, E.: Melting Mechanisms at the Limit of Superheating. *Physical Review Letters*, **87** (5), 12–15, 2001.

[64] Jou, D., Casas-Vázquez, J., and Lebon, G.: Extended irreversible thermodynamics revisited (1988-98). *Reports on Progress in Physics*, **62** (7), 1999.

[65] Kaiser, A. B.: Electron-phonon enhancement of thermopower: Application to metallic glasses. *Physical Review B*, **29** (12), 7088–7091, 1984.

[66] Kandyla, M., Shih, T., and Mazur, E.: Femtosecond dynamics of the laser-induced solid-to-liquid phase transition in aluminum. *Physical Review B*, **75** (21), 1–7, 2007.

[67] Kittel, C.: *Introduction to Solid State Physics* (John Wiley & Sons, 1976).

[68] Konomi, I., Motohiro, T., and Asaoka, T.: Angular distribution of atoms ejected by laser ablation of different metals. *Journal of Applied Physics*, **106** (1), 013107, 2009.

[69] Kresse, G. and Furthmüller, J.: Efficiency of ab-initio total energy calculations for metals and semiconductors using a plane-wave basis set. *Computational Materials Science*, **6** (1), 15 – 50, 1996.

[70] Kresse, G. and Furthmüller, J.: Efficient iterative schemes for ab initio total-energy calculations using a plane-wave basis set. *Physical Review B*, **54** (16), 11169–11186, 1996.

[71] Kresse, G. and Hafner, J.: Ab initio molecular dynamics for liquid metals. *Physical Review B*, **47** (1), 558–561, 1993.

[72] Kresse, G. and Hafner, J.: Ab initio molecular-dynamics simulation of the liquid-metal–amorphous-semiconductor transition in germanium. *Physical Review B*, **49** (20), 14251–14269, 1994.

[73] Le Harzic, R., Breitling, D., Weikert, M., Sommer, S., Föhl, C., Dausinger, F., Valette, S., Donnet, C., and Audouard, E.: Ablation comparison with low and high energy densities for Cu and Al with ultra-short laser pulses. *Applied Physics A*, **80** (7), 1589–1593, 2005.

[74] Lescoute, E., Hallo, L., Chimier, B., Hébert, D., Tikhonchuk, V. T., Stenz, C., Chevalier, J.-M., Rullier, J.-L., and Palmier, S.: Particles formation in an expanding plasma. *The European Physical Journal Special Topics*, **175** (1), 159–164, 2009.

[75] Leveugle, E. and Zhigilei, L. V.: Molecular dynamics simulation study of the ejection and transport of polymer molecules in matrix-assisted pulsed laser evaporation. *Journal of Applied Physics*, **102** (7), 074914, 2007.

[76] Li, J.: AtomEye: an efficient atomistic configuration viewer. *Modelling and Simulation in Materials Science and Engineering*, **11** (2), 173–177, 2003.

[77] Lide, D. R. (editor): *CRC Handbook of Chemistry and Physics* (CRC Press LLC, 1997).

[78] Lin, Z. and Zhigilei, L. V.: Temperature dependences of the electron–phonon coupling, electron heat capacity and thermal conductivity in Ni under femtosecond laser irradiation. *Applied Surface Science*, **253** (15), 6295–6300, 2007.

[79] Lin, Z., Zhigilei, L. V., and Celli, V.: Electron-phonon coupling and electron heat capacity of metals under conditions of strong electron-phonon nonequilibrium. *Physical Review B*, **77** (7), 1–17, 2008.

[80] Lorazo, P., Lewis, L. J., and Meunier, M.: Picosecond pulsed laser ablation of silicon: a molecular-dynamics study. *Applied Surface Science*, **168** (1-4), 276–279, 2000.

[81] Madsen, N. R., Gamaly, E. G., Rode, a. V., and Luther-Davies, B.: Cluster formation through the action of a single picosecond laser pulse. *Journal of Physics: Conference Series*, **59**, 762–768, 2007.

[82] Martin, S., Hebard, A. F., Kortan, A. R., and Thiel, F. A.: Transport properties of $Al_{65}Cu_{15}Co_{20}$ and $Al_{70}Ni_{15}Co_{15}$ decagonal quasicrystals. *Physical Review Letters*, **67** (6), 719–722, 1991.

[83] Maxwell, J. C.: On the Dynamical Theory of Gases. *Philosophical Transactions of the Royal Society of London*, **157**, 49–88, 1867.

[84] McMillan, W.: Transition Temperature of Strong-Coupled Superconductors. *Physical Review*, **167** (2), 331–344, 1968.

[85] Menéndez-Manjón, A., Barcikowski, S., Shafeev, G., Mazhukin, V., and Chichkov, B.: Influence of beam intensity profile on the aerodynamic particle size distributions generated by femtosecond laser ablation. *Laser and Particle Beams*, **28** (01), 45, 2010.

[86] Metzler, R. and Compte, A.: Stochastic foundation of normal and anomalous Cattaneo-type transport. *Physica A*, **268**, 454– 468, 1999.

[87] Mierswa, I., Wurst, M., Klinkenberg, R., Scholz, M., and Euler, T.: Yale: Rapid prototyping for complex data mining tasks. In *KDD '06: Proceedings of the 12th ACM SIGKDD international conference on Knowledge discovery and data mining*, (editors L. Ungar, M. Craven, D. Gunopulos, and T. Eliassi-Rad), pages 935–940 (ACM, New York, NY, USA, 2006). 1-59593-339-5.

[88] Mihalkovič, M. and Widom, M.: First-principles calculations of cohesive energies in the Al-Co binary alloy system. *Physical Review B*, **75** (1), 1–10, 2007.

[89] Mishin, Y.: Atomistic modeling of the γ and γ'–phases of the Ni–Al system. *Acta Materialia*, **52** (6), 1451–1467, 2004.

[90] Mishin, Y., Farkas, D., Mehl, M. J., and Papaconstantopoulos, D. A.: Interatomic potentials for monoatomic metals from experimental data and ab initio calculations. *Physical Review B*, **59** (5), 1999.

[91] Mishin, Y. and Lozovoi, a.: Angular-dependent interatomic potential for tantalum. *Acta Materialia*, **54** (19), 5013–5026, 2006.

[92] Mishin, Y., Mehl, M., and Papaconstantopoulos, D.: Phase stability in the Fe–Ni system: Investigation by first-principles calculations and atomistic simulations. *Acta Materialia*, **53** (15), 4029–4041, 2005.

[93] Mishin, Y., Mehl, M., Papaconstantopoulos, D., Voter, A., and Kress, J.: Structural stability and lattice defects in copper: Ab initio, tight-binding, and embedded-atom calculations. *Physical Review B*, **63** (22), 1–16, 2001.

[94] Momma, C., Nolte, S., Chichkov, B., Tunnermann, A., and von Alvensleben, F.: Precise Laser Ablation with Ultra-Short Pulses. *Proceedings of European Meeting on Lasers and Electro-Optics*, pages 318–318, 1997.

[95] Nosé, S.: A unified formulation of the constant temperature molecular dynamics methods. *J. Chem. Phys.*, **81** (November 1983), 511–519, 1984.

[96] Nosé, S.: A molecular dynamics method for simulations in the canonical ensemble. *Molecular Physics*, **100** (1), 191–198, 2002.

[97] Ohmura, E. and Fukumoto, I.: Molecular dynamics simulation on laser ablation of fcc metal. *Int. J. Japan Soc. Prec. Eng.*, **30**, 128–133, 1996.

[98] Ohmura, E. and Fukumoto, I.: Modified molecular dynamics simulation on laser ablation of metal. *Int. J. Japan Soc. Prec. Eng.*, **31**, 206–207, 1997.

[99] Okano, Y., Oguri, K., Nishikawa, T., and Nakano, H.: Observation of femtosecond-laser-induced ablation plumes of aluminum using space- and time-resolved soft x-ray absorption spectroscopy. *Applied Physics Letters*, **89** (22), 221502, 2006.

[100] Pasianot, R., Farkas, D., and Savino, E.: Empirical many-body interatomic potential for bcc transition metals. *Physical Review B*, **43** (9), 6952–6961, 1991.

[101] Penrose, R.: The rôle of aesthetics in pure and applied mathematical research. *Bull. Inst. Math. and its Appl.*, **10**, 226–271, 1974.

[102] Popčević, P., Smontara, a., Ivkov, J., Wencka, M., Komelj, M., Jeglič, P., Vrtnik, S., Bobnar, M., Jagličić, Z., Bauer, B., Gille, P., Borrmann, H., Burkhardt, U., Grin, Y., and Dolinšek, J.: Anisotropic physical properties of the $Al_{13}Fe_4$ complex intermetallic and its ternary derivative $Al_{13}(Fe,Ni)_4$. *Physical Review B*, **81** (18), 1–12, 2010.

[103] Press, W. H., Teukolsky, S. A., Vetterling, W. T., and Flannery, B. P.: *Numerical Recipes in C: The Art of Scientific Computing* (Academic Press, Cambridge, 2007), 3. edition.

[104] Preuss, S., Demchuk, A., and Stuke, M.: Sub-picosecond UV laser ablation of metals. *Applied Physics A*, **61** (1), 33–37, 1995.

[105] Puretzky, A. A., Geohegan, D. B., Fan, X., and Pennycook, S. J.: Dynamics of single-wall carbon nanotube synthesis by laser vaporization. *Applied Physics A*, **70** (2), 153–160, 2000.

[106] Rethfeld, B.: *Mikroskopische Prozesse bei der Wechselwirkung von Festkörpern mit Laserpulsen im Subpikosekundenbereich*. Ph.D. thesis, Technischen Universität Carolo-Wilhelmina zu Braunschweig, 1999.

[107] Rethfeld, B., Kaiser, A., Vicanek, M., and Simon, G.: Femtosecond laser-induced heating of electron gas in aluminium. *Applied Physics A*, **69** (7), S109–S112, 1999.

[108] Rethfeld, B., Kaiser, A., Vicanek, M., and Simon, G.: Ultrafast dynamics of nonequilibrium electrons in metals under femtosecond laser irradiation. *Physical Review B*, **65** (21), 1–11, 2002.

[109] Rindler, W.: *Relativity* (Oxford University Press, 2001).

[110] Rizvi, N. H.: Femtosecond laser micromachining: Current status and applications. *RIKEN Review*, **50** (50), 107–112, 2003.

[111] Ródenas, A., Lamela, J., Jaque, D., Lifante, G., Jaque, F., García-Martín, A., Zhou, G., and Gu, M.: Near-field imaging of femtosecond laser ablated sub-$\lambda/4$ holes in lithium niobate. *Applied Physics Letters*, **95** (18), 181103, 2009.

[112] Sakurai, J. J.: *Modern Quantum Mechanics* (Addison Wesley Longman, 1994).

[113] Sales, M., Merstallinger, A., Brunet, P., de Weerd, M. C., Khare, V., Traxler, G., and Dubois, J. M.: Cold welding and fretting tests on quasicrystals and related compounds. *Philosophical Magazine*, **86** (6-8), 965–970, 2006.

[114] Schäfer, C., Urbassek, H. M., and Zhigilei, L. V.: Metal ablation by picosecond laser pulses: A hybrid simulation. *Physical Review B*, **66** (11), 115404, 2002.

[115] Schmidt, V., Husinsky, W., and Betz, G.: Ultrashort laser ablation of metals: pump–probe experiments, the role of ballistic electrons and the two–temperature model. *Applied Surface Science*, **197-198**, 145–155, 2002.

[116] Shechtman, D., Blech, I., Gratias, D., and Cahn, J. W.: Metallic phase with long-range orientational order and no translational symmetry. *Physical Review Letters*, **53** (20), 1951–1953, 1984.

[117] Shu-yuan, L., Xue-mei, W., Li, L., Dian-lin, Z., He, L. X., and Kuo, K. X.: Anisotropic transport properties of a stable two-dimensional quasicrystal: $Al_{62}Si_3Cu_{20}Co_{15}$. *Physical Review B*, **41** (13), 9625–9627, 1990.

[118] Smontara, A., Smiljanić, I., Ivkov, J., Stanić, D., Barišić, O. S., Jagličić, Z., Gille, P., Komelj, M., Jeglič, P., Bobnar, M., and Dolinšek, J.: Anisotropic magnetic, electrical, and thermal transport properties of the Y-Al-Ni-Co decagonal approximant. *Physical Review B*, **78** (10), 104204, 2008.

[119] Sokolowski-Tinten, K., Bialkowski, J., Cavalleri, A., von der Linde, D., Oparin, A., Meyer-ter Vehn, J., and Anisimov, S. I.: Transient states of matter during short pulse laser ablation. *Physical Review Letters*, **81** (1), 224–227, 1998.

[120] Springel, V., White, S. D. M., Jenkins, A., Frenk, C. S., Yoshida, N., Gao, L., Navarro, J., Thacker, R., Croton, D., Helly, J., Peacock, J. a., Cole, S., Thomas, P., Couchman, H., Evrard, A., Colberg, J.,

and Pearce, F.: Simulations of the formation, evolution and clustering of galaxies and quasars. *Nature*, **435** (7042), 629–36, 2005.

[121] Stadler, J., Mikulla, R., and Trebin, H.-R.: IMD: a software package for molecular dynamics studies on parallel computers. *Int. J. Mod. Phys. C*, **8** (5), 1131–1140, 1997. `http://www.itap.physik.uni-stuttgart.de/~imd/`.

[122] Stillinger, F. H. and Weber, T. A.: Computer simulation of local order in condensed phases of silicon. *Physical Review B*, **31** (8), 5262–5271, 1985.

[123] Tersoff, J.: Modeling solid-state chemistry: Interatomic potentials for multicomponent systems. *Physical Review B*, **39** (8), 5566–5568, 1989.

[124] Toftmann, B., Schou, J., and Lunney, J.: Dynamics of the plume produced by nanosecond ultraviolet laser ablation of metals. *Physical Review B*, **67** (10), 1–5, 2003.

[125] Ulrich, C. M.: *Simulation der Laserablation an Metallen.* Master's thesis, Universität Stuttgart, 2007.

[126] Upadhyay, A. K., Inogamov, N. A., Rethfeld, B., and Urbassek, H. M.: Ablation by ultrashort laser pulses: Atomistic and thermodynamic analysis of the processes at the ablation threshold. *Physical Review B*, **78** (4), 1–10, 2008.

[127] Valette, S., Audouard, E., Le Harzic, R., Huot, N., Laporte, P., and Fortunier, R.: Heat affected zone in aluminum single crystals submitted to femtosecond laser irradiations. *Applied Surface Science*, **239** (3-4), 381–386, 2005.

[128] Vekilov, Y., Isaev, E., and Johansson, B.: Does the Wiedemann-Franz law work for quasicrystals? *Physics Letters A*, **352** (6), 524 – 525, 2006.

[129] Von der Linde, D., Sokolowski-Tinten, K., and Bialkowski, J.: Laser-solid interaction in the femtosecond time regime. *Applied Surface Science*, **109-110**, 1–10, 1997.

[130] Vorobyev, A., Kuzmichev, V., Kokody, N., Kohns, P., Dai, J., and Guo, C.: Residual thermal effects in Al following single ns- and fs-laser pulse ablation. *Applied Physics A*, **82** (2), 357–362, 2005.

[131] Wang, X. and Xu, X.: Thermoelastic wave induced by pulsed laser heating. *Applied Physics A*, **73** (1), 107–114, 2001.

[132] Wang, X. Y., Riffe, D. M., Lee, Y.-S., and Downer, M. C.: Time-resolved electron-temperature measurement in a highly excited gold target using femtosecond thermionic emission. *Physical Review B*, **50** (11), 8016–8019, 1994.

[133] Wang, Z. G., Dufour, C., Paumier, E., and Toulemonde, M.: The S_e sensitivity of metals under swift-heavy-ion irradiation: a transient thermal process. *Journal of Physics: Condensed Matter*, **6** (34), 6733–6750, 1994.

[134] Waynant, R. W.: *Lasers in Medicine* (CRC Press LLC, 2002).

[135] Wellershoff, S.-S., Hohlfeld, J., Güdde, J., and Matthias, E.: The role of electron-phonon coupling in femtosecond laser damage of metals. *Applied Physics A*, **69** (7), S99–S107, 1999.

[136] Williamson, S., Mourou, G., and Li, J. C. M.: Time-Resolved Laser-Induced Phase Transformation in Aluminum. *Physical Review Letters*, **52** (26), 2364–2367, 1984.

[137] Wuchner, A. and Wahl, M.: The formation of clusters during ion induced sputtering of metals. *Nuclear Instruments and Methods in Physics Research Section B: Beam Interactions with Materials and Atoms*, **115** (1-4), 581–589, 1996.

[138] Zhakhovskii, V. V., Inogamov, N. A., Petrov, Y. V., Ashitkov, S. I., and Nishihara, K.: Molecular dynamics simulation of femtosecond ablation and spallation with different interatomic potentials. *Applied Surface Science*, **255** (24), 9592–9596, 2009.

[139] Zhang, D. M., Li, L., Li, Z. H., Guan, L., Tan, X., and Liu, D.: Non-Fourier heat conduction studying on high-power short-pulse laser ablation considering heat source effect. *The European Physical Journal Applied Physics*, **33** (2), 91–96, 2006.

[140] Zhidkov, A., Zhigilei, L., Sasaki, A., and Tajima, T.: Short-laser-pulse-driven emission of energetic ions into a solid target from a surface layer spalled by a laser prepulse. *Applied Physics A*, **73** (6), 741–747, 2001.

[141] Zhigilei, L. V.: Dynamics of the plume formation and parameters of the ejected clusters in short-pulse laser ablation. *Applied Physics A*, **76** (3), 339–350, 2003.

[142] Zhigilei, L. V. and Dongare, A. M.: Multiscale Modeling of Laser Ablation: Applications to Nanotechnology. *Science*, **3** (5), 539–555, 2002.

[143] Zhigilei, L. V. and Garrison, B. J.: Velocity distributions of molecules ejected in laser ablation. *Applied Physics Letters*, **71** (4), 551, 1997.

List of Publications

[144] Sonntag, S., Trichet, C., Roth, J., and Trebin, H.-R.: Molecular Dynamics Simulations of Cluster Distribution from Femtosecond Laser Ablation in Aluminum. *submitted*, 2010.

[145] Sonntag, S., Roth, J., and Trebin, H.-R.: Molecular dynamics simulations of laser induced surface melting in orthorhombic Al13Co4. *Applied Physics A*, **101** (1), 77–80, 2010.

[146] Lipp, H., Engel, M., Sonntag, S., and Trebin, H.-R.: Phason dynamics in one-dimensional lattices. *Physical Review B*, **81** (6), 1–12, 2010.

[147] Roth, J., Trichet, C., Trebin, H.-R., and Sonntag, S.: *Laser Ablation of Metals in High Performance Computing in Science and Engineering 2010* (Springer Heidelberg, 2010).

[148] Sonntag, S., Roth, J., Gaehler, F., and Trebin, H.-R.: Femtosecond laser ablation of aluminium. *Applied Surface Science*, **255** (24), 9742 – 9744, 2009.

[149] Engel, M., Sonntag, S., Lipp, H., and Trebin, H.-R.: Structure factors of harmonic and anharmonic Fibonacci chains by molecular dynamics simulations. *Physical Review B*, **75** (14), 2007.

[150] Sonntag, S.: *Zum Strukturfaktor der dynamischen Fibonacci-Kette*. Master's thesis, Universität Stuttgart, 2006.

Danksagung

Ein ganz besonders herzliches Dankeschön gebührt Prof. Dr. Hans–Rainer Trebin, der mich an seinem Lehrstuhl aufgenommen und in die luxuriöse Lage gebracht hat, diese Doktorarbeit über eine SFB Stelle anfertigen zu können.

Prof. Dr. Christian Holm möchte ich dafür danken, dass er so kurzfristig den Mitbericht übernommen hat.

Prof. Dr. J. Wrachtrup danke ich für die Übernahme als Prüfunsvorsitzenden.

Bei PD Dr. Johannes Roth bedanke ich mich als erstklassigen Ansprechpartner für alle Physik- und Technikfragen, die sich während der Jahre ergeben haben.

Auch wenn Peter Brommer derzeit nicht am ITAP ist, war er zwei Jahre stets mein erster Ansprechparter für Probleme jeder Art. Seit eineinhalb Jahren hat Philipp Beck als mein Zimmerkollege diese Rolle übernommen.

Hansjörg Lipp gebührt ein Dank für die Hilfe mit den Skripten, die ich benötigt habe, um meine Daten auszuwerten. Er ist ganz sicher ein Meister im Umgang mit der Konsole.

Mit Valeriano Ferreras Paz und Jürgen Falb habe ich unzählige Mittagspausen – nicht nur in der Mensa – verbracht. Dank ihnen mag ich heute keine Subway Sandwiches mehr. Schade nur, dass *traderz* bis heute nicht zum gewünschten Erfolg geführt hat.

Felix Maye danke ich für die schönen Abende in der Reinsburgstraße, auf die ich mich auch noch heute ganz besonders freue.

Nach zehn Jahren gemeinsamen Studiums danke ich Moritz Vogel für seine Freundschaft, Bereitschaft zum Lernen, zum Sport machen oder einfach zum Ausgehen und Spaß haben.

Robert Hafenbrak möchte ich für die gemeinsamen Einkäufe, für das Scannen wichtiger Dokumente sowie dem Galgenhumor auf dem Gang danke sagen.

Von Marcus Witzany und Moritz Bommer habe ich 2006 Texas Hold Em gelernt das zeitweise zu meinem größten Hobby wurde. Viele lustige Abende am Olgaeck haben während der letzten sechs Jahre für genügend Abwechslung gesorgt. Scharfes Essen und Islay Malts gehören nun dank ihnen zu einem festen Bestandteil meines Lebens.

Den Doktoren Andrew Aird und Roman Bedau danke ich für das Korrekturlesen des Manuskripts sowie für die interessanten Perspektivengespräche.

Andreas Chatzopoulos war während meiner Promotion mein liebster Ansprechpartner für alle Fragen, Sorgen und Probleme, die weniger mit Physik zu tun hatten. Für die anstregenden Nachsitzungen in Zimmer 6.346 sowie der entstandenen Freundschaft auf Dienstreisen möchte ich mich ganz besonders bedanken.

Bei Carolina Trichet Paredes und Johannes Karlin möchte ich mich für ihre Mitarbeit in der *small laser group* bedanken. Ohne Johannes wären wir sicher nicht so überzeugt von unserem Code gewesen.

Matthias Scheidewig, Tobias Denner und Eberhard Renz gebührt ein ganz besonderes *muchas gracias* für die seit über zwei Jahren fest stehende Stammtischrunde im Irish Pub, bei der es nicht ein einziges Mal um Physik ging.

Dem liebsten Menschen auf der Erde danke ich dafür, dass sie immer für mich da ist: Daniela ♡.

Meinen Eltern möchte ich danke sagen für den Rückhalt, den ich immer bei all meinem Treiben bekommen habe. Ihnen ist diese Arbeit gewidmet.

Ehrenwörtliche Erklärung

Ich erkläre, dass ich diese Arbeit selbstständig verfasst und keine anderen als die angegebenen Quellen und Hilfsmittel benutzt habe.

Stuttgart, im Dezember 2010 Steffen Sonntag